

NORTHWESTERN UNIVERSITY

Engineering Plasmonic Lasing from Visible to Near-infrared Wavelength

A DISSERTATION

SUBMITTED TO THE GRADUATE SCHOOL  
IN PARTIAL FULFILLMENT OF THE REQUIREMENTS

For the degree of

DOCTOR OF PHILOSOPHY

Field of Materials Science and Engineering

by

Ran Li

EVANSTON, ILLINOIS

March 2020

© Copyright by Ran Li 2020

All Rights Reserved

## **ABSTRACT**

### **Engineering Plasmonic Lasing from Visible to Near-infrared Wavelength**

**Ran Li**

Light trapping with standing waves has been achieved using photonic bandgap crystals, metal-dielectric waveguides and periodic metal nanocavity arrays. Compared with photonic materials, plasmonic metal nanocavities can provide light confinement at the sub-wavelength scale with strong near-field electric enhancement. The localized surface plasmons of individual metal nanoparticles can collectively couple to the diffraction modes from the lattice geometry, giving rise to surface lattice resonances. Surface lattice resonances can serve as optical feedback for plasmonic nanolasing at room temperature. By engineering the unit cell or lattice geometry of a plasmonic nanoparticle array, we are able to manipulate the coupling mechanisms of the plasmonic nanoparticles, leading to the realization of a plasmonic nanolaser with distinct hotspot regions.

In Chapter 1, we discuss how the coupling between plasmonic nanocavities changes with lattice geometries. We fabricated plasmonic aluminum nanoparticles on Polydimethylsiloxane substrate and investigated the optical responses under different stretching conditions. Chapter 2 describes the linear and nonlinear properties of plasmonic nanoparticle arrays fabricated using different plasmonic materials. We achieved sharp surface lattice resonances with Au and Al nanoparticle arrays and integrated organic dye molecules to the arrays to compare the lasing emissions and ultrafast dynamic behaviors between different plasmonic materials. Chapter 3 shows the realization of multicolor lasers on a single device. By mixing two or three different dye solutions, we can broaden the photoluminescence of the dye gain medium to spectrally overlap with different surface lattice resonances simultaneously. By stacking two plasmonic nanoparticle

lattices with different periodicities and incorporating mixed dye solutions between the lattices, we obtained blue, green and red color lasing emissions at the same time, which can be potentially used to achieve a plasmonic white laser.

Chapters 4 and 5 discuss the coupling mechanism in hexagonal and honeycomb lattices at different high-symmetry points. Chapter 4 presents the distinct coupling in plasmonic honeycomb lattices caused by the non-Bravais nature of a honeycomb lattice. We discovered that the surface lattice resonance at the  $\Gamma$  point of a honeycomb lattice has in-plane dipole coupling hybridized with in-plane quadrupole coupling, while the surface lattice resonance at the  $\Gamma$  of hexagonal lattice only shows in-plane dipole coupling. Besides looking the surface lattice resonance at the  $\Gamma$  point, we also investigated the surface lattice resonance at the off-normal M point in Chapter 5. Out-of-plane dipole coupling was revealed in a hexagonal array and high order coupling leads to mode splitting at the M point of honeycomb lattice. These findings show the importance of the non-Bravais nature in a unit cell to the near-field coupling of plasmonic nanostructures.

## ACKNOWLEDGEMENTS

I would first like to thank my advisor, Professor Teri W. Odom for her dedicated, patient and excellent mentoring in the past five years. Teri is a very reasonable and supportive advisor, who cares about the students and trusts the students a lot. Teri provided her strongest support to me during my difficult time and helped me continue my graduate school in Northwestern University. I sincerely appreciate to be one of her students and I learned a lot from her both from research and life. Teri always gives her students a lot of freedom in terms of initiating and processing a project. She is very patient to listen to the students' ideas and opinions and share her precious advice with us. Teri likes to train students, and she respects us from bottom of her heart. When I meet difficulties in my project, Teri always encourages me to think deeply and provides me with plenty of resources to help me pursue various exciting projects. Teri has extremely high requirements of writing and presenting skills, which benefit my job career in future. Besides academic support, Teri is a role model for me to learn how to communicate and get along well with other people. It is the greatest honor I ever have for being part of "the Odom's Group". Teri makes me become not only more insightful but also much softer person, which would be cherished for my whole personal life.

I would like to acknowledge my Ph.D. thesis and qualifying exam committee members - Professor George C. Schatz, Professor Richard D. Schaller, Professor Mark C. Hersam and Professor Kenneth R. Shull - for their critical reviews and insightful suggestions on my research work. I also appreciated much the advice from Professor Jiaying Huang on my graduate life. I would like to thank my undergraduate advisors Professor Yujie Xiong at University of Science and Technology of China and summer school mentor Yi Cui from Stanford University, who

provided me with research opportunities and help on applying for graduate school, which inspired my great interests in research and science.

I want to like to express my gratitude to my collaborators, who have made all my projects possible. Professor Richard D. Schaller from Argonne National Lab provided endless assistance on my experiments in Argonne in terms of optical set up and data analysis. He is always passionate and knowledgeable in a wide range of research fields. The fruitful discussions with Professor George C. Schatz motivate me to conduct my projects with deeper understanding. I would also like to thank my collaborators Dr. Weijia Wang, Dr. Michael Kundson, Dr. Danqing Wang, Dr. Jun Guan, Dr. Marc R. Bourgeois, Dr. Cherqui Charles, Dr. Thaddeus Reese, Dr Xitlali Juarez, Dr. Jingtian Hu, Dr Alexander Sample with their hard work and tremendous contributions. The interdisciplinary collaborations let me learn faster and brainstorm more exciting ideas.

My earnest thanks to all the Odom group members, who provide a comfortable working environment. I appreciate the willingness for discussions and offering suggestions from the Odom group members. In the meanwhile, I want to thank Lindsay Haukebo for her great administrative help. She always responds fast and helps with organizing our group, making our research life much easier.

My friends from undergraduate university to graduate school, have been one of my greatest and the most reliable source of support and assistance. Lin Sun, Weizi Yuan, Liangjie Wu, Jue Chen, Shikai Deng, Bowei Zhang, Tingting Zheng, Qingyun Wan, Manman Chu, Qianqian Li, Yuan Li, Heguang Liu, Jinsong Wu, Yue Yin, Qinyuan Lin, Yaoyao Chen, Jiazhen Chen, Haoxiang Yang, Xiankai Yu, Ruiyun Huang, Furui Zhang, Yuehan Yao make my life happy and joyful. The memories and experience with them are inestimable gift for me.

Finally, I would like to express gratitude to my families. My father Wei Li and mother Suhua Tang have been providing their unconditioned love, understanding and support to me in pursuing my dream. They are not scientists, but they emphasize the importance of education and critical thinking. They give me high level of freedom that I can do whatever I would like to try, and they are my strongest back support. They teach me to always be optimistic and passionate towards life. Lastly, and significantly, I owe thanks to a very special person, my lovely husband, Xiong Wang for his continued love, support and understanding during my pursuit of my Ph.D degree. His accompany, his smiles and his belief in me, which are invaluable, always make my life brighter. Thank you all.

## List of Abbreviations

SPP	Surface Plasmon Polariton
LSP	Localized Surface Plasmon
NP	Nanoparticle
SLR	Surface Lattice Resonance
DL	Dipole Lattice Plasmons
HQL	Hybrid Quadrupole Lattice Plasmons
D-Q	Dipole-Quadrupole
Q-Factor	Quality Factor
CDA	Coupled Dipole Approximation
RA	Raley Anomaly
FWHM	Full Width at Half Maximum
TE	Transverse Electric
TM	Transverse Magnetic
SEM	Scanning Electron Microscopy
LDOS	Local Density of States
FDTD	Finite-difference Time-domain
PSP	Phase-Shifting Photolithography
PEEL	PSP + Etching + Electron-beam evaporation + Lift-off
SANE	Solvent Assisted Nanoscale Embossing
PDMS	Poly(dimethyl siloxane)
DMSO	Dimethyl Sulfoxide

NIR	Near-Infrared
CCD	Charge-coupled Device
BZ	Brillouin Zone
QD	Quantum Dots
Uv-vis	Ultra-violet
BEM	Boundary Element Method

## Table of Contents

ABSTRACT.....	5
ACKNOWLEDGEMENTS.....	7
List of Abbreviations.....	8
List of Figures.....	12
<b>Chapter 1. Plasmonic Modes Engineering with Plasmonic Nanostructures on Stretchable Substrate.....</b>	<b>20</b>
1.1 Background of Plasmonic Mode Engineering.....	21
1.2 Al NP Arrays Imbedded into PDMS Fabrication.....	22
1.3 Optical Response of Al NP Arrays under Stretching.....	23
1.3.1 Design of Stretching process.....	23
1.3.2 Optical Response of Al NP Arrays with Excitation Polarization Along Stretching Direction.....	24
1.3.3 Optical Response of Al NP Arrays with Excitation Polarization Perpendicular to Stretching Direction.....	27
1.4 Summary and Outlook.....	29
<b>Chapter 2. Plasmon Nanolasing with Aluminum Nanoparticle Arrays.....</b>	<b>30</b>
2.1 Introduction.....	31
2.2 Dipole Lattice Plasmon Nanolasing from Al and Au NP arrays.....	32
2.3 Ultrafast Dynamics of Dipole Lattice Plasmon Nanolasing from Al and Au NP arrays.....	35
2.4 Quadrupole Lattice Plasmon Nanolasing from Al and Au NP arrays.....	39
2.4 Ultrafast Dynamics of Quadrupole Lattice Plasmon Nanolasing from Al and Au NP arrays.....	45
2.6 Summary and Outlook.....	47
2.7 Methods.....	47

	11
<b>Chapter 3. Plasmonic Nanolaser over Full Visible-Color Range</b> .....	50
3.1 Introduction.....	51
3.2 Individual Lasing Emission from Plasmonic Square Arrays .....	53
3.3 Multi-color Lasing Emission in Square Arrays .....	57
3.4 Blue, Green and Red Color Lasing by Stacking Two Square Lattices .....	59
3.5 Plasmonic Lasing Emitted from Off-normal Directions.....	63
3.6 Summary and Outlook .....	67
3.7 Methods.....	68
<b>Chapter 4. Hierarchical Hybridization in Plasmonic Honeycomb Lattices</b> .....	69
4.1 Introduction.....	70
4.2 Hybridized $\Gamma_1$ Mode in Plasmonic Honeycomb Lattice .....	72
4.3 Dipole-Quadrupole Coupling at $\Gamma_1$ Mode.....	75
4.4 Dipole-Quadrupole Coupling for Lasing from Honeycomb Lattices .....	78
4.5 Lasing from Two Distinct Band Edge State .....	80
4.6 Summary and Outlook .....	83
4.7 Methods.....	84
<b>Chapter 5. M-point Lasing in Hexagonal and Honeycomb Plasmonic Lattices</b> .....	86
5.1 Introduction.....	87
5.2 Out-of-plane Dipole Coupling at M-point in Hexagonal Lattice.....	89
5.3 M-point Lasing from Hexagonal Lattice .....	92
5.4 M-point Band-edge State from Honeycomb Lattice.....	94
5.5 M-point Lasing from Honeycomb Lattice .....	97
5.6 Summary and Outlook .....	98
5.7 Methods.....	99
Reference .....	101
CV (Ran Li) .....	108

## List of Figures

<b>Figure 1.1. Overall fabrication process of patterning Al NP arrays into PMDS.</b> .....	<b>22</b>
<b>Figure 1.2. Al NP arrays with optimized size and homogeneous stretching. (a)</b> SEM images shown Al NP diameter is around 230 nm with 450 nm periodicity. <b>(b)</b> SEM images under larger scale shown uniform Al NP lattice. <b>(c)</b> Optical images of stretched soft PDMS with Al NP imbedded with strain value inserted upper left. ....	<b>23</b>
<b>Figure 1.3. Experimental and FDTD simulation results show consistent change of quadrupolar and dipolar modes.</b> .....	<b>24</b>
<b>Figure 1.4. Charge distribution of different plasmon modes marked with number indicating higher order quadrupolar mode appearance.</b> .....	<b>26</b>
<b>Figure 1.5. Experimental and FDTD simulation results of Al NP arrays under polarization direction normal to stretching condition.</b> .....	<b>27</b>
<b>Figure 1.6. Quadrupolar mode confirmation and evolution relationship with (0,1) diffraction mode. (a)</b> FDTD simulated transmission spectra under certain strain value. <b>(b)</b> Charge distribution at position denoted in (a). <b>(c)</b> Quadrupolar resonance position followed (0,1) diffraction mode. ....	<b>28</b>
<b>Figure 2.1. Dipole lattice plasmon (DL) nanolasing from Al and Au nanoparticles (NPs). (a)</b> SEM images of Au and Al NP array (NP spacing $a_0 = 580$ nm, average diameter $d = 110$ nm with height $h = 50$ nm). <b>(b)</b> The DL modes of Al and Au NP arrays overlapped with the red side of LDS 765 dye emission. Transmission spectra of Au was shifted down 30%. The lasing spectrum of Au NPs was shifted down for clarity. <b>(c)</b> Charge distribution of Al and Au NP at DL resonances (Au: 844 nm, Al: 840 nm). Measured emission spectra with Al NP array <b>(d)</b> and Au NP array <b>(e)</b> with increased pump power (concentration $C = 4$ mM, solvent: DMSO). Light-light curves were inserted. ....	<b>33</b>
<b>Figure 2.2. Near-field electric intensity distributions of Al and Au NPs at DL resonance.</b> .....	<b>34</b>

- Figure 2.3. Beam profiles showed directional and confined DL lasing spot from Al and Au NP arrays ( $< 1^\circ$  divergence angle). .....34**
- Figure 2.4. Time-correlated single-photon counting of LDS 765 dye ( $C = 4$  mM) dissolved in DMSO suggested around 400 ps decay lifetime. ....35**
- Figure 2.5 Power-dependent lasing dynamics for DL modes.** Time-correlated single-photon counting images (wavelength range: 800 nm to 820 nm) and corresponding processed data showing lasing decay lifetime for DL lasing from Al and Au NP arrays **(a)** around threshold and **(b)** at highest pump power ( $0.61 \text{ mJ/cm}^2$ ). .....36
- Figure 2.6. Simulated DL lasing from Al NPs dynamics under different pump powers. (a)** Power-dependent population inversion changes with time of DL lasing from Al NPs. **(b)** Spatial distributions of stimulated and spontaneous emission rates above DL lasing from Al NPs threshold. Scale bar is 100 nm. ....37
- Figure 2.7. Power- and time- dependent population inversion evolution of Au DL lasing...38**
- Figure 2.8. Hybrid quadrupole lattice plasmon (HQL) nanolasing from Al and Au NP arrays. (a)** SEM images of Al and Au NP array (NP spacing  $a_0 = 560$  nm, average diameter  $d = 220$  nm with height  $h = 120$  nm **(b)** The HQL modes of Al and Au NP arrays overlapped with the red side of LDS 765 dye emission. Transmission spectra of Au was shifted down 30%. The lasing spectrum of Au NPs was shifted down for clarity). **(c)** Charge distribution of Al and Au NP at HQL resonances (Au: 813 nm, Al: 809 nm). Measured emission spectra with Al NP array **(d)** and Au NP array **(e)** with increased pump power (concentration  $C = 4$  mM, solvent: DMSO). Light-light curves were inserted. ....39
- Figure 2.9. Cross-SEM images of Al NP array show the truncated cone structure. (scale bar is  $1 \mu\text{m}$ ) .....40**
- Figure 2.10. Al and Au NP arrays both can support sharp HQL resonances.** Transmission spectra of fabricated Al and Au NP arrays at HQL modes. The spectrum of Au NP array was shifted up 40% for clarification. ....40

<b>Figure 2.11. Extinction of single Al and Au NP (diameter <math>d = 220</math> nm, height <math>h = 120</math> nm). The quadrupole and dipole localized surface plasmons of single Al NP are both shorter in wavelength than those of Au NP. ....</b>	<b>41</b>
<b>Figure 2.12. Distinct energy dissipation channels of Al and Au NP arrays. (a) Scattering spectra and (b) Absorption spectra of Al and Au NP arrays. Spectra for Au NPs was shifted up 30% along y axis. ....</b>	<b>42</b>
<b>Figure 2.13. Beam profiles showed directional and confined HQL lasing spots from Al and Au NP arrays (<math>&lt; 1^\circ</math> divergence angle). ....</b>	<b>43</b>
<b>Figure 2.14. Au NP array showed stronger near-field intensity than Al NP array at HQL resonance. ....</b>	<b>43</b>
<b>Figure 2.15. Simulated emission intensity at different mark positions near NPs (10 nm away from NP edge and 20 nm away from NP edge). ....</b>	<b>44</b>
<b>Figure 2.16. Power-dependent lasing dynamics for HQL lasing. Time-correlated single-photon counting images (wavelength range from bottom to top: 800 nm to 820 nm) and corresponding processed data showing lasing decay lifetime for HQL lasing from Al and Au NPs (a) around threshold and (b) at highest pump power (<math>0.96 \text{ mJ/cm}^2</math>). ....</b>	<b>45</b>
<b>Figure 2.17. Power-dependent population inversion changes over time for HQL lasing. (a) Power-dependent population inversion changes over time for Au and Al HQL lasing. (b) Spatial distributions of stimulated and spontaneous emission rates above (top panel) and below (bottom panel) Al HQL lasing threshold. ....</b>	<b>46</b>
<b>Figure 3.1. Fano-type <math>\Gamma_{11}</math> and <math>\Gamma_{10}</math> Resonances in Plasmonic Square Lattice. (a) SEM image of fabricated square lattice (<math>a_0 = 450</math> nm) of Al NPs with 60 nm diameter and 50 nm height. (b) Scheme of realizing red and blue lasing emission with Al NP array under 400 nm wavelength femtosecond pump. (c) Calculated and measured transmission spectra of lattice in (a) for x-polarized plane waves at the <math>\Gamma</math> point showing strong SRL <math>\Gamma_{11}</math> and <math>\Gamma_{10}</math>. Lasing supported by <math>\Gamma_{11}</math> and <math>\Gamma_{10}</math> modes was achieved by incorporating spectrally overlapped dye solutions. ....</b>	<b>53</b>

**Figure 3.2. Near-field distributions at  $\Gamma_{11}$  and  $\Gamma_{10}$  Resonance.** (a) Calculated electric field magnitude within the XY plane of square lattice excited at  $\Gamma_{11}$  mode showing symmetric spatial distributions characteristic. (b) Calculated phase mapping at  $\Gamma_{11}$  mode. (c) Calculated electric field magnitude within the XY plane of square lattice excited at  $\Gamma_{10}$  mode showing dipolar coupling. (d) Calculated phase mapping at  $\Gamma_{10}$  mode.....54

**Figure 3.3. Lasing Characterizations Supported by  $\Gamma_{11}$  and  $\Gamma_{10}$  Resonance.** (a)  $\Gamma_{11}$  lasing output profiles. (b) Light-light curve of  $\Gamma_{11}$  lasing showing threshold value of 0.61 mJ/cm<sup>2</sup>. (c)  $\Gamma_{10}$  lasing out-put profiles with increasing pump powers. (d) Light-light curve of  $\Gamma_{11}$  lasing showing threshold value of 0.33 mJ/cm<sup>2</sup>.....55

**Figure 3.4. Angle-resolved emission of (a)  $\Gamma_{11}$  and (b)  $\Gamma_{10}$  lasing shows the directionality of lasing.** .....56

**Figure 3.5.  $\Gamma_{11}$  and  $\Gamma_{10}$  Lasing Emissions from Plasmonic Square Lattice.** (a) Scheme of mixing two dye solutions and achieve  $\Gamma_{11}$  and  $\Gamma_{10}$  lasers simultaneously. (b) Measured lasing spectra by incorporating mixed dye solutions with different volume ratios. ....57

**Figure 3.6: PL of mixed dye shows two peaks at 464 nm and 645 nm.** .....58

**Figure 3.7. The  $\Gamma$  Mode from Al NPs in 350 nm periodicity square lattice supports lasing at 514 nm when incorporating with 20mM C500 Dye-DMSO solution onto NP array.** .....59

**Figure 3.8. The three dye mixed solution shows PL emission from 440 nm to 740 nm wavelength range with two PL peaks at 501 nm and 642 nm.** .....60

**Figure 3.9. Multi-color Lasing Emission from Stacking Two Plasmonic Square Lattice.** (a) Scheme of stacking two square lattices with different rotational angles ( $\varphi$ ). (b) Transmission spectra from stacking two plasmonic square lattice with different  $\varphi$  values. (c) Scheme of measuring lasing emissions and device design. (d) Measured laser emission output with the three mixed dye solutions. Measured lasing spectra by incorporating mixed dye solutions with different volume ratios. ....61

**Figure 3.10. Individual PL and absorption spectra of three dye solutions.** .....62

**Figure 3.11. Multi-color Lasing Emission from Plasmonic Square Lattice.** (a) Measured dispersion diagram of Al NPs in square lattice under different polarization angles of incident light at different geometries. (b) Scheme of measuring lasing emission from off-normal high-symmetry directions. Measured angle-resolved emission of Al NPs in square lattice from (c)  $\Gamma$ -X and (d)  $\Gamma$ -M directions. Measured lasing spectra by incorporating mixed dye solutions with different volume ratios. (e) Representative lasing spectra from off-normal high-symmetry points. (f) The spatial distributions of lasers corresponding to the Brillouin zones (BZ). (g) Photos of laser beams showing similar spatial distributions of lasers in (f). .....64

**Figure 3.12. The spectral comparison between X-point lasing emission and transmission spectra near X-point under (a) TM and (b) TE excitations of incident light.** .....65

**Figure 3.13. The spectral comparison between off-normal lasing emission and transmission spectra near the high-symmetry points.** (a)  $\Delta_2$ -point lasing, (b)  $\Delta$ -point lasing, (c) M-point lasing. ....66

**Figure 4.1. Hybridized  $\Gamma_1$  Mode in Plasmonic Honeycomb Lattice.** (a) Scheme of a honeycomb lattice with two NPs per unit cell (outlined). Red and blue sites belong to hexagonal sublattices  $L_1$  and  $L_2$ , respectively. (b) SEM image of fabricated honeycomb lattice ( $a_0 = 400$  nm) of Ag NPs with  $d = 110$  nm and  $h = 50$  nm. (c) Calculated and measured transmission spectra of lattice in (b) for  $x$ -polarized plane waves at the  $\Gamma$  point showing strong SLR  $\Gamma_1$ . (d) Calculated (left) and measured (right) dispersion diagram (angle-dependent transmission of TM polarized plane wave) for the lattice in (b) along the  $\Gamma - M$  path through the Brillouin zone. (e) Calculated electric field magnitude within the  $xy$  plane of honeycomb unit cell excited at  $\lambda_{\Gamma_1}$  showing asymmetric spatial distributions characteristic of multipolar LSP superposition. ....72

**Figure 4.2.  $\Gamma_1$  SLR in hexagonal lattice.** (a)  $\Gamma$  point  $x$ -polarized transmission spectra for honeycomb and hexagonal lattices calculated using FDTD. (b) Calculated electric field magnitude, normalized to that of the incident field, of  $\Gamma_1$  SLR within the XY plane of hexagonal lattice unit cell. (c) Figure 1e of the main text reproduced for comparison with panel b). ....73

**Figure 4.3. Hierarchical Hybridization at  $\Gamma_1$  Resonance.** (a) Calculated extinction spectra of isolated Ag disks ( $d = 110$  nm and  $h = 50$  nm) excited by plane waves with incident wave vector

$\mathbf{k}$  parallel (green) and perpendicular (black) to the disk symmetry axis. The dipole mode  $D_{\parallel}$  is excited in both cases, while the in-plane quadrupole  $Q_{\parallel}$  is not excited with  $\mathbf{k}$  directed along the z-axis. Note that the mode near 3.0 eV under  $k_y$ ,  $E_x$  plane wave excitation is an electric octupole mode that does not noticeably contribute to the near-fields shown in Figure 1e. **(b)** Calculated electric fields associated with  $D_{\parallel}$  and  $Q_{\parallel}$  modes of the isolated disk projected onto the surface normal  $\hat{\mathbf{n}}$  highlighting different near-field spatial distributions. **(c)** Hierarchical hybridization scheme showing the  $\Gamma_1$  mode of the honeycomb lattice involves D-Q mixing on both sublattice (vertical) and unit cell (horizontal) levels. Red and blue colors correspond to positive and negative induced surface charges, respectively. ....75

**Figure 4.4. The spectral profiles of the Ag NP ( $d = 110$  nm;  $h = 50$  nm) dimer (dashed) closely match those of the isolated Ag NP (solid) after normalizing the former by a factor of 2 to account for the particle number.** Deviations from the single-particle responses are small due to the 400 nm center-to-center distance between NPs in the dimer structure. The trace colors correspond to the plane wave excitation conditions in Figure 4.3 of the main text. Explicitly, red and blue traces correspond to incident plane waves polarized along short- and long-axes of the disc respectively. ....76

**Figure 4.5. Dipole – Quadrupole Coupling Supports Lasing at  $\Gamma_1$  Mode.** **(a)** Lattice mode (black) spectrally overlapped with PL of IR 140 dye solution (light blue). The lasing emission spectrum (red) exhibits characteristic linewidth narrowing close to the  $\Gamma_1$  mode of the lattice. **(b)** Calculated spatial distribution maps of the stimulated ( $\frac{1}{\hbar\omega_a} E \frac{dP_a}{dt}$ ) and spontaneous ( $N_2/\tau_{21}$ ) emission rates when lasing occurred in units of  $s^{-1}\cdot m^{-3}$ . The stimulated emission spatial distribution matches that of the Q mode in Figure 4.3b. ....78

**Figure 4.6.  $\Gamma_1$  lasing characterization from Ag NP lattice.** **(a)** Light-light curve of  $\Gamma_1$  lasing and power-dependent emission FWHM. Lasing intensities and linewidths are plotted on linear and logarithmic scales, respectively. **(b)** Angle-resolved emission of  $\Gamma_1$  lasing. ....79

**Figure 4.7. Simulated  $\Gamma_1$  lasing emission peak matches wavelength of  $\Gamma_1$  resonance in the absence of dye. Calculation details included in the main text. ....80**

**Figure 4.8. Lasing Supported by Two Distinct Band Edge States.** (a) Measured transmission spectrum of Al NP ( $d = 110$  nm,  $h = 100$  nm) honeycomb lattice showing simultaneously optimized  $\Gamma_1$  and  $\Gamma_2$  modes. (b) Calculated electric field magnitude normalized by magnitude of incoming field ( $|\mathbf{E}|^2/|\mathbf{E}_0|^2$ ) and phase profile of the  $\Gamma_2$  mode. Scale bars are 100 nm. (c) Dispersion diagram of Al NP array under TM polarization. The white dashed line denotes the edge of dispersion diagram which is limited by the areas of fabricated NP array in experiments. (d) Measured  $\Gamma_2$  emission spectra with increasing pump power for Al NP array (LDS 473 dye concentration 20 mM). (e) Measured  $\Gamma_1$  emission spectra with increasing pump power for Al NP array (IR-140 dye concentration 0.5 mM). .....81

**Figure 4.9: Charge distributions at  $\Gamma_2$  resonance showing the charge accumulated at four corners of Al nanoparticles.** .....82

**Figure 4.10: The Bragg mode (denoted by the dash line) related to  $\Gamma_2$  resonance coupled with out-of-plane quadrupole localized surface plasmon.** .....82

**Figure 4.11: Light-light curve and angle-resolved emission suggested that  $\Gamma_2$  lasing happened at zero wavevector.** (a) Input-output curves of  $\Gamma_2$  lasing. (b) Angle-resolved emission spectra measured from  $0^\circ$  to  $3^\circ$ . .....83

**Figure 5.1. M-point Band-edge State in Plasmonic Hexagonal Lattice.** (a) SEM image of fabricated hexagonal lattice ( $a_0 = 400$  nm) of Ag NPs with 80 nm diameter and 50 nm height. (b) Reciprocal space with Brillouin zone of hexagonal lattice. (c) Calculated (left) and measured (right) dispersion diagram (angle-dependent transmission of TM polarized plane wave) for the lattice in (a) along the  $\Gamma - M$  path through the Brillouin zone. .....89

**Figure 5.2. Out-of-plane dipole coupling at  $SLR_M$ .** (a) Measured and calculated transmission spectra of lattice in Figure 1a for x-polarized plane waves at  $60^\circ$  excitation angle showing strong  $SLR_M$ . (b) Calculated electric field magnitude and (d) phase map within the XY and XZ plane of hexagonal Ag NP array showing out-of-plane dipole resonance (c) Calculated charge distribution of Ag NPs at  $SLR_M$  showing charge accumulates at the diagonal corners of NPs. .....90

**Figure 5.3. Photoluminescence of C-540 dye dissolved into DMSO centers at 536 nm wavelength. ....91**

**Figure 5.4. Out-of-plane Dipole Coupling Supports Lasing at SLR<sub>M</sub> Mode of Hexagonal Lattice. (a) SLR<sub>M</sub> lasing at 583 nm emission out-put of Ag NP array with PL of C540 dye solution. The lasing signal was detected at 59°. (b) Angle-resolved emission mapping shows that the SLR<sub>M</sub> lasing from Ag NP array emitted at  $9.2 \text{ um}^{-1}$  ( $\sim 59^\circ$ ). (c) Scheme of SLR<sub>M</sub> lasing emission from hexagonal array. (d) Imaged SLR<sub>M</sub> laser spots indicating the six-fold symmetry of SLR<sub>M</sub> lasing. ....93**

**Figure 5.6. Mode Splitting at the M-point of Plasmonic Honeycomb Lattice. (a) SEM image of fabricated honeycomb lattice ( $a_0 = 346 \text{ nm}$ ) of Ag NPs with 100 nm diameter and 50 nm height. (b) Measured dispersion diagram (angle-dependent transmission of TM polarized plane wave) for the lattice in (a) along the  $\Gamma - M$  path through the Brillouin zone. (c) Measured and calculated transmission spectra of lattice in (a) for x-polarized plane waves with  $60^\circ$  excitation angle showing two SLR<sub>M</sub> resonances (shown in the zoomed-in image). (d) Near-field electric distributions indicates the hybridization between out-of-plane dipole and out-of-plane quadrupole resonance at M1. (e) Near-field electric distributions shows the in-plane dipole coupling at M2. ....94**

**Figure 5.8. Simulated transmission spectra at  $60^\circ$  from honeycomb lattice. (a) Sweeping the NP diameter and fixing NP height to be 50 nm. (b) Sweeping the NP height and fixing diameter to be 100 nm. ....95**

**Figure 5.7. Phase mapping of M1 and M2 modes. ....96**

**Figure 5.9. M-point Lasing from Plasmonic Honeycomb Lattice. (a) M1 lasing at 868 nm emission out-put of Ag NP array with PL of IR140 dye solution. The lasing signals were detected at  $58^\circ$ . (b) Angle-resolved emission mapping shows that the SLR<sub>M</sub> lasing from Ag NP honeycomb lattice emitted at  $6.2 \text{ um}^{-1}$  ( $\sim 58^\circ$ ). ....97**

**Figure 5.10: Light-light curve of SLR<sub>M</sub> lasing from honeycomb lattice. ....98**

# Chapter 1. Plasmonic Modes Engineering with Plasmonic Nanostructures on Stretchable Substrate

## Abstract

This chapter describes the change of optical response by mechanically stretching the plasmonic Al NPs in square lattice. We optimized a fabrication process to fabricate Al NP arrays imbedded into a thin PDMS substrate for dynamically tuning lattice geometries. Under TE or TM excitation of incident light, the plasmonic Al NP arrays present different linear properties and charge distributions at the same stretching value. Out-of-plane quadrupole and in-plane dipole coupling are both involved during stretching process. We demonstrate how the polarization of excitation direction and lattice geometry play a role in the coupling mechanisms and optical response of plasmonic nanostructures.

## 1.1 Background of Plasmonic Mode Engineering

When an incident light excites at the metal thin film with dielectric layer on the top of it, there is resonant oscillation of conduction electrons at the interface between metal layer and dielectric layer, which is defined as surface plasmon polaritons (SPP).<sup>1</sup> Furthermore, when the plasmonic materials exist in terms of small nanoparticles, the electrons tend to be confined around the nanoparticles, resulted in localized surface plasmon (LSP).<sup>1</sup> Nowadays, plasmonic materials have many applications in varied fields, such as SPR immunoassay<sup>2</sup>, fluorescence enhancement<sup>3</sup> and photocatalysis enhancement<sup>4</sup>. However, for unstructured plasmonic materials, they suffer from huge radiative loss and lose beam directionality when coupled with fluorescence materials. To solve this problem, previous work has fabricated plasmonic nanoparticle (NP) arrays embedded into uniform refractive index environment. The strong dipole-dipole coupling resulted in high quality lattice plasmon mode in near-infrared range (IR).<sup>5</sup> Moreover, by changing the geometry of NP lattice from infinite array to superlattice, previous work has been able to engineer the plasmon mode from single mode to multiple modes.<sup>6</sup>

For commonly used plasmonic materials, such as Au and Ag, they showed very high quality of plasmonic effect in the IR range. But in visible range, they suffer from huge plasmonic loss due to their interband transition in visible range.<sup>7</sup> Meanwhile, Al showed very good plasmonic properties from ultra-violet to visible range due to its interband transition at 800 nm.<sup>7</sup> Previous work in our group has reported high-quality lattice plasmon mode at visible range with full-width at half-maximum around 5 nm.<sup>7</sup> More interestingly, our group developed a strategy for fabricating Al NP hexagonal arrays into PDMS for engineering plasmonic mode.<sup>7</sup> In that work, we proposed the quadrupole mode with large Al NP size. However, hexagonal array lattice is complicated to

investigate the origin of quadrupole mode. Here we propose to investigate the plasmonic Al NP square arrays to further study the evolution of mode coupling under mechanical stretching, including both the dipolar and quadrupolar lattice modes.

## 1.2 Al NP Arrays Imbedded into PDMS Fabrication

**Figure 1.1** describes the overall fabrication process of patterning Al NP arrays into PDMS to create a uniform refractive index environment (1.4). First, we spin coat photoresist (PR) layer on

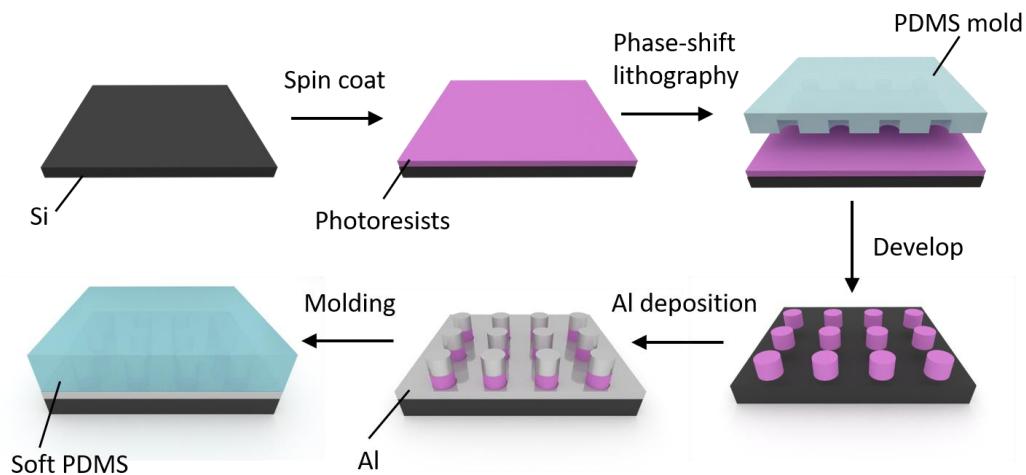


**Figure 1.1. Overall fabrication process of patterning Al NP arrays into PMDS**

top of Si wafer, then we put a PDMS mold on the PR layer and expose the entire system under ultra-visible (UV) light. After developing the exposed PR, we can remove the PR residue between patterned PR posts. Then we use e-beam evaporation to deposit 40 nm Al layer on the PR posts. After that, we pour soft PDMS on top of the sample and cure for 1.5 hours. Due to the strong adhesion between Al layer and Si wafer, weak adhesion between PR and Si, Al NP can be peeled off during peeling soft PDMS while the Al layer is still attached on Si wafer. Eventually, we can

obtain periodic Al NP arrays embed into soft PDMS. In this work, we fabricated 450 nm periodicity Al NP with optimized size to investigate the plasmon mode evolution under stretching.

### 1.3 Optical Response of Al NP Arrays under Stretching

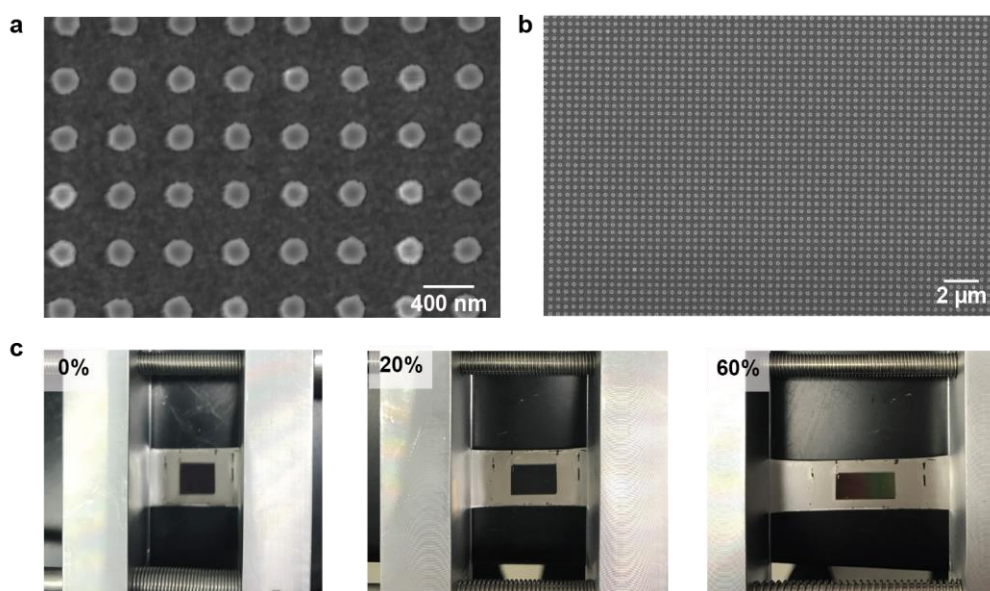


**Figure 1.2. Al NP arrays with optimized size and homogeneous stretching.** (a) SEM images shown Al NP diameter is around 230 nm with 450 nm periodicity. (b) SEM images under larger scale shown uniform Al NP lattice. (c) Optical images of stretched soft PDMS with Al NP imbedded with strain value inserted upper left.

#### 1.3.1 Design of Stretching process

Based on finite-difference time-domain (FDTD) simulation results, the sharpest quadrupole mode of Al NP arrays with 450 nm periodicity happens when the diameter of Al NP is around 230 nm. By optimizing the fabrication condition, we successfully fabricated the Al NP arrays with 230 nm diameter. **Figure 1.2.a and b** showed the scanning electron microscopy (SEM) images,

indicating the diameter of Al NP is around 230 nm and periodicity is 450 nm as expected. By optimizing the stretcher, we have achieved a very homogeneous stretching even under higher stretch strain. As shown in Figure 1.2.c, the shape of patterned area was changing homogeneously along stretching direction and there was no obvious distortion in the transverse direction.

By aligning polarization of incident light along stretching direction and changing strain value from 0% to 60%, we measured the transmission spectra with Al NP arrays imbedded into soft PDMS. In the meanwhile, we used FDTD simulation to simulate the transmission spectra of Al NP arrays under different strain. Here we used Poisson ratio ( $\gamma$ ) of 0.5, to calculate the periodicity change normal to stretching condition. The equations are shown as below:

$$l_f = l_0 \times (1 + \varepsilon) \quad (1.1)$$

$$l_t = l_0 \times (1 - \gamma \times \varepsilon) \quad (1.2)$$

$l_0$  is the original periodicity of Al NP arrays,  $\varepsilon$  is the strain,  $l_f$  is the periodicity along the stretching direction,  $l_t$  is the periodicity transverse to the stretching direction,  $\gamma$  is the Poisson ratio of soft PDMS. For the simulation, we set the refractive index environment to be 1.4, which is the refractive index of soft PDMS.

### 1.3.2 Optical Response of Al NP Arrays with Excitation Polarization Along Stretching Direction

Figure 1.3.a and b showed the transmission spectra of stretched Al NP arrays from experiments and FDTD simulation. Here the polarization direction of incident light was parallel to the stretching direction. Compared with experimental result and FDTD simulation, there was a very sharp peak at 632 nm, indicating the existence of quadrupolar mode. Along with increasing

strain value, the periodicity along stretching direction (here we defined as x direction for convenience) increased, when the (1,0) diffraction mode went to the red side of dipolar resonance, it can couple with dipolar resonance, which results in (1,0) lattice plasmon mode. With increasing strain, the (1,0) lattice plasmon mode red shifted following the movement of (1,0) diffraction mode. On the other hand, for the y direction, with increasing strain, the periodicity along y direction decreased, leading blue shift of (0,1) diffraction mode. Since (0,1) diffraction mode was on the blue side of dipole resonance, it couldn't couple with dipole, resulting in a peak near the dipolar resonance. More interestingly, when the strain value increased to 50%, another Fano-type interference (asymmetrical spectral feature) appeared at 473 nm, indicating the appearance of a new plasmon mode. This position was near to the (2,0) diffraction mode, which meant this mode

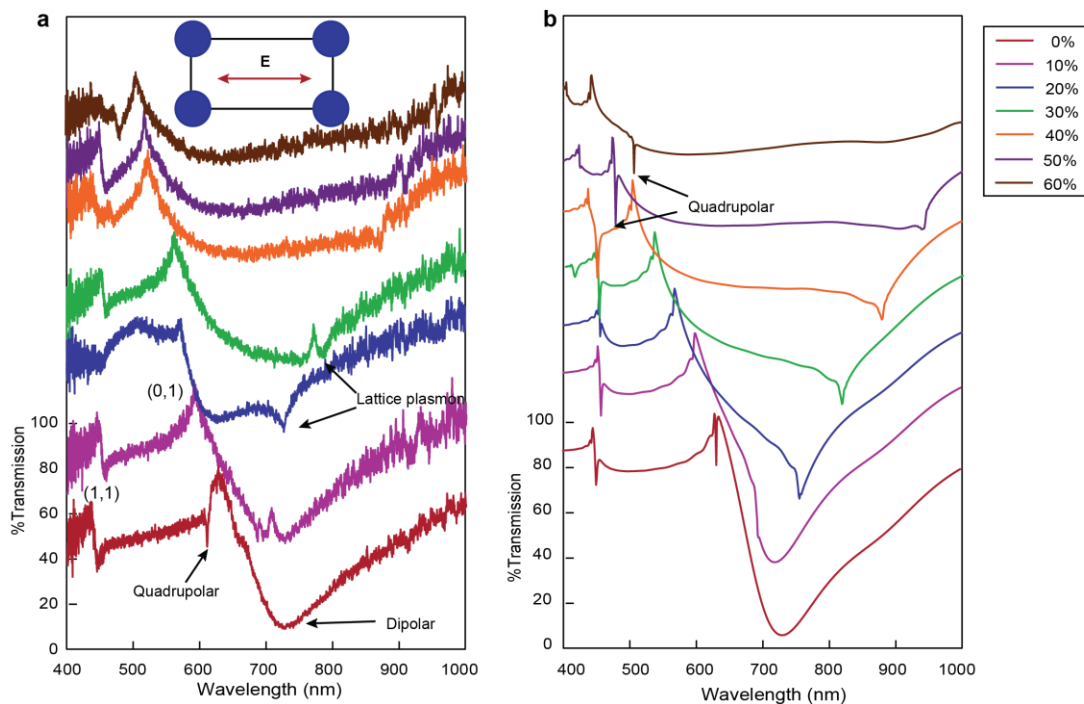


**Figure 1.3. Experimental and FDTD simulation results show consistent change of quadrupolar and dipolar modes.**

coupled with (2,0) diffraction mode. With increasing strain value to 60%, this new plasmon mode red shifted to 504 nm, which was exactly the (2,0) diffraction mode under 60% strain. Therefore, we investigated the charge distribution at these two positions and compared them with the charge distribution of original quadrupolar and dipolar resonance.

**Figure 1.4.** showed the charge distribution of quadrupolar (1) and lattice plasmon mode (2).

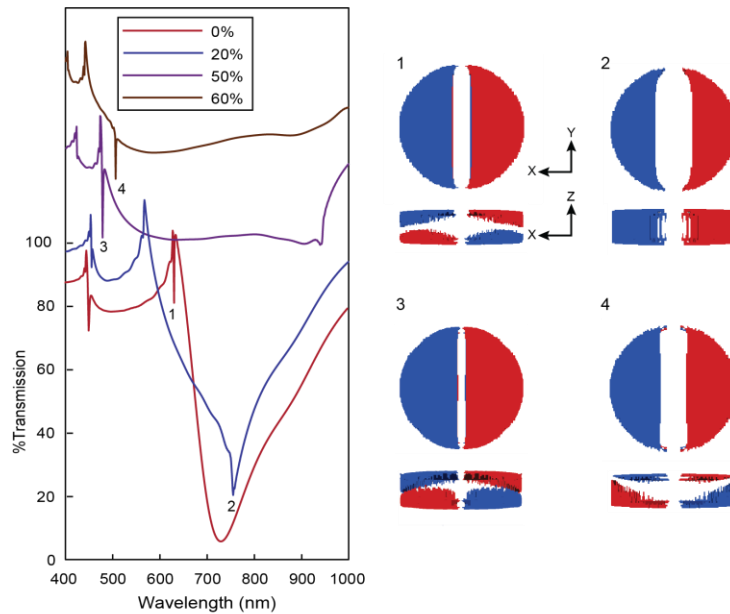


**Figure 1.4. Charge distribution of different plasmon modes marked with number indicating higher order quadrupolar mode appearance.**

Compared with lattice plasmon mode, which is in-plane coupling, quadrupolar mode tended to couple at xz plane. Therefore, quadrupolar mode is out-of-plane coupling, which is subradiant. Since the coupling was confined around the cross-section of NP, the symmetric quadrupolar mode should be a dark mode that was not supposed to be detected in far-field. Considering that the movement of quadrupolar mode at high strain condition followed the diffraction mode along polarization direction, we proposed that this out-of-plane quadrupolar mode was coupled with

(1,0) diffraction mode to be observed more obviously at far-field. To further confirm our conclusion, we conducted experiments with polarization direction normal to the stretching direction.

### 1.3.3 Optical Response of Al NP Arrays with Excitation Polarization

#### Perpendicular to Stretching Direction

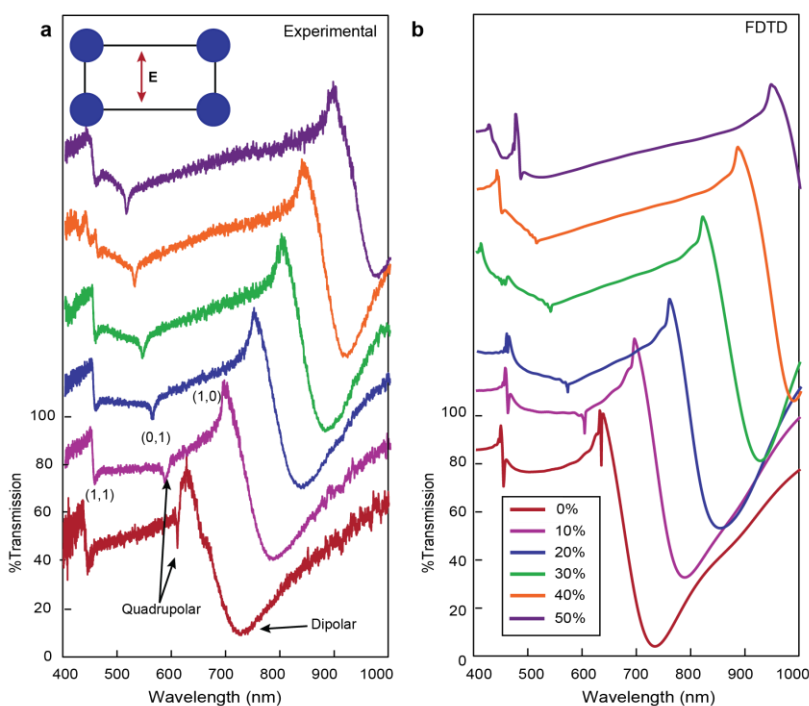


**Figure 1.5. Experimental and FDTD simulation results of Al NP arrays under polarization direction normal to stretching condition.**

Figure 1.5 showed the transmission spectra of Al NP arrays with different stretch strain when the polarization of incident light normal to the stretching direction. With increased strain, the periodicity at x direction increased, resulted in (1,0) diffraction mode red shifted. In this situation, since the polarization was along y axis, the diffraction mode that dominated dipolar resonance was

(1,0) diffraction mode. Therefore, the dipole resonance red shifted with increasing strain value. On the other hand, there was another mode blue shifting with increasing strain. To further explain the evolution of this mode, we investigated the charge distribution of this mode and its relationship with (0,1) diffraction mode.

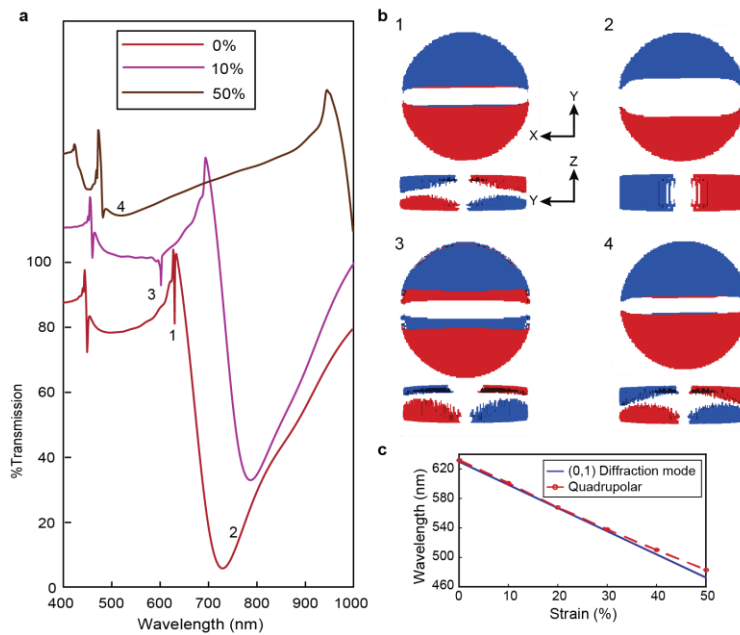


**Figure 1.6. Quadrupolar mode confirmation and evolution relationship with (0,1) diffraction mode.** (a) FDTD simulated transmission spectra under certain strain value. (b) Charge distribution at position denoted in (a). (c) Quadrupolar resonance position followed (0,1) diffraction mode.

**Figure 1.6.** shows the charge distributions at different distinct plasmonic modes. We looked at four different plasmonic modes as shown in **Figure 1.6a**. Respectively, plasmonic mode 1 shows out-of-plane quadrupole coupling and plasmonic mode 2 shows in-plane dipole coupling. Under stretching value of 10%, we observed out-of-plane quadrupole coupling with stronger net-dipole moment at plasmonic mode 3. Further stretching leads to the appearance of plasmonic mode 4,

and the charge calculations suggest it is out-of-plane quadrupole coupling (**Figure 1.6b**) Moreover, the evolution of (0,1) diffraction mode under stretching matches with the wavelength of quadrupolar resonance. This suggests that when the stretching direction is normal to the polarization direction of excitation light, the quadrupolar LSP tends to couple to the (0,1) diffraction mode to form HQL.

## 1.4 Summary and Outlook

In conclusion, by changing direction between the polarization and stretching, we investigated the evolution of quadrupolar and lattice plasmon. ‘Dark’ quadrupolar resonance turned to be visible by coupling the diffraction mode along the polarization direction. Furthermore, unlike lattice plasmon mode case that can only couple with the red side of dipolar, quadrupolar mode only happens at the blue side of the dipolar resonance and could be from coupling with higher diffraction mode. The extra net dipole moment existing in the out-of-plane quadrupole resonance coupled to the diffraction mode to make the resonance ‘bright’. We demonstrate evolution of the plasmonic modes towards the dynamic change of lattice geometry, and we hope it can be beneficial for applications like bio-sensing and multiplexing displays.

## Chapter 2. Plasmon Nanolasing with Aluminum Nanoparticle Arrays

### Abstract

This chapter compares plasmon nanolasing and corresponding ultrafast dynamics supported by Al and Au nanoparticle arrays. By tuning nanoparticle size, we achieved high-quality surface lattice resonances from both dipolar lattice plasmons and hybrid quadrupolar lattice plasmons at near-infrared wavelengths. We demonstrated that the dipolar and hybrid quadrupolar lattice modes can serve as optical feedback for plasmonic nanolasing. Even at the wavelength of its interband transition, Al showed nanolasing properties similar to Au. Also, independent of the type of cavity mode used as optical feedback, Al lattice plasmon lasing showed thresholds and ultrafast dynamics similar to Au.

### Related reference

**Li, R.;** Wang, D.; Guan, J.; Wang, W.; Ao, X.; Schatz, G. C.; Schaller, R.; Odom, T. W., Plasmon nanolasing with aluminum nanoparticle arrays. *JOSA B* **2019**, *36* (7), E104-E111.

## 2.1 Introduction

Metal nanoparticles (NPs) can support localized surface plasmon (LSP) resonances, where the electromagnetic field is confined at the surface of the particle.<sup>8</sup> Depending on NP size, dipolar and multipolar LSP resonances, such as quadrupolar LSPs, can be excited.<sup>9</sup> When arrays of metal NPs are of appropriate dimensions in a uniform refractive index environment, the LSPs of the individual NPs and the Bragg mode defined by the lattice geometry can produce different types of lattice plasmon modes<sup>5, 7, 10-11</sup>. For example, dipolar lattice plasmon (DL) modes or hybrid quadrupolar plasmon (HQL) modes can be achieved when the dipole or quadrupole LSP resonance couples to the diffraction mode.<sup>5, 7</sup> Radiative losses of plasmonic NPs can be suppressed, which results in narrow lattice resonances with high mode quality at the band edge.<sup>5</sup> Besides the sharp DL modes produced in plasmonic NP arrays, HQLs can be realized by increasing the NP size, and the smaller net-dipole moments result in less radiative loss compared to the DL mode.<sup>7, 12</sup>

Plasmonic nanocavity array lasers have relied on Au and Ag materials because these metals support high-quality lattice plasmons at near-infrared (NIR) wavelengths.<sup>5, 13-15</sup> Organic gain incorporated with plasmonic NP arrays can result in directional nanolasing at room temperature.<sup>5, 16-17</sup> Al is an alternative plasmonic material whose real part of the dielectric function  $\text{Re}\{\epsilon\}$  is negative at NIR, but whose imaginary part  $\text{Im}\{\epsilon\}$  is more than 20 times larger than Au and Ag. Hence, absorption losses are dominated by radiative damping.<sup>18</sup> Different from Au and Ag NPs that exhibit large losses at ultra-violet and visible wavelengths,<sup>5, 7, 12, 19</sup> Al NPs support plasmon resonances of uniform quality across this range despite its interband transition (1.5 eV,  $\sim 800$  nm).<sup>20-22</sup> Although sharp DL and HQL resonances from Al NP arrays have been reported,<sup>7</sup> whether Al can be used as a nanocavity material for NIR plasmonic nanolasing is an open question.

Here we show Al NP arrays can support high-quality lattice plasmon modes as optical feedback for nanoscale lasing. Al and Au NP arrays with similar lattices and particle sizes produced sharp DL modes at the optical band edge. DL lasing from Al NP arrays had lasing thresholds comparable to Au NP arrays. Ultrafast dynamics also showed that DL lasing from Al NP arrays had decay lifetimes and rise times similar to those from Au NPs. Simulations using a four-level gain system in the time domain agreed with experiment in the shortening of lasing decay lifetime and rise time under high pump powers. Finally, arrays of Al and Au NPs with larger particle sizes showed sharp HQL resonances, and HQL lasing from Al arrays had threshold behaviors and ultrafast dynamics similar to Au NP arrays.

## 2.2 Dipole Lattice Plasmon Nanolasing from Al and Au NP arrays

We used the soft nanofabrication process PEEL<sup>23-24</sup> to fabricate cylindrical Al and Au NP arrays on silica substrates (**Figure 2.1a**, NP spacing  $a_0 = 580$  nm, average diameter  $d = 110$  nm, height  $h = 50$  nm). To match the refractive index of the superstrate with the substrate, we used the solvent dimethyl sulfoxide (DMSO) ( $n = 1.44$ ). In transmission spectra, we observed sharp modes from both Al and Au NP arrays (**Figure 2.1b**,  $\lambda_{\text{Al}} = 840$  nm,  $\lambda_{\text{Au}} = 844$  nm). The resonance  $\lambda_{\text{Al}}$  in Al NP arrays is shorter in wavelength than  $\lambda_{\text{Au}}$  because of the higher-energy LSP of Al NPs. The full-width half-maximum (FWHM,  $\Delta\lambda$ ) of this mode was ca. 5 nm, corresponding to a quality factor ( $Q = \lambda/\Delta\lambda$ )  $> 160$ . Calculated charge distributions confirmed that the collective mode was a dipolar lattice plasmon (DL) because of the in-plane separation of positive and negative charge in the NPs at resonance (**Figure 2.1c**). Electric field distributions showed that Al NPs had near-field enhancement ( $|E|^2 \sim 400$ ) similar to Au NPs at the DL resonance (**Figure 2.2**).

To compare lasing from DL resonances in Al and Au, we put a droplet of LDS-765-DMSO (4 mM) solution on top of the NP arrays and pumped LDS-765 dye with 600 nm, 1kHz operation rate and 35-fs pulse width light under transverse electric (TE) polarization. The circular pump spot was

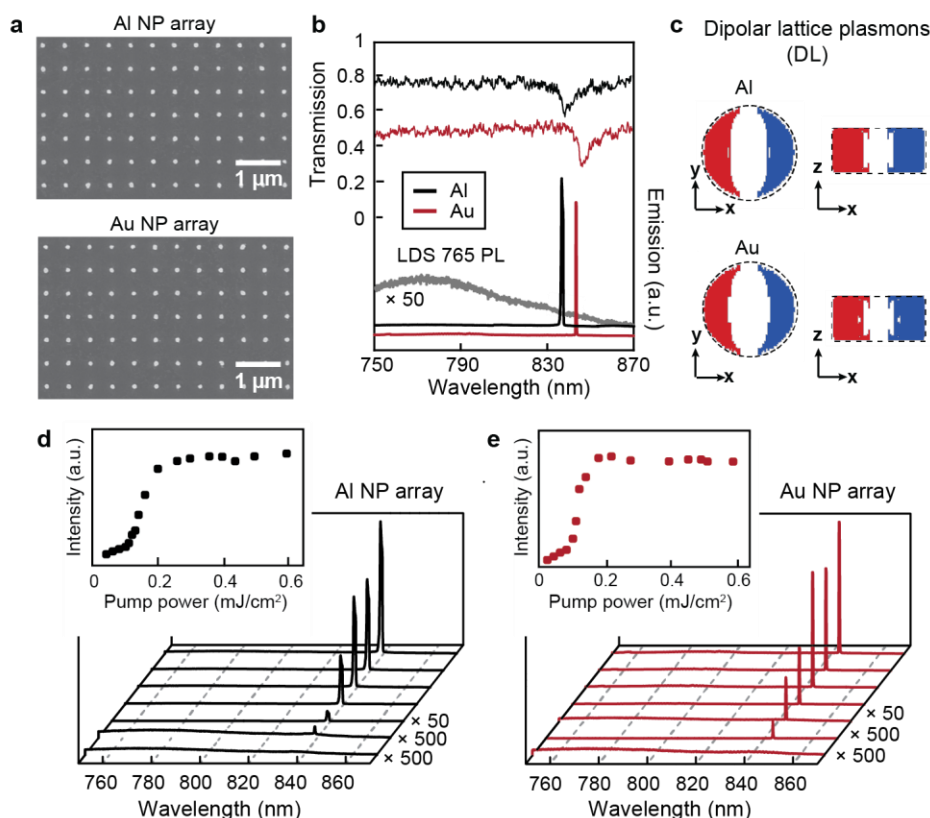


**Figure 2.1. Dipole lattice plasmon (DL) nanolasing from Al and Au nanoparticles (NPs).**

(a) SEM images of Au and Al NP array (NP spacing  $a_0 = 580$  nm, average diameter  $d = 110$  nm with height  $h = 50$  nm). (b) The DL modes of Al and Au NP arrays overlapped with the red side of LDS 765 dye emission. Transmission spectra of Au was shifted down 30%. The lasing spectrum of Au NPs was shifted down for clarity. (c) Charge distribution of Al and Au NP at DL resonances (Au: 844 nm, Al: 840 nm). Measured emission spectra with Al NP array (d) and Au NP array (e) with increased pump power (concentration  $C = 4$  mM, solvent: DMSO). Light-light curves were inserted.

~800 μm in diameter. With an incident angle of 45°, lasing signals were collected at the sample

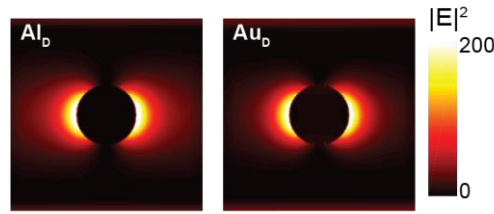


**Figure 2.2. Near-field electric intensity distributions of Al and Au NPs at DL resonance.**

surface normal and analyzed by a charge-coupled device (CCD) spectrometer (LN<sub>2</sub>-cooled CCD/Triax 552, Horiba Jobin Yvon, ~0.15 nm resolution). A high-resolution CCD beam profiler (LBR-HR, Newport, 1.4 Megapixel) was used to detect the far-field emission patterns. Collecting the emission signals normal to the surface, we observed a narrow lasing peak (FWHM  $\approx$  0.5 nm) at  $\lambda_{\text{Al}} = 839$  nm close to the DL resonance (**Figure 2.1b**). Lasing emission with similar characteristics and narrow linewidths (FWHM  $\approx$  0.4 nm,  $\lambda_{\text{Au}} = 843$  nm) was observed from Au

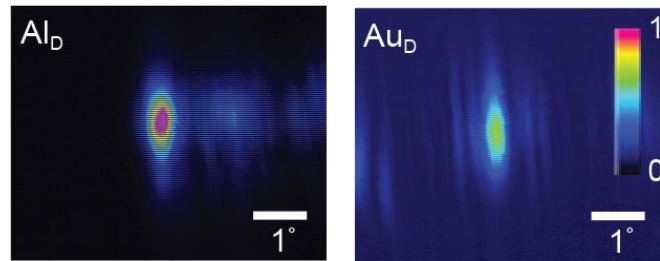


**Figure 2.3. Beam profiles showed directional and confined DL lasing spot from Al and Au NP arrays ( $< 1^\circ$  divergence angle).**

NP arrays (Figure 2.1b). The FWHM of lasing from DL cavity modes in Al NP arrays was broader than that from Au possibly because of metal NP quality, where Al NPs were fabricated by electron-beam deposition and had rougher surfaces compared to Au NPs prepared by thermal deposition. The light-light curve for DL lasing from Au NPs revealed that the lasing threshold was ca. 0.10 mJ/cm<sup>2</sup>, similar to the threshold of DL lasing from Al NPs (0.11 mJ/cm<sup>2</sup>) (**Figures 2.1d-e**). The

comparable thresholds of DL lasing from Al and Au NPs can be attributed to their similar near-field intensities at the DL modes, which is related to the stimulated emission rate.<sup>25</sup> Far-field beam profile measurements for DL lasing from Al and Au NPs showed a directional and confined output beam spot with  $<1^\circ$  beam divergence (**Figure 2.3**).

### 2.3 Ultrafast Dynamics of Dipole Lattice Plasmon Nanolasing from Al and Au NP arrays

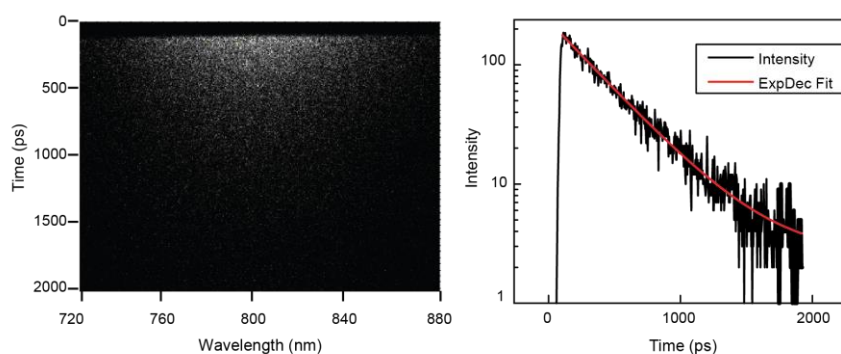


**Figure 2.4. Time-correlated single-photon counting of LDS 765 dye ( $C = 4$  mM) dissolved in DMSO suggested around 400 ps decay lifetime.**

Time-correlated single-photon counting was used to reveal the DL lasing dynamics in Al and Au NP arrays. Under pulsed laser excitation, the emissions from the sample were coupled into a spectrograph and a streak camera was synchronized to the 1 kHz repetition rate of the pump laser. Integration times of 0.5 seconds allowed averaging over several nanolaser pulse signals. Streak camera data was binned by wavelength with an 8-nm bin width around laser mode. Decay lifetime data was obtained by fitting collected data to a single exponential decay function  $y = y_0 + Ae^{-\frac{(x-x_0)}{t}}$ .

LDS 765 dye dissolved in DMSO exhibited photoluminescence with an intrinsic decay lifetime  $\sim 400$  ps (**Figure 2.4**), consistent with prior reports ( $\sim 300$  ps).<sup>26</sup> Around threshold, the photon decay lifetime from DL lasing was significantly shortened because of the dominant stimulated emission process, which is faster than spontaneous emission.<sup>17, 27</sup> Above lasing threshold, the

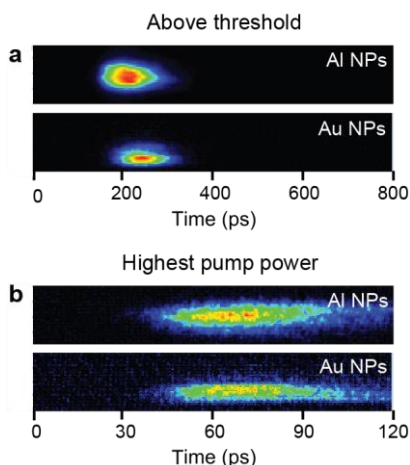


**Figure 2.5. Power-dependent lasing dynamics for DL modes.** Time-correlated single-photon counting images (wavelength range: 800 nm to 820 nm) and corresponding processed data showing lasing decay lifetime for DL lasing from Al and Au NP arrays (**a**) around threshold and (**b**) at highest pump power ( $0.61 \text{ mJ/cm}^2$ ).

decay lifetime of the DL lasing from Al NPs was 44 ps and 54 ps from Au NPs (**Figures 2.5a**). Since the decay lifetime of lasing emission partially captures the ability of the cavity to trap photons, the longer lifetime of the DL lasing from Au NPs indicates that Au NPs at the DL resonance had photon-trapping abilities higher than Al NPs.<sup>28-29</sup> At high pump power ( $0.61 \text{ mJ/cm}^2$ ), we chose a short time window (120 ps) to resolve the fast decay lifetime. The decay lifetime of Al and Au could not be fit due to the long rise time and short time window range (Fig. S5b); however, the rise time for DL lasing from Al arrays (20 ps) was shorter than that from Au arrays (25 ps) (**Figure 2.5b**), which suggests faster lasing build-up of DL lasing from Al NP arrays compared to Au NPs. We attribute these effects to Al NPs having lower non-radiative loss at 600

nm (pump wavelength)<sup>30-31</sup>, which can confine more energy into the hot spots. Overall, for DL lasing, we observed that the lasing lifetime and rise time decreased with increased pump power

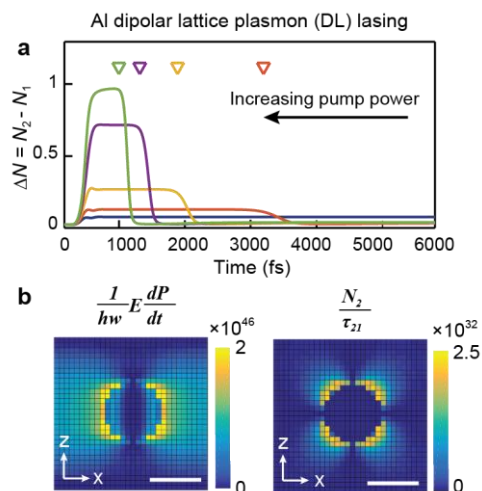


**Figure 2.6. Simulated DL lasing from Al NPs dynamics under different pump powers.** (a) Power-dependent population inversion changes with time of DL lasing from Al NPs. (b) Spatial distributions of stimulated and spontaneous emission rates above DL lasing from Al NPs threshold. Scale bar is 100 nm.

because high pump powers increase energy transfer rates between dye molecules and plasmonic NPs.

To understand dynamics of DL lasing, we used a four-level gain system and finite-difference time-domain (FDTD) methods to simulate DL lasing and change in population inversion ( $\Delta N = N_2 - N_1$ ) over time<sup>17</sup>. After a 300-fs optical pulse,  $\Delta N$  started to build up and then depleted with the onset of lasing. Therefore, decreased  $\Delta N$  can represent the start of energy transfer from dye molecules to DL plasmons. With increased pump power, we found that  $\Delta N$  of DL lasing decreased faster for both Al or Au NPs (**Figures 2.6a, 2.7**), which indicates shortening of the lasing rise time and decay lifetime, consistent with experiments (Figure. 2.5). Compared with photonic lasers, where lasing occurs in bulk regions of gain, lasing buildup in lattice plasmon nanolasers is

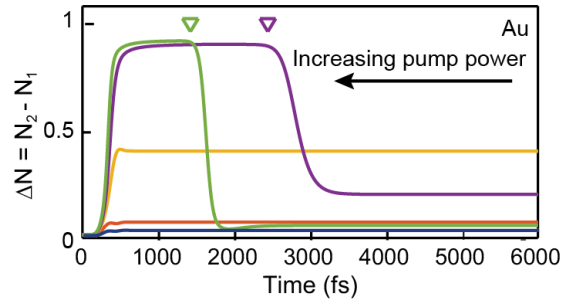


**Figure 2.7. Power- and time- dependent population inversion evolution of Au DL lasing.**

localized to the sub-wavelength vicinity around the NPs.<sup>32</sup> High stimulated emission rates ( $\frac{1}{h\nu} E \frac{dP}{dt}$ ) were observed at the hot spots near the NPs (**Figure 2.6b**), where the strong near fields ( $|E|^2$ ) enhanced the stimulated emission rate by a factor of  $|E|^2$ .<sup>33</sup> Because the onset of lasing depleted the  $\Delta N$  at the dipolar hot spots, the spontaneous emission rate ( $\frac{N_2}{\tau_{21}}$ ) was lowered significantly, which showed more than 12 orders of magnitude lower intensity than that of stimulated emission rate and was located at regions outside of the dipolar hot spots (Figure 2.6b).

## 2.4 Quadrupole Lattice Plasmon Nanolasing from Al and Au NP arrays

At larger NP sizes (and the same lattice spacing), hybrid quadrupole lattice plasmons (HQLs) can form.<sup>7, 12</sup> Different from the in-plane coupling DL mode, the HQL originates from an out-of-plane LSP coupled to the Bragg mode and enables stretchable devices.<sup>7, 12</sup> To fabricate arrays of

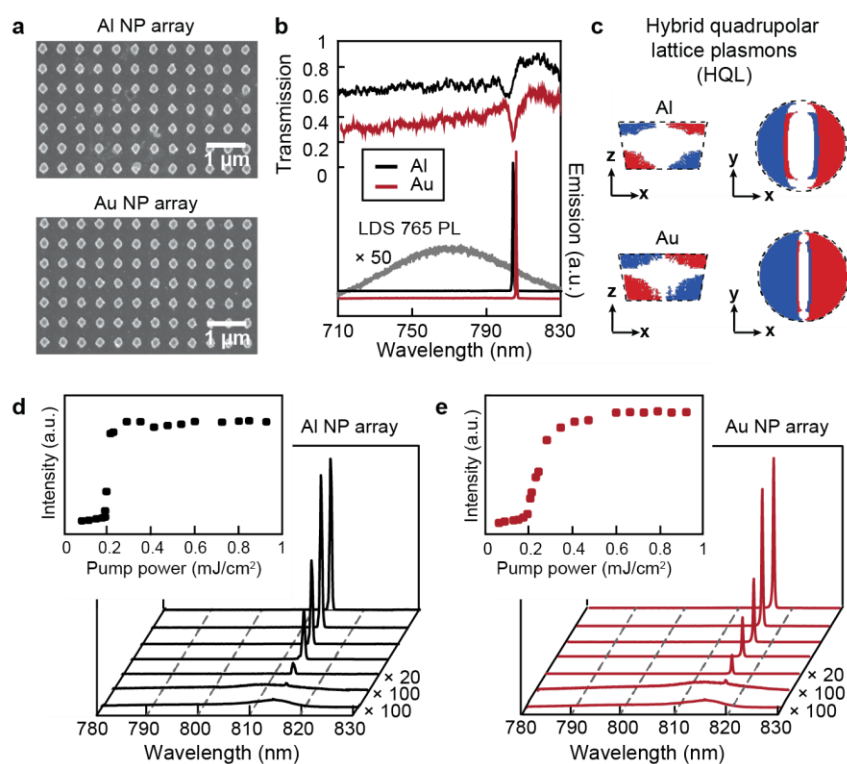


**Figure 2.8. Hybrid quadrupole lattice plasmon (HQL) nanolasing from Al and Au NP arrays.** (a) SEM images of Al and Au NP array (NP spacing  $a_0 = 560$  nm, average diameter  $d = 220$  nm with height  $h = 120$  nm) (b) The HQL modes of Al and Au NP arrays overlapped with the red side of LDS 765 dye emission. Transmission spectra of Au was shifted down 30%. The lasing spectrum of Au NPs was shifted down for clarity). (c) Charge distribution of Al and Au NP at HQL resonances (Au: 813 nm, Al: 809 nm). Measured emission spectra with Al NP array (d) and Au NP array (e) with increased pump power (concentration  $C = 4$  mM, solvent: DMSO). Light-light curves were inserted.

Al and Au NPs with larger particle sizes (NP spacing  $a_0 = 560$  nm, average diameter  $d = 220$  nm, height  $h = 120$  nm), we used solvent-assisted nanoscale embossing (SANE)<sup>34</sup> followed by PEEL (**Figure 2.8a**). Cross-sectional SEM images showed that larger NPs had a truncated cone structure because of shrinkage in Au hole sizes in the mask during metal deposition (**Figure 2.9**). In transmission spectra, Al NP arrays showed a sharp HQL resonance at 809 nm, and Au NP arrays showed a sharp resonance at 813 nm with high quality factor ( $\sim 200$ ) (**Figure 2.8b, 2.10**). In contrast, the width of DL modes of Al and Au NP of these larger particles was broader than HQL

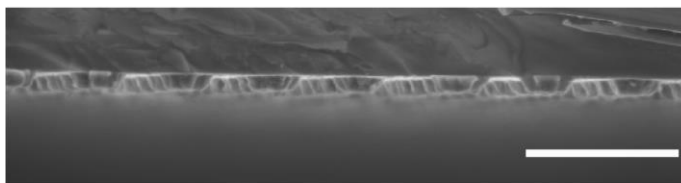


**Figure 2.9.** Cross-SEM images of Al NP array show the truncated cone structure. (scale bar is 1  $\mu\text{m}$ )

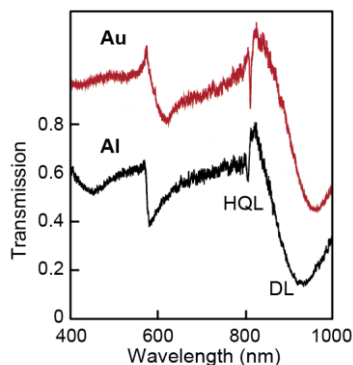


**Figure 2.10.** Al and Au NP arrays both can support sharp HQL resonances. Transmission spectra of fabricated Al and Au NP arrays at HQL modes. The spectrum of Au NP array was shifted up 40% for clarification.

modes because the coupling between dipole LSP resonances and Bragg mode was not optimized (**Figure 2.11**). The DL resonance wavelength for Au NP arrays is at wavelengths longer than Al

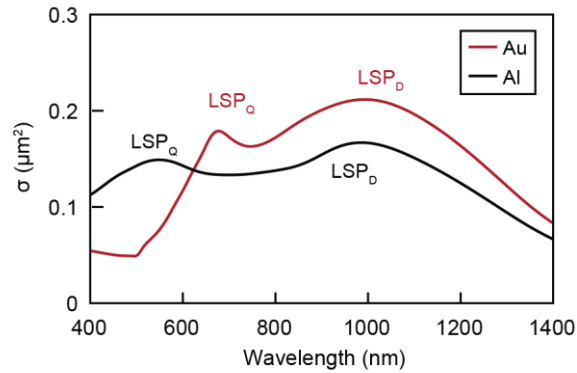


**Figure 2.11. Extinction of single Al and Au NP (diameter  $d = 220$  nm, height  $h = 120$  nm). The quadrupole and dipole localized surface plasmons of single Al NP are both shorter in wavelength than those of Au NP.**

NP arrays because the LSP dipolar resonance of single Au NPs (997 nm) is red-shifted compared to Al NPs (982 nm) (Figure 2.10). The simulated charge plots reveal an asymmetric charge distribution along  $z$  for both Al and Au NP arrays at the HQL resonances, which results in a dipole moment at facilitate radiation into the far field (**Fig. 2.8c**).

To identify energy dissipation channels of Al and Au HQLs, we used FDTD simulations to calculate the scattering and absorption spectra of Al and Au NP arrays at normal incidence. The scattering spectra provides a measure of radiative damping in the system, and absorption spectra represents non-radiative damping. For Au NP arrays at the HQL resonance, extinction spectra of the band-edge lattice plasmon ( $\lambda_{\text{Au}} = 817 \text{ nm}$ ) had nearly equal contributions from scattering and absorption (**Figure 2.12**). In contrast, for Al NPs at the HQL resonance ( $\lambda_{\text{Al}} = 814 \text{ nm}$ ), the non-

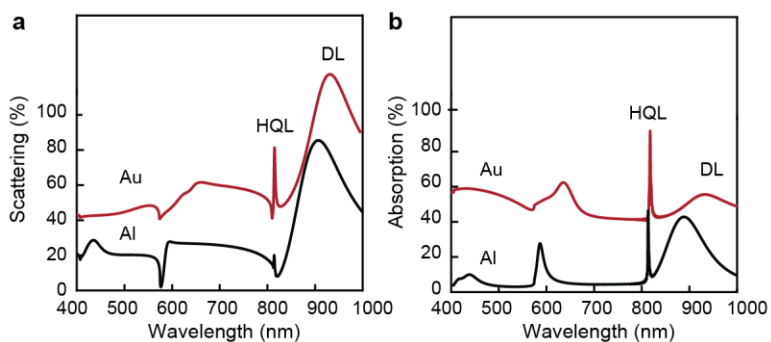


**Figure 2.12. Distinct energy dissipation channels of Al and Au NP arrays.** (a) Scattering spectra and (b) Absorption spectra of Al and Au NP arrays. Spectra for Au NPs was shifted up 30% along y axis.

radiative energy dissipation contributed mostly to the extinction, while radiative dissipation was minor (**Figure 2.12**), which indicates that the dominate radiative damping term for Al NPs was suppressed by lattice coupling.

To investigate the lasing emission process from HQL modes in different plasmonic materials, we put a droplet of LDS-765-DMSO (4 mM) solution on top of the NP arrays on a silica substrate

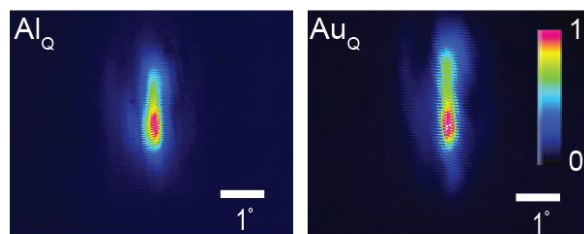


**Figure 2.13. Beam profiles showed directional and confined HQL lasing spots from Al and Au NP arrays ( $< 1^\circ$  divergence angle).**

and pumped the device under the same conditions as those for DL lasing. At the surface normal, a strong and narrow lasing signal at 813 nm from Al NP arrays was observed (**Fig. 2.8b**). Similarly, surface normal lasing emission at 816 nm was observed for Au NP arrays. The beam profile of HQL lasing was spatially coherent with emission having  $< 1^\circ$  divergence (**Figure 2.13**). Light curves showed that HQL lasing from Al NPs had comparable threshold values ( $0.22 \text{ mJ/cm}^2$ ) to that from Au NPs ( $0.20 \text{ mJ/cm}^2$ ) (**Figs. 2.8d-e**).

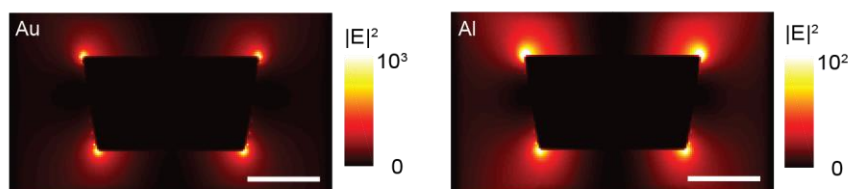


**Figure 2.14. Au NP array showed stronger near-field intensity than Al NP array at HQL resonance.**

To explain the similar thresholds between HQL lasing from Al NPs and Au NPs in experiments despite the stronger electric near-field distributions of Au NPs (**Figure 2.14**), we simulated how  $\Delta N$  changed in time in the hot spot regions and observed higher intensities at the pump wavelength

near Al NPs compared to Au NPs (**Figure. 2.15**). For a 600-nm pump, Al NPs tended to scatter more of the pump source while Au NP tended to absorb the pump because of differences in the interband transition between Al (~ 800 nm, 1.5 eV) and Au (~ 495 nm, 2.5eV). Therefore, higher

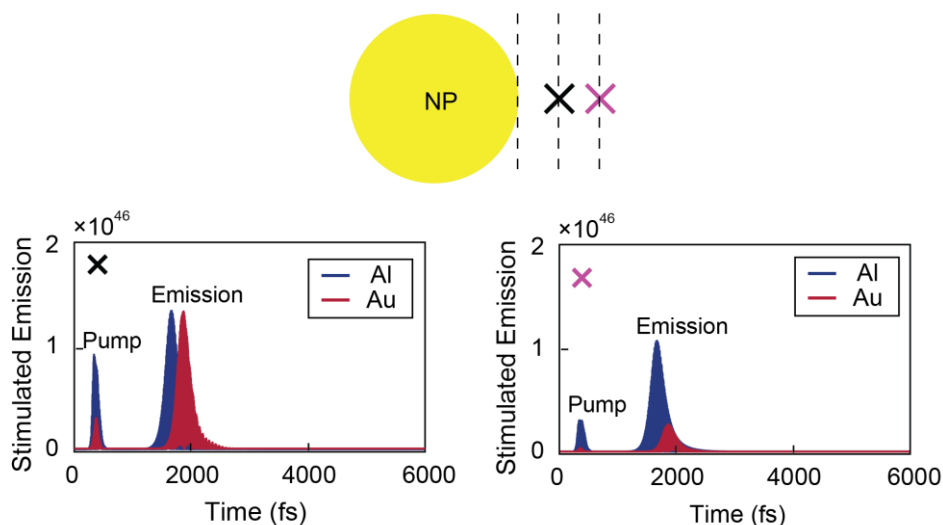


**Figure 2.15. Simulated emission intensity at different mark positions near NPs (10 nm away from NP edge and 20 nm away from NP edge).**

energy rate was available in the hot spot regions to excite the gain, which increased  $\Delta N$  depletion for HQL lasing from Al NPs and hence compensated for the weaker near fields of Al NPs. In experiment, HQL lasing from Al NPs had threshold values similar to HQL lasing from Au NPs possibly because the quality of the Al NPs was not as high as that of Au NPs.

## 2.5 Ultrafast Dynamics of Quadrupole Lattice Plasmon Nanolasing from Al and Au NP arrays

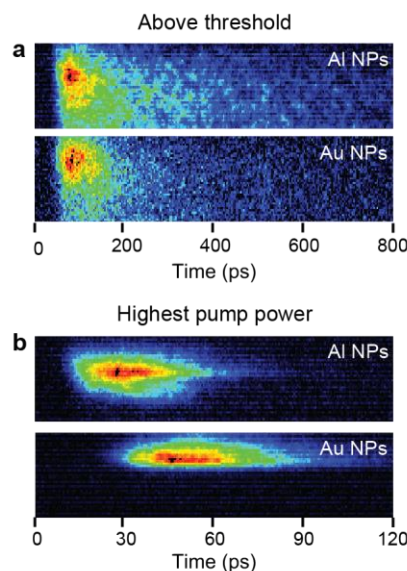


**Figure 2.16. Power-dependent lasing dynamics for HQL lasing.** Time-correlated single-photon counting images (wavelength range from bottom to top: 800 nm to 820 nm) and corresponding processed data showing lasing decay lifetime for HQL lasing from Al and Au NPs (a) around threshold and (b) at highest pump power ( $0.96 \text{ mJ/cm}^2$ ).

Similar to DL lasing, the decay lifetime of photons in HQL lasing was reduced due to the onset of the stimulated emission process. Pumped around threshold, the decay lifetime of HQL lasing from Al NPs (99 ps) was longer than that of Au (81 ps) (**Figure 2.16a**). At the highest pump power ( $0.96 \text{ mJ/cm}^2$ ), HQL lasing from Al NPs had a shorter decay lifetime (23 ps) than HQL lasing from Au NPs (37 ps) (**Figure 2.16b**), indicating a faster modulation speed than HQL lasing from Au NPs, and which is consistent with DL lasing performance. In terms of the lasing rise time, Al HQL modes enabled faster lasing build-up and shorter rise times than lasing from Au HQL modes. Independent of plasmonic material, shorter HQL lasing lifetimes and rise times were observed

with increased pump power in experiments (Figure 2.16b), in agreement with simulation results of HQL lasing dynamics (Figure 2.8 and Figure 2.17).

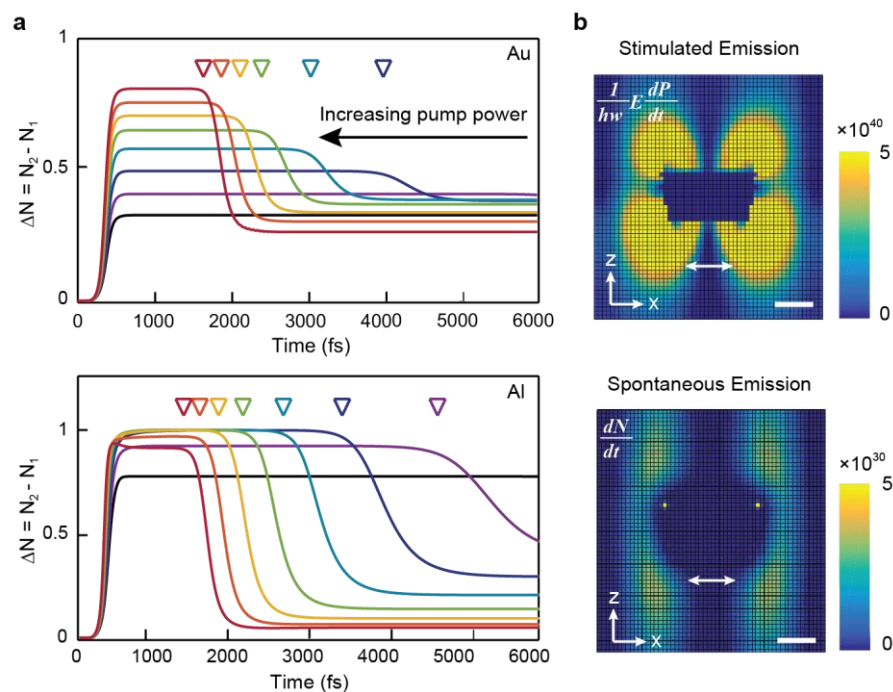


**Figure 2.17. Power-dependent population inversion changes over time for HQL lasing.**

(a) Power-dependent population inversion changes over time for Au and Al HQL lasing. (b) Spatial distributions of stimulated and spontaneous emission rates above (top panel) and below (bottom panel) Al HQL lasing threshold.

## 2.6 Summary and Outlook

In summary, we realized dipole lattice plasmon and hybrid quadrupole plasmon lasing with Al NP arrays. We found that lasing from Al arrays had comparable lasing threshold and decay lifetime with Au arrays for both DL and HQL modes. We identified that Al can be used for plasmon lasing at NIR wavelengths despite its weaker near-field intensity at resonance. Our results offer prospects to design plasmon nanolasers across the entire visible and NIR wavelength range. Because of the thermal stability and its native oxide, Al plasmon nanolasers can be potentially operated at higher temperatures and integrated into devices and architectures where noble metals are less desirable.

## 2.7 Methods

### 2.7.1 Fabrication of Al and Au NP arrays

Arrays of Al and Au NPs on fused silica were fabricated with a soft nanofabrication process referred to as PEEL.<sup>24</sup> Briefly, we generated periodic photoresist posts on Si wafers by phase-shifting photolithography (for small NP fabrication) or solvent-assisted nanoscale embossing (for large NP fabrication)<sup>34</sup> with controlled post size. The patterns were then transferred into free-standing Au nanohole films after Cr deposition, removal of PR posts, etching through the Si nanoholes, Au film deposition and lift-off of Au film. Finally, we created NP arrays by metal deposition (thermal deposition for Au and E-beam deposition for Al) through the hole-array mask on a transparent substrate and then use scotch tape to remove of the Au hole mask. A 2-nm Cr layer was deposited in-between for better adhesion between Au NPs and silica.

### 2.7.2 Lasing measurements

Al and Au NP arrays surrounded by LDS765-DMSO on silica were pumped with a mode-locked Ti:sapphire laser with a regenerative amplifier (600-nm wavelength, 1 kHz operation rate and 35-fs pulse width), and the circular pump spot was  $\sim 800$   $\mu\text{m}$  in diameter. With an incident angle of  $45^\circ$ , lasing signals were collected at the sample surface normal and analyzed by a charge-coupled device (CCD) spectrometer (LN<sub>2</sub>-cooled CCD/Triax 552, Horiba Jobin Yvon,  $\sim 0.15$  nm resolution). A high-resolution CCD beam profiler (LBR-HR, Newport, 1.4 Megapixel) was used to detect the far-field emission patterns.

### 2.7.3 Time-correlated single-photon counting

Under pulsed laser excitation, the emissions from the sample were coupled into a spectrograph and a streak camera was synchronized to the 1 kHz repetition rate of the pump laser. Integration times of 0.5 seconds allowed averaging over several nanolaser pulse signals. Streak camera data was binned by wavelength with an 8-nm bin width around laser mode. Decay lifetime data was obtained by fitting collected data to a single exponential decay function  $y = y_0 + Ae^{-\frac{(x-x_0)}{t}}$ .

### 2.7.4 FDTD simulations

FDTD calculations with commercial software (FDTD solution, Lumerical Inc., Vancouver, Canada) were used to simulate the linear optical properties and lasing emission from Al and Au NP arrays. The optical constants of Al were taken from Palik measurements (400–1000 nm).<sup>35</sup> The optical constants of Au were taken from Johnson and Christy measurements (400–1000 nm).<sup>36</sup> A uniform mesh size of 2 nm ( $x$ ,  $y$  and  $z$ ) was used to ensure the accuracy of electric and magnetic field calculations within the metal NPs.

Simulation of DL and HQL lasing was performed by FDTD, where a four-level one-electron model was integrated for modeling dye molecules. In the semi-quantum systems, we set the Al and Au NP size  $d = 110$  nm and height  $h = 50$  nm for DL and  $d = 220$  nm and height  $h = 120$  nm for HQL, dye concentration  $C = 4$  mM, pump wavelength at  $\lambda_a = 600$  nm and dye emission at  $\lambda_e = 780$  nm with bandwidth  $\Delta\lambda_e = 120$  nm, close to experimental conditions. The population inversion was analyzed to show the change of lasing dynamics with pump power. The spontaneous emission rate ( $N_2/\tau_{21}$ ) and stimulated emission rate ( $\frac{1}{\hbar\omega} \mathbf{E} \frac{d\mathbf{P}}{dt}$ ) were analyzed to show their spatial correlation with the plasmonic hot spots.

## **Chapter 3. Plasmonic Nanolaser over Full Visible-Color Range**

### **Abstract**

This paper reports a plasmonic laser device that can generate blue, green and red color lasers at the same time. We found that Al nanoparticles arranged in a square lattice can produce two high-quality surface lattice resonances (SLRs) at the  $\Gamma$  point. Mixing two different dyes can broaden the photoluminescence (PL) of gain to support blue and red color lasing emissions on the single square lattice of Al nanoparticles. Further, we designed an optical device, that is stacking two square lattices with different periodicities, to generate three SLRs in the blue, green and red color wavelength regime as optical feedbacks for lasing. By engineering the relative concentrations of three different dye solutions, we produced a gain material with broad PL to support blue, green and red color plasmonic nanolasing at the  $\Gamma$  point simultaneously.

### 3.1 Introduction

Manipulating lasing emissions over a wide range of wavelengths is advantageous because they can produce monochromatic colors to extend the color range and provide high output power.<sup>37-42</sup> Realizing multi-color lasing on a single device and tuning the laser color over the full visible spectra, especially achieving white color laser, are important for multiplexed optical communication, full-color laser displays, bio-imaging, and 3-D laser printing applications.<sup>43-46</sup> Multicolor lasers have been realized on different structures and devices, such as nanowires with microfiber hybrid structure, dual cavity vertical-cavity surface-emitting laser and microfluidic channels with mixed dye solution and cavity mirrors.<sup>47-51</sup> However, producing blue, green and red color lasers simultaneously is challenging because it requires advances in both gain materials and optical device designs.

Typical single compound semiconducting materials and organic dye molecules support narrow PL wavelength range ( $< 100$  nm), which cannot yield blue, green and red color lasers simultaneously. Recently, an upconversion core/shell/shell nanostructure was reported to enable white light emission.<sup>52</sup> However, the white light emission only happens at a certain pump power and it is difficult to couple upconversion nanostructures to a cavity mode to support white color lasing. In addition to gain material challenges, designing multiple cavity modes on a single device to produce blue, green and red color lasers concurrently from the same direction is difficult, because competitions between each lasing emission can occur.

Compared with semiconducting materials, the organic dye molecules provide more variable and easier mixing strategies to engineer the PL of gain for multi-color laser. Organic dye molecules can perform as gain media for plasmonic nanolasers.<sup>13, 29</sup> Lattices of coupled plasmonic

nanoparticles (NPs) can produce surface lattice resonances (SLRs) for cavity mode designs with subwavelength confinement of electric fields and control over band-edge states to achieve multimode cavities.<sup>12-13, 29, 53-55</sup> Through tuning the refractive index of the environment,<sup>13</sup> engineering lattice geometry<sup>28, 54, 12</sup> and NP unit cell,<sup>55</sup> we can engineer the wavelegnth of the SLRs to realize plasmonic nanolasers at different wavelengths. Furthermore, the plasmonic lasing emission process is contributed predominately by the excitons located in the distinct hotspots of the plasmonic NPs at SLRs<sup>54, 56</sup>, which offer a platform for the cavity designs of white color laser. That is, by designing the cavity modes of SLR to separate the hotspot regions for each SLR, we can suppress the mode competitions to realize blue, green and red color lasers at the same time. In conjunction with gain engineering and cavity mode designs, the plasmonic lasing intensities can be easily tuned by varying the concentrations of organic dye gain media and pump powers.<sup>57-59</sup>

Here we show that multiple SLRs at the  $\Gamma$  points of square lattice can provide optical feedbacks for plasmonic multicolor lasing. By mixing two different dye solutions to have spectral overlap with the SLRs, we achieved blue and red lasers simultaneously at the  $\Gamma$  point. The relative intensities of blue and red color lasers are tuned by changing the concentrations of mixed dye solutions. Moreover, we stacked two square lattices with different periodicities to enable three SLRs corresponding to blue, green and red color wavelength regime at the  $\Gamma$  point. By mixing three dye solutions and tuning the each dye concentrations, we successfully achieved blue, green and red color lasers at the  $\Gamma$  point.

### 3.2 Individual Lasing Emission from Plasmonic Square Arrays

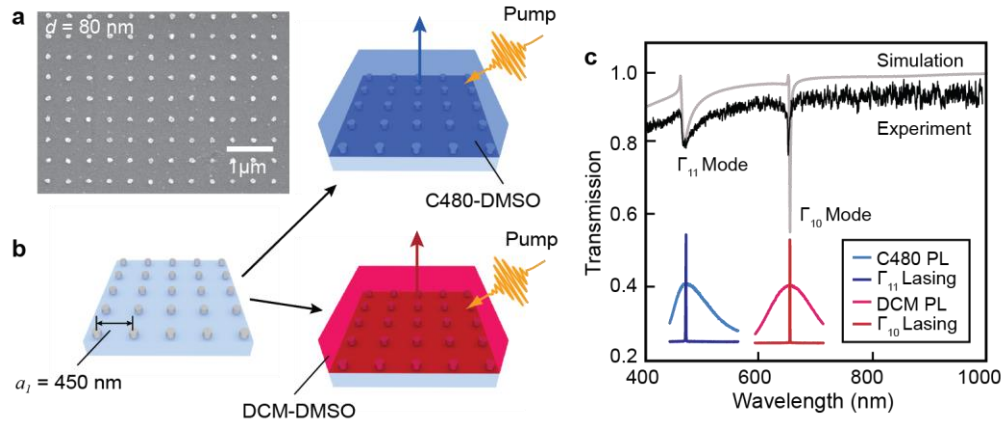


**Figure 3.1. Fano-type  $\Gamma_{11}$  and  $\Gamma_{10}$  Resonances in Plasmonic Square Lattice.** (a) SEM image of fabricated square lattice ( $a_0 = 450$  nm) of Al NPs with 60 nm diameter and 50 nm height. (b) Scheme of realizing red and blue lasing emission with Al NP array under 400 nm wavelength femtosecond pump. (c) Calculated and measured transmission spectra of lattice in (a) for x-polarized plane waves at the  $\Gamma$  point showing strong SRL  $\Gamma_{11}$  and  $\Gamma_{10}$ . Lasing supported by  $\Gamma_{11}$  and  $\Gamma_{10}$  modes was achieved by incorporating spectrally overlapped dye solutions.

**Figures 3.1a** shows the SEM image of fabricated Al NPs with uniform NP size and shape. Solvent-assisted nanoscale embossing (SANE<sup>60</sup>) and PEEL processes<sup>61-62</sup> were used to fabricate Al NP arrays in square lattice (spacing  $a_0 = 450$  nm, diameter  $d = 80$  nm, height  $h = 50$  nm) on silica over  $\text{cm}^2$  areas. **Figure 3.1b** describes the scheme of realizing blue and red color lasing individually. Basically, with the same plasmonic Al NP lattice and 400 nm wavelength pulsed laser pump, we can incorporate different dye solutions, which has spectral overlap with each SLR, to achieve blue and red color laser separately. **Figure 3.1c** suggests the good agreement between simulated and experimental measured transmission spectra of Al NP array in square lattice (Methods). Under transverse magnetic (TM) polarized plane wave excitation, the fabricated Al NP

arrays incorporated with dimethyl sulfoxide solution (DMSO) (refractive index: 1.44) support two high-quality SLRs at the  $\Gamma$  point. The localized surface plasmon resonances (LSPs) of Al NPs couple to (1,1) diffraction mode of square lattice, resulting the  $\Gamma_{11}$  mode at 472 nm. On the other hand, the SLR at 655 nm ( $\Gamma_{10}$  mode) comes from the coupling between the LSPs of Al NPs and (1,0) diffraction mode. 20mM C480-DMSO solutions shows PL centered at 465 nm wavelength, which enables the spectral overlap with  $\Gamma_{11}$  mode. Under 400 nm wavelength pulsed laser pump,  $\Gamma_{11}$  lasing at 468 nm was realized by putting 20mM C480-DMSO solution onto Al NP array. Similarly, incorporating 5mM DCM-DMSO dye solutions (PL centered at 645 nm) onto Al NP

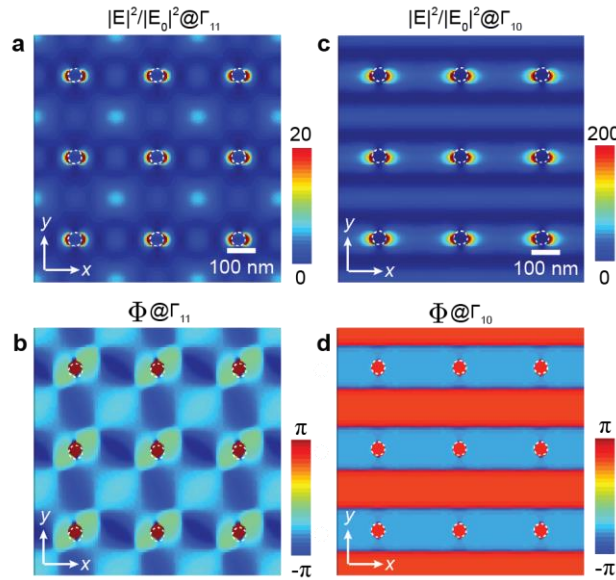


**Figure 3.2. Near-field distributions at  $\Gamma_{11}$  and  $\Gamma_{10}$  Resonance.** (a) Calculated electric field magnitude within the XY plane of square lattice excited at  $\Gamma_{11}$  mode showing symmetric spatial distributions characteristic. (b) Calculated phase mapping at  $\Gamma_{11}$  mode. (c) Calculated electric field magnitude within the XY plane of square lattice excited at  $\Gamma_{10}$  mode showing dipolar coupling. (d) Calculated phase mapping at  $\Gamma_{10}$  mode.

array and pumping with 400 nm wavelength femtosecond pulsed laser, we achieved  $\Gamma_{10}$  lasing at 654 nm (Figure 3.1c).

To identify the near-field coupling of  $\Gamma_{11}$  and  $\Gamma_{10}$  modes, we used finite-difference time-domain (FDTD) simulation to investigate the near-field electric distributions and phase mapping of  $\Gamma_{11}$  and  $\Gamma_{10}$  modes. Under TM excitation of incident plane-wave light, the  $\Gamma_{11}$  mode shows a symmetric charge distribution with dipoles orientated along the polarization direction of incident light (**Figure 3.2a**). The phase fronts of the standing-wave patterns at the  $\Gamma_{11}$  mode are along the direction of (1,1) mode, suggesting the SLR at  $\Gamma_{11}$  mode is from in-plane dipole coupled with (1,1) diffraction mode (**Figure 3.2b**). Furthermore, the near-field electric distributions and phase mapping of  $\Gamma_{10}$  mode shows that the  $\Gamma_{10}$  mode is from in-plane dipole coupled with (1,0) diffraction

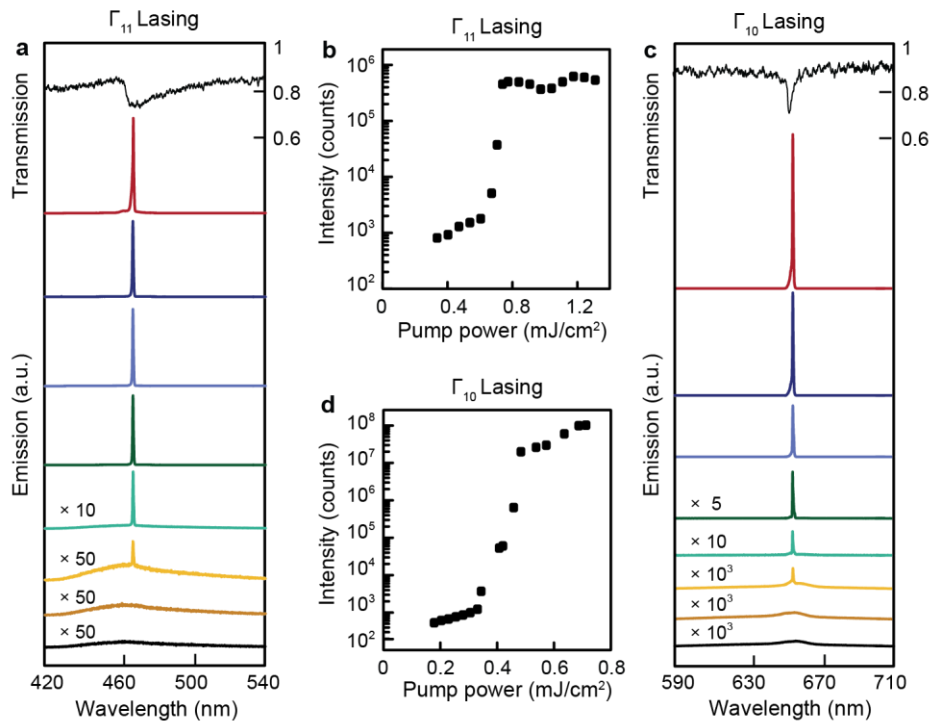


**Figure 3.3. Lasing Characterizations Supported by  $\Gamma_{11}$  and  $\Gamma_{10}$  Resonance.** (a)  $\Gamma_{11}$  lasing output profiles. (b) Light-light curve of  $\Gamma_{11}$  lasing showing threshold value of 0.61 mJ/cm<sup>2</sup>. (c)  $\Gamma_{10}$  lasing out-put profiles with increasing pump powers. (d) Light-light curve of  $\Gamma_{10}$  lasing showing threshold value of 0.33 mJ/cm<sup>2</sup>

mode (**Figure 3.2c and 3.2d**), which is similar to other in-plane dipole SLRs reported before.<sup>17,</sup>

<sup>56</sup> First of all, we investigated the individual lasing emission supported by  $\Gamma_{11}$  and  $\Gamma_{10}$  mode. **Figure 3.3a** shows the  $\Gamma_{11}$  lasing emission output profiles supported by  $\Gamma_{11}$  mode. We put a droplet of 20mM C480-DMSO dye solution onto the Al NP array and capped it with a cover glass. Under 400 nm femtosecond pulsed pump, we observed the lasing emitted at 468nm. The wavelength of  $\Gamma_{11}$  lasing (468 nm) determines its blue color. Angle-resolved emission profiles shows that the  $\Gamma_{11}$  lasing emitted at surface normal direction (**Figure 3.4a**). The light-light curve of  $\Gamma_{11}$  lasing suggests the threshold value of  $\Gamma_{11}$  lasing is around 0.61 mJ/cm<sup>2</sup> (**Figure 3.3b**). When putting a droplet of 5mM DCM-DMSO solutions onto Al NP array and covered with glass slide, we can excite  $\Gamma_{10}$  mode to achieve red color  $\Gamma_{10}$  lasing at 654 nm with lasing threshold around 0.33 mJ/cm<sup>2</sup> (**Figure 3.3c and 3.3d**). The angle-resolved emission also indicate the surface normal direction

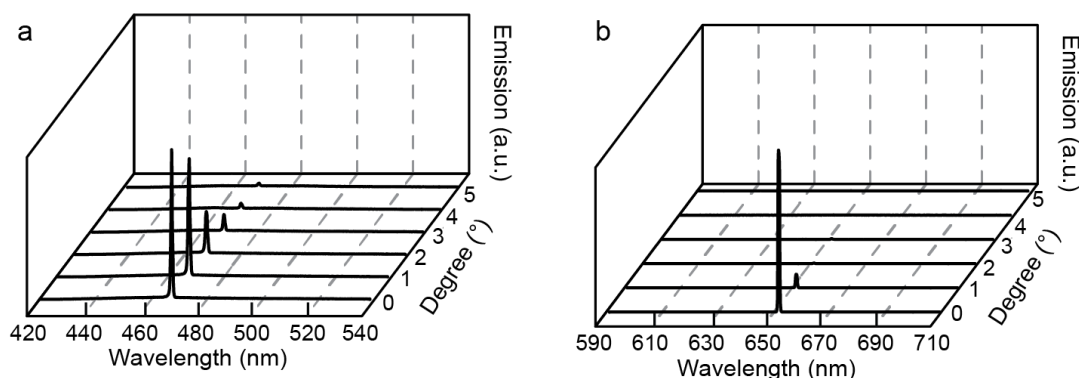


**Figure 3.4. Angle-resolved emission of (a)  $\Gamma_{11}$  and (b)  $\Gamma_{10}$  lasing shows the directionality of lasing.**

emission of  $\Gamma_{10}$  lasing (**Figure 3.4b**). Compared with  $\Gamma_{11}$  lasing, the  $\Gamma_{10}$  lasing shows stronger intensity and lower threshold could be related to the different dye efficiencies, higher quality factor (Figure 3.1c) and stronger near-field electric intensities of  $\Gamma_{10}$  mode (Figure 3.2a and 3.2c).

### 3.3 Multi-color Lasing Emission in Square Arrays

To obtain blue color  $\Gamma_{11}$  lasing and red color  $\Gamma_{10}$  lasing simultaneously, we mixed the C460-DMSO dye solutions with DCM-DMSO solutions to have a mixed dye which has spectrally overlap with both  $\Gamma_{11}$  and  $\Gamma_{10}$  modes. Considering mixing two dye solutions together will decrease

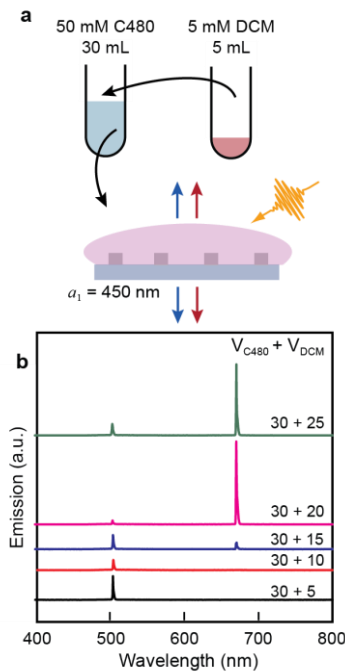


**Figure 3.5.  $\Gamma_{11}$  and  $\Gamma_{10}$  Lasing Emissions from Plasmonic Square Lattice.** (a) Scheme of mixing two dye solutions and achieve  $\Gamma_{11}$  and  $\Gamma_{10}$  lasers simultaneously. (b) Measured lasing spectra by incorporating mixed dye solutions with different volume ratios.

the concentrations of each individual dye solution, we started with 50mM C480-DMSO dye solution with 5mM DCM-DMSO dye solution. Initially, we used 30mL 50mM C480-DMSO dye solutions and we added 5mL 20mM DCM-DMSO dye solution into the C480-DMSO dye solution every time (**Figure 3.5a**). The PL of mixed dye shows two peaks at 464 nm and 645 nm, which is similar to the PL peak of individual dye solutions (**Figure 3.6**). A glass pipette was used to obtain one droplet of mixed dye solutions (less than 5 $\mu$ L), then we put it on the top of Al NP array and

covered with a glass slide. Under 400 nm wavelength pulsed laser pump, we used charge-coupled device (CCD) camera to detect the output lasing emissions at surface normal with a constant pump

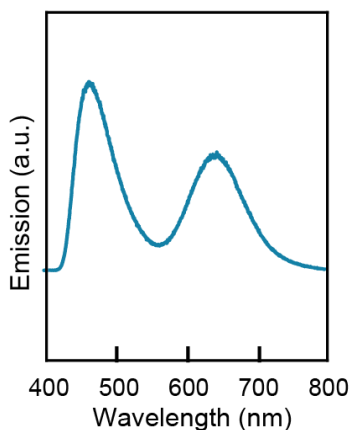


**Figure 3.6: PL of mixed dye shows two peaks at 464 nm and 645 nm.**

power around  $1.34 \text{ mJ/cm}^2$ . **Figure 3.5b** shows the lasing emission spectra under different mixed volume of DCM-DMSO dye solution. With less than 10mL DCM-DMSO dye solution mixed, only the  $\Gamma_{11}$  lasing signal was observed because the concentration of DCM in mixed dye solution is not high enough to support  $\Gamma_{11}$  lasing at  $1.34 \text{ mJ/cm}^2$ .  $\Gamma_{10}$  lasing appeared when we mixed 15mL DCM-DMSO with 30mL 50mM C480-DMSO dye solution. By increasing the mixing volume of DCM-DMSO dye solution, the concentration of DCM in mixed dye solution increases and concentration of C480 in mixed dye solution decreases. We observed stronger  $\Gamma_{10}$  lasing signal and weaker  $\Gamma_{11}$  lasing emission. Our results suggest one platform to manipulate the lasing emission output intensities by tuning the concentrations of individual dye molecules in mixed dye solution.

### 3.4 Blue, Green and Red Color Lasing by Stacking Two Square Lattices

To achieve plasmonic monolithic white laser, we need to introduce another  $\Gamma$ -point SLR in green color wavelength regime. For Al NPs ( $d = 60$  nm,  $h = 50$  nm) in 350 nm periodicity square lattice surrounded by DMSO solvents, it can support a  $\Gamma$ -point SLR at 509 nm, which is in the green color wavelength range (**Figure 3.7**). Under TM excitation of incident light, the  $\Gamma$ -point

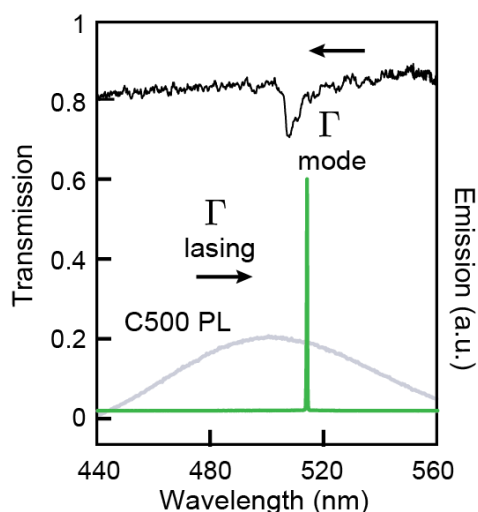


**Figure 3.7. The  $\Gamma$  Mode from Al NPs in 350 nm periodicity square lattice supports lasing at 514 nm when incorporating with 20mM C500 Dye-DMSO solution onto NP array.**

SLR is formed because the LSPs of Al NPs couple with (1,0) diffraction mode. By incorporating 20mM C500-DMSO dye solution (PL centered at 505 nm wavelength) on to the 350 nm periodicity Al NP array, a green color lasing signal at 514 nm was observed at surface normal direction (**Figure 3.8**). Then we stacked Al NP array with 350 nm periodicity square lattice with 450 nm periodicity square lattice together. With DMSO put between the two lattices, the whole device shows three SLRs (472 nm, 509 nm and 655 nm) at  $\Gamma$  point (**Figure 3.9a**). The three SLRs are not influenced by the translational angle between the two square lattices due to the

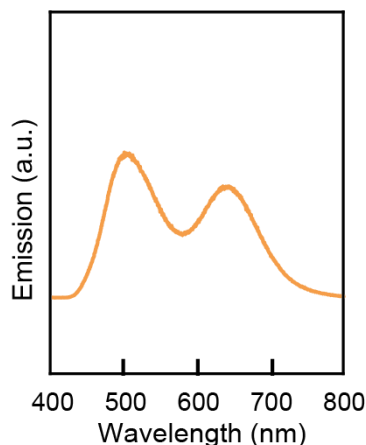


**Figure 3.8.** The three dye mixed solution shows PL emission from 440 nm to 740 nm wavelength range with two PL peaks at 501 nm and 642 nm.

micro-scale distance between the two lattices (Figure 3.9a). Previously we found that with  $V_{C480} : V_{DCM} = 30 : 15$ , we can have blue and red color lasers with comparable intensities (Figure 3b). Therefore, we started with 300 $\mu$ L mixed dye solution with this ration (corresponding to 200 $\mu$ L 50mM C480-DMSO and 100 $\mu$ L 5mM DCM-DMSO) and add 100 $\mu$ L 50mM C500-DMSO solution as shown in the scheme of **Figure 3.9b**. The three dye mixed solution shows PL emission from 440 nm to 740 nm wavelength range with two PL peaks at 501 nm and 642 nm (**Figure 3.10**). The blue PL peak comes from the combinations of C480 PL and C500 PL. Under 400 nm wavelength pulsed laser, we measured the lasing output profiles at a constant pump power of 1.34 mJ/cm<sup>2</sup> (**Figure 3.9c**). To avoid the effects of pump polarizations on different SLRs, we aligned the two stacking lattices with translational angle equals to 0° during measurement. Under 400 nm wavelength pulsed laser with a constant pump power of 1.34 mJ/cm<sup>2</sup>, we observed three lasing emissions at 464 nm, 512 nm and 654 nm wavelengths, which are supported by the three SLRs at the  $\Gamma$  point. The emission at 654 nm is stronger than the

emission at 468 nm possibly because the PL of C480 dye has a minor overlap with the absorption of C500 dye, causing less excitons to support lasing at 468 nm (**Figure 3.10**).

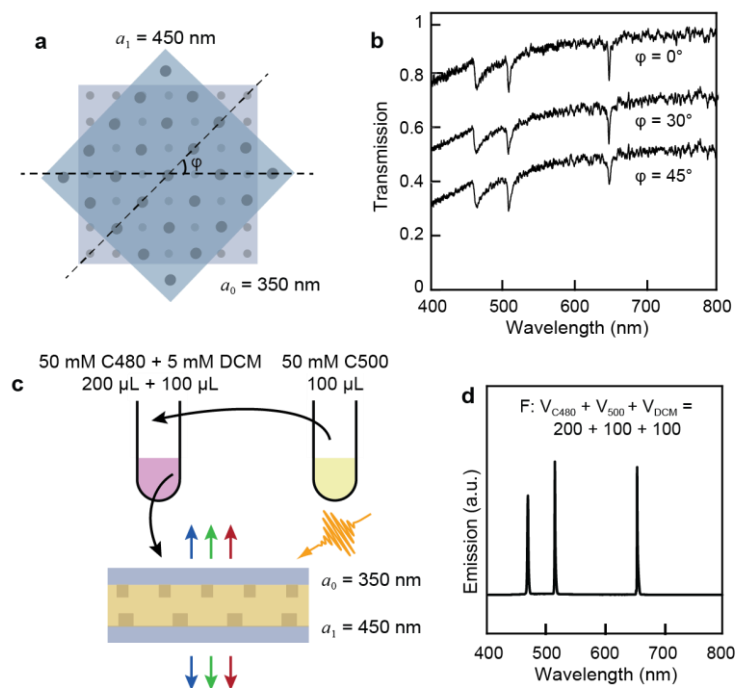


**Figure 3.9. Multi-color Lasing Emission from Stacking Two Plasmonic Square Lattice.** (a) Scheme of stacking two square lattices with different rotational angles ( $\varphi$ ). (b) Transmission spectra from stacking two plasmonic square lattice with different  $\varphi$  values. (c) Scheme of measuring lasing emissions and device design. (d) Measured laser emission output with the three mixed dye solutions.

Moreover, the absorption of DCM dye overlaps with the PL of C500 dye, extra C500 dye molecules in the mixed solution can provide more excitons to support lasing at 654 nm (Figure S6). A lasing signal emitted at 514 nm, which is supported by the  $\Gamma_{10}$  mode from 350 nm periodicity square lattice, was observed when we added 40 $\mu$ L 50mM C500 dye solution to the mixed dye solutions. Stronger lasing emission at 514 nm and weaker emission at 468 nm were

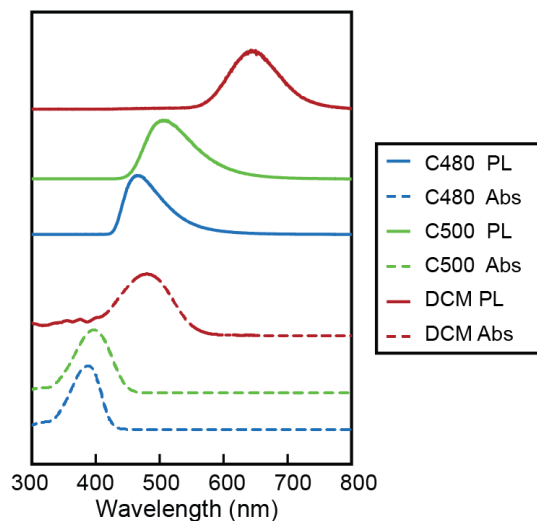


**Figure 3.10. Individual PL and absorption spectra of three dye solutions.**

detected with more C500 dye solution mixed (Figure 3.9c). Finally, the lasing emission signal at 468 nm disappeared with 120 $\mu$ L C500 dye solution added to the mixed dye solution. This may be because the absorption of C500 dye has overlap with the PL of C480 dye (Figure S6). Too much C500 dye molecules in the mixed dye solution leads to intense energy transfer from C480 dye molecules to C500 dye molecules, leading to the insufficient gain from C480 dye to support lasing at 468 nm.

### 3.5 Plasmonic Lasing Emitted from Off-normal Directions

Few studies reported engineering of SLRs at the high-symmetry points to achieve multicolor lasing over a wide range of angles on a single device.<sup>17, 51, 63</sup> Lasing from plasmonic superlattice emitted at different wavelengths simultaneously, but is limited in a small wavelength range (less than 20 nm). QDs shell lasing from plasmonic square arrays can emit over wide range angles but can only emit at one color at a time. Here we show that the SLRs at the high-symmetry points can support plasmonic nanolasers emitted in directions with respect to the off-normal SLRs at high-symmetry points. We realized green, yellow and orange color lasers at the same time on a single device over a wide range angles by incorporating one dye solutions overlapped with SLRs.

**Figure 3.11** shows the off-normal lasing emissions from Al NPs in square lattice with 450 nm periodicity. **Figure 3.11a** depicts the dispersion diagrams of Al NPs in square lattice. Along  $\Gamma$ -X symmetry, exciting the lattice under TM polarization of incident light, we have X and  $\Delta_2$  ( $\Delta$  point in the second BZ) high-symmetry points. And under TE excitation of incident light, there is a  $\Delta$  high-symmetry point along  $\Gamma$ -X direction. Moreover, with TE polarization of incident light exciting the lattice along  $\Gamma$ -M direction, we observed M/3 high-symmetry point. **Figure 3.11b** shows the scheme of experimental setup for measuring lasing emission from off-normal high-symmetry points. Under 400 nm wavelength femtosecond pulsed laser with 100 Hz frequency,

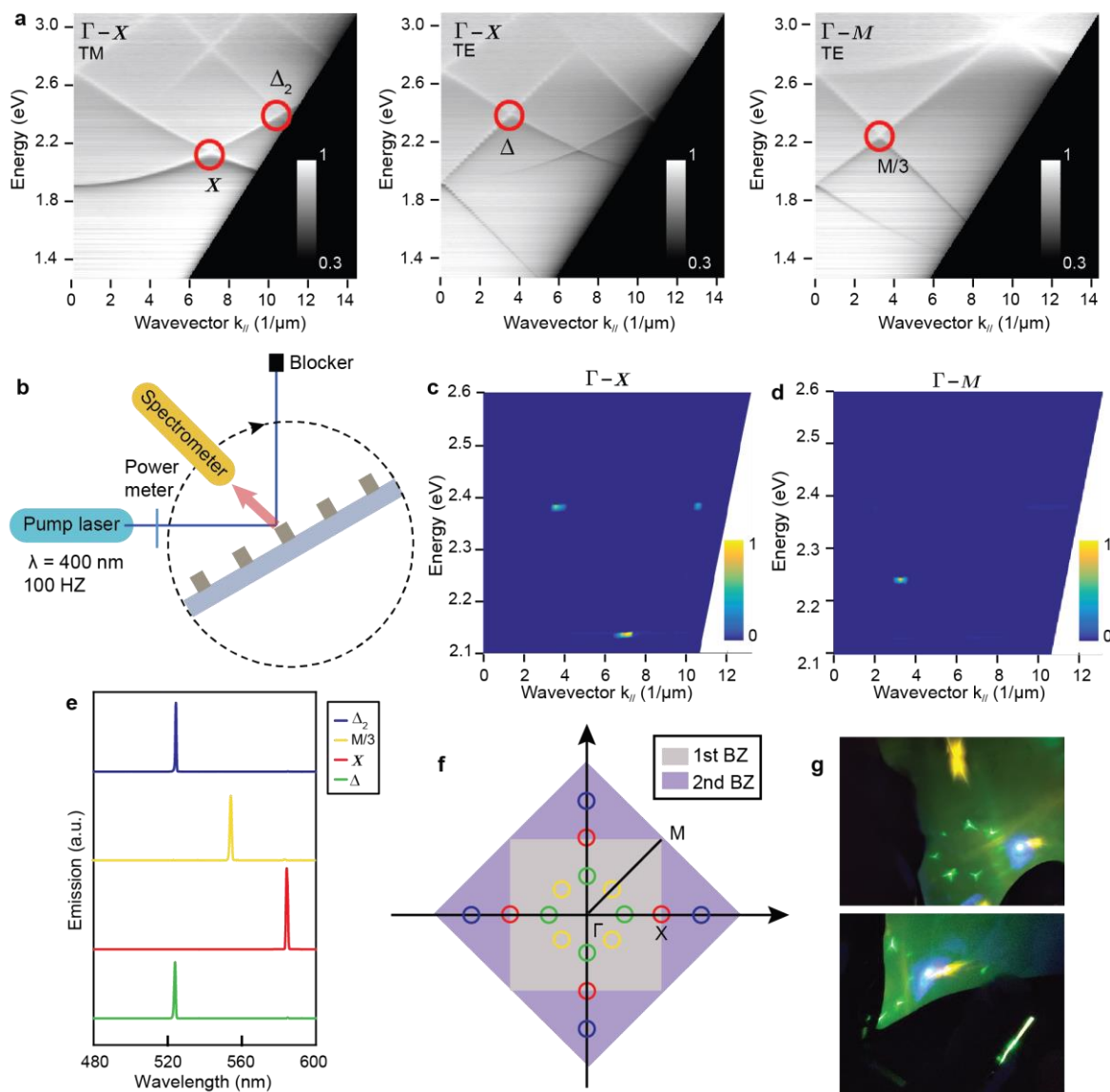


**Figure 3.11. Multi-color Lasing Emission from Plasmonic Square Lattice.** (a) Measured dispersion diagram of Al NPs in square lattice under different polarization angles of incident light at different geometries. (b) Scheme of measuring lasing emission from off-normal high-symmetry directions. Measured angle-resolved emission of Al NPs in square lattice from (c)  $\Gamma-X$  and (d)  $\Gamma-M$  directions. Measured lasing spectra by incorporating mixed dye solutions with different volume ratios. (e) Representative lasing spectra from off-normal high-symmetry points. (f) The spatial distributions of lasers corresponding to the Brillouin zones (BZ). (g) Photos of laser beams showing similar spatial distributions of lasers in (f).

we put a droplet of 20mM C481-DMSO dye solution on top of the NPs and capped with a cover slide. The C481-DMSO dye solution has central wavelength at 515 nm with PL wavelength ranging from 440 nm to 620 nm under 400 nm wavelength pump. The angle of incident pump source was set to be around  $30^\circ$  to avoid the reflected pump spot overlapped with lasing emissions. And the reflected pump spot was blocked to prevent the damage from high pump power to the detector. We measured the lasing emission spectra by rotating the spectrometer every  $1^\circ$  manually to obtain the angle-resolved emission map. **Figure 3.11c and 3.11d** show the experimental angle-resolved emission along different symmetry directions. It indicates the consistence between bandstructure dispersion diagrams with lasing emission map. Along  $\Gamma$ -X direction, we observed lasing emissions from X,  $\Delta_2$  and  $\Delta$  points. Along  $\Gamma$ -M direction, we observed lasing emission from

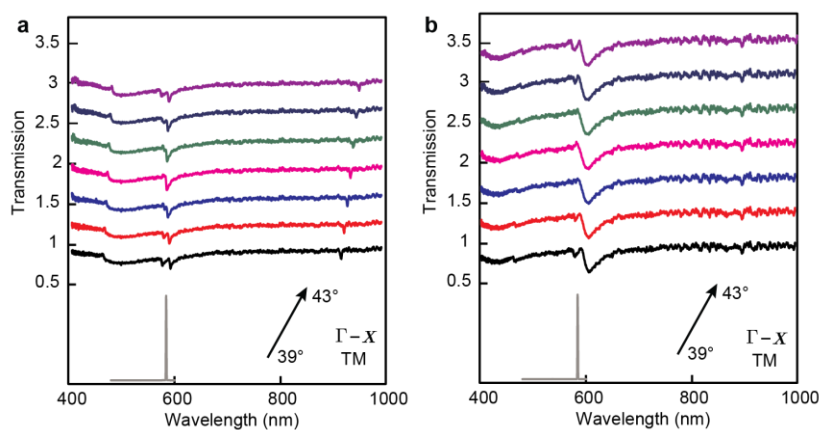


**Figure 3.12. The spectral comparison between X-point lasing emission and transmission spectra near X-point under (a) TM and (b) TE excitations of incident light.**

M/3 point. Figure 3.11e suggests the representative lasing emission spectra from different high-symmetry points. Basically, the  $\Delta$ -point lasing was at 520 nm wavelength from  $17^\circ$ , X-point lasing was at 581 nm wavelength from  $41^\circ$ , M/3-point lasing was at 552 nm wavelength from  $17^\circ$ ,  $\Delta_2$ -

point has the same energy to  $\Delta$ -point but different at  $k_{//}$  wavevectors,  $\Delta_2$ -point lasing was at 520 nm wavelength from  $61^\circ$ . Because the square lattice has 4-fold symmetry and all the high-symmetry points come from the Brillouin zone, we are able to draw the scheme of the spatial distributions of lasers from off-normal high-symmetry points (**Figure 3.11g**). And the experimental observations of emitted laser beams show similar distribution patterns with theory (**Figure 3.11f**). Interestingly, if we compare the X-point lasing emission wavelength from off-normal directions with the transmission spectra at different angles, we will see the off-normal emission was supported by the resonance at the sidebands near the high-symmetry points (**Figure 3.12**). Similar phenomena were observed for other off-normal lasing emissions as shown in **Figure 3.13**. The angle-resolved measurement didn't show two beams near each high-symmetry point is because the detection angle of spectrometer is  $3^\circ$ , which cannot resolve the sideband effects. This is because the sidebands have stronger near-field intensities than the center part.

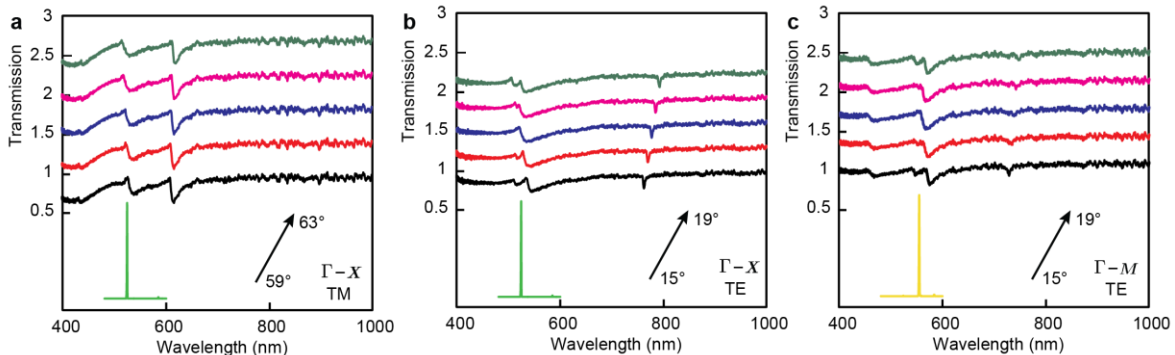


**Figure 3.13. The spectral comparison between off-normal lasing emission and transmission spectra near the high-symmetry points. (a)  $\Delta_2$ -point lasing, (b)  $\Delta$ -point lasing, (c) M-point lasing.**

### 3.6 Summary and Outlook

In conclusion, we realized plasmonic monolithic white color laser by engineering the dye gain media and designing the device supporting plasmonic lasing. We demonstrated the both  $\Gamma_{11}$  and  $\Gamma_{10}$  mode in square lattice can support plasmonic lasing simultaneously. We achieved blue, green and red color plasmonic lasers on a single device. Engineering the concentrations of each dye gain media supporting corresponding SLR lasing, we are able to control the relative intensities of output lasing emissions, which presents a wide tunability of lasing output color. We expect our results can benefit for nanophotonics and nanotechnology communities. We believe that our demonstrations of tuning the color of plasmonic nanolasers can provide a powerful design strategy for applications such as full-color display, multi-color fluorescence sensing and dynamical color control device.

## 3.7 Methods

### 3.7.1 Fabrication of Ag NP arrays

Al NP lattices on fused silica were fabricated with a soft nanofabrication process. First, we generated periodic photoresist posts on Si wafers by solvent-assisted nanoscale embossing (SANE<sup>60</sup>). The patterns were then transferred into free-standing Au nanohole films after Cr deposition, removal of photoresist posts, etching through the Si nanoholes and lift-off of the Au film. Finally, we created Al NP lattices by E-beam deposition through the hole-lattice mask on fused silica and then removal of the mask.

### 3.7.2 FDTD simulations

FDTD calculations with commercial software (FDTD solution, Lumerical Inc., Vancouver, Canada) were used to simulate the linear optical properties from Al NP lattices. Periodic boundary conditions were set for both  $x$  and  $y$  direction. PML boundary condition was used for  $z$  direction. The optical constants of Al were taken from Palik constant<sup>64</sup>. A uniform mesh size of 2 nm ( $x$ ,  $y$  and  $z$ ) was used to calculate the near-field electric and phase mapping within the metal NPs.

### 3.7.3 Lasing measurements

The plasmonic laser was optically pumped using 35 fs, 400-nm laser pulses with a repetition rate of 100 Hz, beam diameter of  $\sim 600$   $\mu\text{m}$ , incident excitation angle  $\sim 45^\circ$ . Lasing signals were collected normal to the sample surface and measured by a charge-coupled device (CCD) spectrometer. 435 nm long pass filter was used to avoid the pump beam entering and damage CCD camera. A manually controlled translational stage was used to measure the angle-resolved emission with every  $1^\circ$ .

## Chapter 4. Hierarchical Hybridization in Plasmonic Honeycomb Lattices

### Abstract

This chapter reports hierarchical hybridization as a mode-mixing scheme to account for the unique optical properties of non-Bravais lattices of plasmonic nanoparticles. The formation of surface lattice resonances mediated by localized surface plasmons of different multipolar orders, *e.g.* dipole and quadrupole, can result in asymmetric electric near-field distributions surrounding the NPs. This asymmetry is because of LSP hybridization at the individual NP level from LSPs of different multipole order and at the unit-cell level (NP dimer) from LSPs of the same multipole order. Fabricated honeycomb lattices of silver NPs exhibit ultra-sharp SLRs at the  $\Gamma$  point that can also facilitate nanolasing. Modeling of the stimulated emission process revealed that the multipolar component of the lattice plasmon mode was responsible for feedback for lasing. By leveraging multipolar LSP responses from aluminum NPs lattices, we achieved two distinct  $\Gamma$  point band-edge modes from a single honeycomb lattice. These relatively unexplored degrees of freedom can decrease both ohmic and radiative losses in nanoscale systems and enable SLRs to build unanticipated connections among photonics and nanochemistry.

### Related references

**Li, R.;** Bourgeois, M. R.; Cherqui, C.; Guan, J.; Wang, D.; Hu, J.; Schaller, R. D.; Schatz, G. C.; Odom, T. W., Hierarchical Hybridization in Plasmonic Honeycomb Lattices. *Nano letters* **2019**, *19* (9), 6435-6441.

## 4.1 Introduction

Two-dimensional (2D) materials with honeycomb lattice symmetry exhibit unusual conductive and optical properties because of degeneracies at the high-symmetry points in the electronic band structure.<sup>65-68</sup> In solids, band structure emerges from the interplay between global lattice symmetry and interactions between atomic wavefunctions at each site. In 2D lattices of plasmonic nanoparticles (NPs), an analogous photonic band structure can result, where atomic wavefunctions are replaced by surface-bound electron oscillations known as localized surface plasmons (LSPs) or LSP wavefunctions. By exploiting the intrinsic size-and-composition tunability of the LSP wavefunctions, NP units offer a programmable basis set that does not exist in electronic systems.<sup>53, 69</sup> For example, as the distance between NPs becomes commensurate with an integer multiple of the wavelength of incident light, collective lattice modes emerge that can be rationally tuned based on the diffractive character of the 2D array as well as the induced charge distribution of LSPs.<sup>70-73</sup> These lattice plasmons, also called surface lattice resonances (SLRs), are characterized by an energy dispersion relation  $E(\mathbf{k}_{\parallel})$ , where  $\mathbf{k}_{\parallel}$  is the in-plane wave vector.<sup>6, 74</sup>

The photonic band structure of SLRs can be constructed directly from transmission spectra and indirectly from the back-focal plane of a microscope or spectroscopic ellipsometry.<sup>6, 75-81</sup> Early work reported that there were no major differences among the linear optical properties of square, rectangular, hexagonal, and honeycomb lattices at the  $\Gamma$  point ( $|\mathbf{k}_{\parallel}| = 0$ ) based on dipole (D) interactions between units.<sup>82</sup> An analysis of the mode symmetries and far-field polarization properties of the K-point SLRs supported by a plasmonic honeycomb lattice were also recently reported.<sup>21</sup> Work that captured SLR dispersion characteristics showed clear differences due to lattice symmetry, but since the data was analyzed only according to the free-photon dispersion

relation, effects of scattering from NPs on the resulting band structure were not considered.<sup>77</sup> The relationship between lattice symmetry and contributions of higher-order LSPs to SLRs has just started to receive attention. Quadrupolar (Q) coupling in plasmonic NP lattices show characteristics from out-of-plane Q-Q interactions that are similar to those from D-D coupling.<sup>83-</sup><sup>85</sup> Although SLRs from in-plane Q-Q coupling have been observed in *finite* square lattices,<sup>85</sup> these modes are optically dark in the infinite lattice limit. Also, the focus on SLRs in Bravais lattices has been on modes mediated by LSPs of the same multipolar order because SLR modes of mixed D-Q character are not accessible at the  $\Gamma$  point in systems of such symmetries.<sup>83</sup> In the case of non-Bravais lattices, where D-Q coupling is allowed at the  $\Gamma$  point, only far-field observables have been reported, with near-field signatures missing.<sup>12, 85</sup>

Recent interest in the band structure of SLRs has been motivated in part by the emergence of topological photonics in dielectric NP arrays. The low losses associated with dielectric NPs allow for defect-tolerant unidirectional propagating edge states,<sup>86-87</sup> and topological states in plasmonic systems have been considered.<sup>84, 88-89</sup> However, topological effects are challenging to realize in metal systems because of radiative and ohmic losses. SLRs provide a potential strategy to explore topology-based phenomena because they can mitigate losses associated with plasmonic NPs.<sup>90</sup> By exploring non-Bravais lattice symmetries and complex wavefunction hybridization at the unit-cell level, we can test how lattice symmetry and LSP wavefunction bases can be applied to plasmonic topological effects.<sup>91</sup>

Here we show that honeycomb plasmonic lattices can produce SLRs from the hybridization of same-order LSPs between lattice sites and hybridization of different-order LSPs at the same lattice site. This mode-mixing scheme—hierarchical hybridization—is a result of the non-Bravais nature

of the honeycomb lattice combined with the available LSP wavefunction basis of plasmonic NPs. Hybrid SLRs exhibit asymmetric surface-charge distributions on the NP surfaces that dominate the near-field, and whose effects can be visualized by plasmonic lasing with silver NP lattices. We extended and leveraged the LSP wavefunction basis to create a single lattice that could support two distinct band-edge SLRs that were spectrally separated by ca. 300 nm in aluminum NP lattices. This work highlights a distinct feature of plasmonic NP lattices that enables an unexpected class of hybridization not possible in other nanophotonics systems.

## 4.2 Hybridized $\Gamma_1$ Mode in Plasmonic Honeycomb Lattice

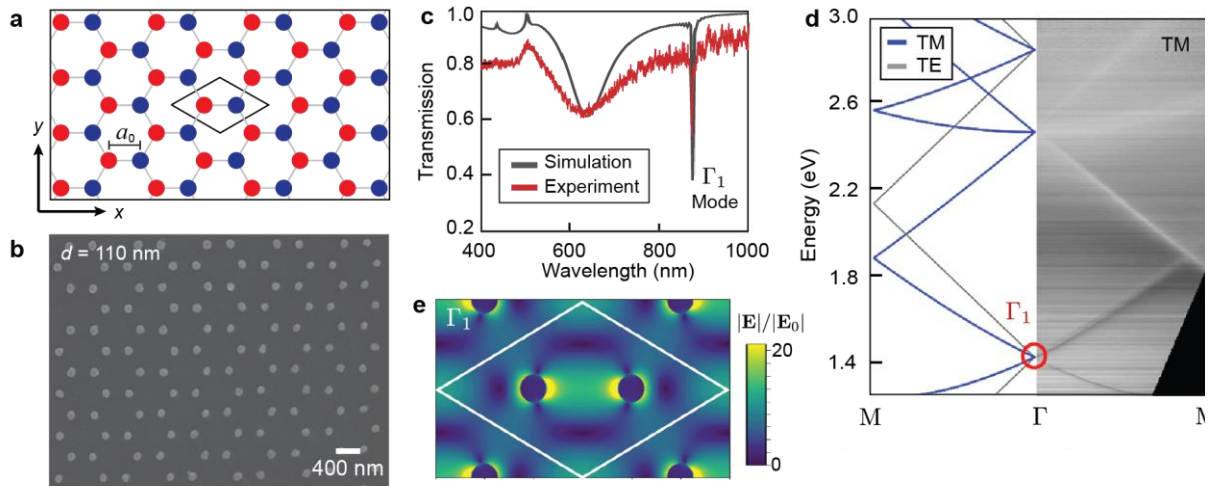


**Figure 4.1. Hybridized  $\Gamma_1$  Mode in Plasmonic Honeycomb Lattice.** (a) Scheme of a honeycomb lattice with two NPs per unit cell (outlined). Red and blue sites belong to hexagonal sublattices  $L_1$  and  $L_2$ , respectively. (b) SEM image of fabricated honeycomb lattice ( $a_0 = 400$  nm) of Ag NPs with  $d = 110$  nm and  $h = 50$  nm. (c) Calculated and measured transmission spectra of lattice in (b) for  $x$ -polarized plane waves at the  $\Gamma$  point showing strong SLR  $\Gamma_1$ . (d) Calculated (left) and measured (right) dispersion diagram (angle-dependent transmission of TM polarized plane wave) for the lattice in (b) along the  $\Gamma - M$  path through the Brillouin zone. (e) Calculated electric field magnitude within the  $xy$  plane of honeycomb unit cell excited at  $\lambda_{\Gamma_1}$  showing asymmetric spatial distributions characteristic of multipolar LSP superposition.

**Figure 4.1a** indicates how the honeycomb lattice can be described as a hexagonal lattice with a two-unit basis or a superposition of two identical but non-equivalent hexagonal sublattices  $L_1$  (red) and  $L_2$  (blue).  $L_1$  and  $L_2$  are related by an inversion operation and are characterized by two length scales: (1) the magnitude of the basis vectors of each hexagonal sublattice  $a$ ; and (2) the distance between adjacent NPs in the honeycomb lattice  $a_0 = a/\sqrt{3}$ . **Figure 4.1b** shows a

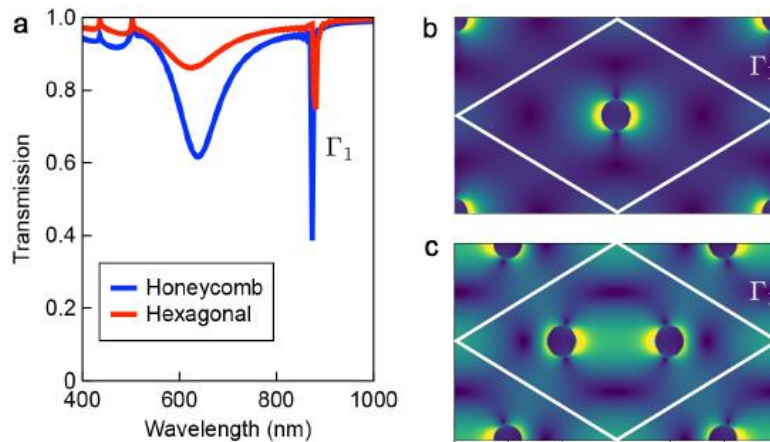


**Figure 4.2.  $\Gamma_1$  SLR in hexagonal lattice.** (a)  $\Gamma$  point x-polarized transmission spectra for honeycomb and hexagonal lattices calculated using FDTD. (b) Calculated electric field magnitude, normalized to that of the incident field, of  $\Gamma_1$  SLR within the XY plane of hexagonal lattice unit cell. (c) Figure 1e of the main text reproduced for comparison with panel b).

honeycomb lattice ( $a_0 = 400$  nm) made of Ag NPs ( $d = 110$  nm diameter) fabricated by soft nanolithography.<sup>23</sup> The NP dimensions were chosen to optimize the SLR mode at the  $\Gamma$  point (873 nm or 1.42 eV) (**Figure 4.1c**) to have a quality factor  $\approx 170$  and a FWHM  $\approx 5$  nm. The broad feature near 625 nm (2.0 eV) is the single-NP LSP response. The transmission spectrum calculated using the finite-difference time-domain (FDTD) method<sup>12</sup> using periodic boundary conditions is accurate when fabricated samples are patterned over large enough areas ( $\sim \text{cm}^2$ ) to be considered infinite.<sup>17, 85</sup>

The dispersion diagram of the fabricated Ag NP honeycomb lattice was mapped along the  $\Gamma$ -M direction through the Brillouin zone by measuring transmission spectra of  $x$ -polarized TM plane waves (polarization vector parallel to the plane of incidence) as a function of incident angle (**Figure 4.1d**, right). The experimental dispersion diagram is similar to the calculated TM-polarized photonic cavity dispersion relation<sup>77</sup> except near the high-symmetry  $\Gamma_1$  (1.42 eV, 873 nm) and M (1.87 eV, 664 nm) points, where deviations emerge from the formation of band-edge states as a result of NP scattering (**Figure 4.1d**, left). The narrow spectral feature in the normal-incident transmission spectrum (Figure 1c) can be assigned as a  $\Gamma_1$  point SLR with associated electric near-field distribution (**Figure 4.1e**). Because honeycomb (non-Bravais) lattices and hexagonal (Bravais) sublattices are characterized by the same reciprocal lattice, both geometries exhibit qualitatively similar  $\Gamma$  point transmission spectra<sup>77, 82</sup> (**Figure 4.2**).

### 4.3 Dipole-Quadrupole Coupling at $\Gamma_1$ Mode

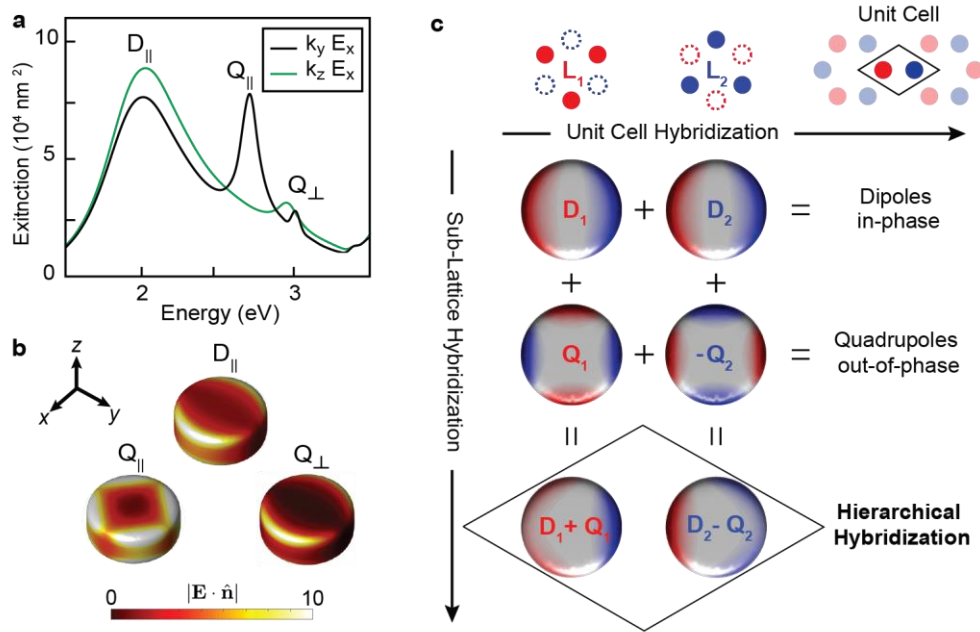


**Figure 4.3. Hierarchical Hybridization at  $\Gamma_1$  Resonance.** (a) Calculated extinction spectra of isolated Ag disks ( $d = 110$  nm and  $h = 50$  nm) excited by plane waves with incident wave vector  $\mathbf{k}$  parallel (green) and perpendicular (black) to the disk symmetry axis. The dipole mode  $D_{||}$  is excited in both cases, while the in-plane quadrupole  $Q_{||}$  is not excited with  $\mathbf{k}$  directed along the z-axis. Note that the mode near 3.0 eV under  $k_y$ ,  $E_x$  plane wave excitation is an electric octupole mode that does not noticeably contribute to the near-fields shown in Figure 1e. (b) Calculated electric fields associated with  $D_{||}$  and  $Q_{||}$  modes of the isolated disk projected onto the surface normal  $\hat{\mathbf{n}}$  highlighting different near-field spatial distributions. (c) Hierarchical hybridization scheme showing the  $\Gamma_1$  mode of the honeycomb lattice involves D-Q mixing on both sublattice (vertical) and unit cell (horizontal) levels. Red and blue colors correspond to positive and negative induced surface charges, respectively.

We identified the multipolar LSP contributions to the  $\Gamma_1$  SLR mode in honeycomb lattices by examining the LSP modes supported by both one- and two-particle hexagonal and honeycomb unit

cells. **Figure 4.3a** shows calculated extinction cross sections of a  $h = 50$  nm and  $d = 110$  nm Ag NP (single-particle unit cell) in a hexagonal sublattice under two excitation conditions. When the  $x$ -polarized incident plane wave propagates along the  $z$ -axis (green trace), a strong and broad LSP mode ( $D_{\parallel}$ ) is excited near 2 eV (620 nm) as well as a weaker mode ( $Q_{\perp}$ ) just above 3 eV (413 nm). A plane wave propagating along the  $y$ -axis and polarized along the  $x$ -axis (black trace) can also excite the  $D_{\parallel}$  mode along with a second resonance ( $Q_{\parallel}$ ) near 2.72 eV (460 nm). Calculated electric fields at the energies of the  $D_{\parallel}$  and  $Q_{\parallel}$  modes near the NP surface enable a multipolar order to be assigned based on nodal structure (**Figure 4.3b**). The near-field distribution of the  $D_{\parallel}$  mode exhibits a single  $yz$  nodal plane characteristic of the in-plane electric dipole  $D_{\parallel} \equiv p_x \hat{x}$  mode. The  $Q_{\parallel}$  mode is characterized by a set of  $xz$  and  $yz$  nodal planes and can be assigned as an in-plane quadrupole LSP mode. The  $Q_{\perp}$  mode is the out-of-plane quadrupole with  $yz$  and  $xy$  nodal planes.

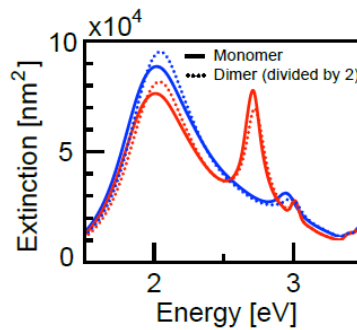


**Figure 4.4.** The spectral profiles of the Ag NP ( $d = 110$  nm;  $h = 50$  nm) dimer (dashed) closely match those of the isolated Ag NP (solid) after normalizing the former by a factor of 2 to account for the particle number. Deviations from the single-particle responses are small due to the 400 nm center-to-center distance between NPs in the dimer structure. The trace colors correspond to the plane wave excitation conditions in Figure 4.3 of the main text. Explicitly, red and blue traces correspond to incident plane waves polarized along short- and long-axes of the disc, respectively.

Interestingly, the electric near-field distribution around NPs at the  $\Gamma_1$  SLR mode of a hexagonal lattice (Figure 4.2) matches that of the  $D_{\parallel}$  mode (Figure 4.3b). This observation indicates that the  $\Gamma_1$  SLR mode of a hexagonal lattice is from hybridization between the  $D_{\parallel}$  LSPs with the Bragg mode of the lattice.

Surface charge distributions corresponding to eigenmodes of an isolated honeycomb lattice unit cell (i.e., a NP dimer) were calculated using the boundary element method (BEM) by solving for the roots of the determinant of the BEM matrix<sup>92</sup> (**Figure 4.3c**, first and second rows). The top row depicts in-phase coupling of  $D_{\parallel}$  LSP modes on  $L_1$  and  $L_2$  (labeled  $D_1$  and  $D_2$ ), and the second row depicts out-of-phase coupling of  $Q_{\parallel}$  (labeled  $Q_1$  and  $Q_2$ ) LSPs on the two sublattices. Other dimer modes, such as in-phase  $Q_{\parallel}$  and the out-of-phase  $D_{\parallel}$  modes are not considered since they are not observed in the near-field distribution (Figure 1e). Due to the relatively large NP-NP separation ( $a_0 = 400$  nm), the energies of the dimer modes are nearly degenerate with the  $D_{\parallel}$  and  $Q_{\parallel}$  modes of an isolated Ag NP (**Figure 4.4**). In contrast to a hexagonal lattice, the honeycomb lattice supports a linear combination of the in-phase  $D_{\parallel}$  and out-of-phase  $Q_{\parallel}$  hybridized LSPs, which accounts for the near-field distribution in the FDTD simulations (Figure 4.1e).

Strikingly, the hybridization scheme of plasmonic honeycomb NP lattices is distinct (Figure 4.3c) and has no analogue in either electronic or dielectric (photonic) systems. Besides hybridization across the unit cell of a non-Bravais lattice, LSP wavefunctions of a single site can self-hybridize *via* the additional photon degree of freedom from the Bragg mode. This type of multipolar mode-mixing on a single NP (self-hybridization) has been observed for cubic metal NPs on a dielectric substrate, where the coupling between in-plane D and out-of-plane Q LSP modes is mediated by the substrate.<sup>93-94</sup> This effect can be suppressed, however, if the dipole and

quadrupole LSP modes do not spectrally overlap. Plasmonic NP lattices are not constrained in this way since the single- NP LSPs are coupled *via* the Bragg lattice modes. In the case of the  $\Gamma_1$  SLR in the honeycomb lattice, the strong electromagnetic response of the multipolar LSPs and the non-Bravais character of the lattice allow the  $D_{||}$  and  $Q_{||}$  modes hybridized with the Bragg mode to become effectively degenerate on sublattices  $L_1$  and  $L_2$ . When the two hexagonal sublattices are combined to form a honeycomb lattice, hybridization occurs at both the single particle and unit-cell level—hence, hierarchical hybridization (Figure 4.3c).

#### 4.4 Dipole-Quadrupole Coupling for Lasing from Honeycomb Lattices

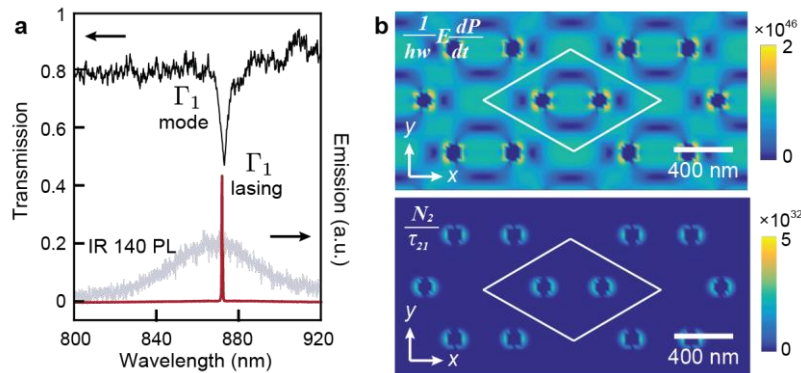


**Figure 4.5. Dipole – Quadrupole Coupling Supports Lasing at  $\Gamma_1$  Mode.** (a) Lattice mode (black) spectrally overlapped with PL of IR 140 dye solution (light blue). The lasing emission spectrum (red) exhibits characteristic linewidth narrowing close to the  $\Gamma_1$  mode of the lattice. (b) Calculated spatial distribution maps of the stimulated ( $\frac{1}{\hbar\omega} E \frac{dP}{dt}$ ) and spontaneous ( $N_2/\tau_{21}$ ) emission rates when lasing occurred in units of  $s^{-1} \cdot m^{-3}$ . The stimulated emission spatial distribution matches that of the Q mode in Figure 2b.

With a detailed understanding of mechanism of the asymmetric near-fields of the hybrid SLRs, we used plasmon lasing as a diagnostic tool to examine this  $\Gamma$  point mode further. We placed a droplet of IR-140-DMSO solution (0.5 mM) on a 2D Ag NP lattice (same dimensions as in Figure

1) on a silica substrate and pumped the dye with a TM-polarized 800-nm fs-pulsed laser (Methods). The light emitted normal to the surface had a very narrow lasing peak (FWHM  $\approx 0.2$  nm) centered

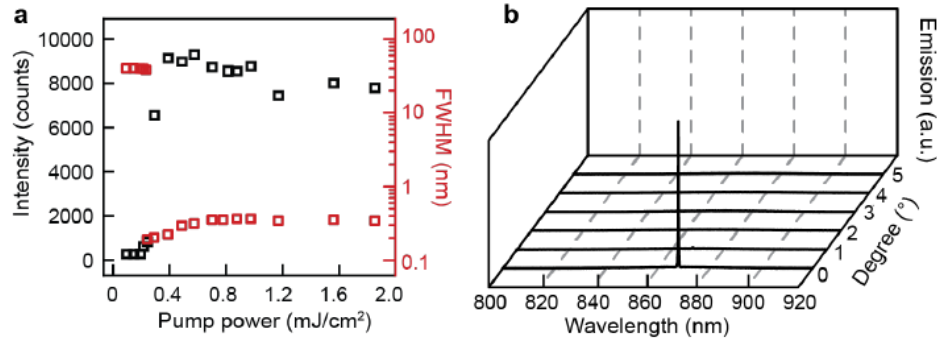


**Figure 4.6.  $\Gamma_1$  lasing characterization from Ag NP lattice.** (a) Light-light curve of  $\Gamma_1$  lasing and power-dependent emission FWHM. Lasing intensities and linewidths are plotted on linear and logarithmic scales, respectively. (b) Angle-resolved emission of  $\Gamma_1$  lasing.

at 866 nm, close to the  $\Gamma_1$  resonance (**Figure 4.5a**). Power-dependent input-output profiles showed a nonlinear increase in lasing intensity above threshold ( $\sim 0.21$  mJ/cm<sup>2</sup>), and angle-resolved emission measurements indicate that the lasing emission was from the band-edge  $\Gamma_1$  mode at  $|\mathbf{k}_{\parallel}| = 0$  (**Figure 4.6**). We used our semi-quantum four-level, one-electron model of organic gain medium coupled to FDTD calculations to simulate lasing action.<sup>17, 54, 56</sup> These calculations confirmed that the lasing occurred at the same wavelength as the  $\Gamma_1$  resonance (**Figure 4.7**). The lasing emission supported by the  $\Gamma_1$  SLR mode was at a slightly shorter wavelength compared to that of the  $\Gamma_1$  SLR mode (Figure 1c) because of refractive index changes at high pump fluences or the optical pulling effect.<sup>12, 32</sup> In contrast to plasmonic systems that have stimulated emission rate  $(\frac{1}{\hbar\omega_a} E \frac{dP_a}{dt})$  maps and spontaneous emission rate  $(N_2/\tau_{21})$  maps dominated by D-D or Q-Q coupled SLRs,<sup>12, 54, 95</sup> lasing from the honeycomb lattices showed an asymmetric distribution of the

stimulated emission rate because of hierarchical hybridization. Notably, different from the stimulated emission rate map, the spatial distribution of the spontaneous emission rate resembles that of a dipole LSP field (**Figure 4.5b**).

#### 4.5 Lasing from Two Distinct Band Edge State

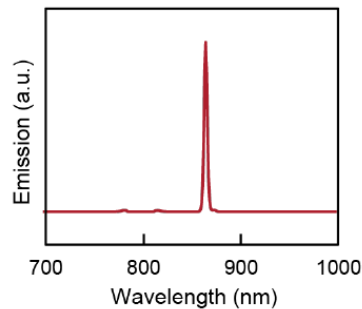


**Figure 4.7. Simulated  $\Gamma_1$  lasing emission peak matches wavelength of  $\Gamma_1$  resonance in the absence of dye. Calculation details included in the main text.**

When the particle height is small ( $< 50$  nm), the out-of-plane quadrupole degrees of freedom are not prominent in SLR excitations; however, these multipolar modes can be used to produce additional SLR modes<sup>12</sup> as NP height increases. To explore whether a single structure can incident angle (**Figure 4.8a**). At the  $\Gamma_2$  resonance, the calculated surface charge distribution and the electric field ( $|\mathbf{E}|^2/|\mathbf{E}_0|^2$ ) are localized to the upper and lower NP surfaces with  $xy$  and  $yz$  nodal planes for  $x$ -polarized light. The phase within the top- and bottom-halves of each NP are out-of-phase by  $\pi$

(Figures 4.8b, 4.9). These characteristics confirm that the  $\Gamma_2$  mode is correlated with an out-of-plane quadrupole LSP, which in earlier work was labeled as a hybrid out-of-plane quadrupole ( $Q_{\perp}$ )

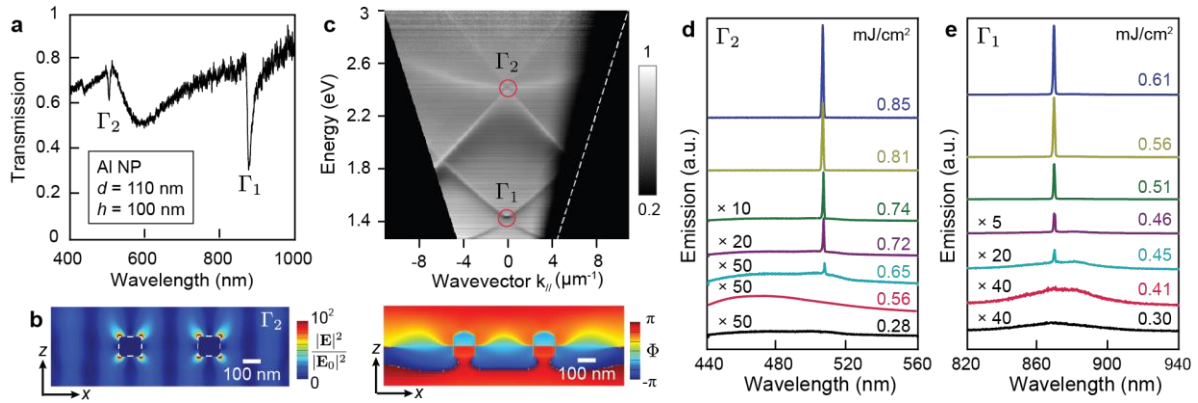


**Figure 4.8. Lasing Supported by Two Distinct Band Edge States.** (a) Measured transmission spectrum of Al NP ( $d = 110$  nm,  $h = 100$  nm) honeycomb lattice showing simultaneously optimized  $\Gamma_1$  and  $\Gamma_2$  modes. (b) Calculated electric field magnitude normalized by magnitude of incoming field ( $|\mathbf{E}|^2/|\mathbf{E}_0|^2$ ) and phase profile of the  $\Gamma_2$  mode. Scale bars are 100 nm. (c) Dispersion diagram of Al NP array under TM polarization. The white dashed line denotes the edge of dispersion diagram which is limited by the areas of fabricated NP array in experiments. (d) Measured  $\Gamma_2$  emission spectra with increasing pump power for Al NP array (LDS 473 dye concentration 20 mM). (e) Measured  $\Gamma_1$  emission spectra with increasing pump power for Al NP array (IR-140 dye concentration 0.5 mM).

lattice plasmon resonance because of the *superposition* of  $Q_{\perp}$  with an overlapping dipolar LSP.<sup>12</sup> Therefore, the sharp  $\Gamma_2$  resonance is from the stronger  $Q_{\perp}$  LSP coupled to the (1, -1) Bragg mode with only minor overlap of the dipole LSP coupled to the (1, -1) Bragg mode (Figure 4.10). Note that this superposition is different from the explicit mode-mixing of hierarchical hybridization. The dispersion diagram of the fabricated Al NP lattice was experimentally mapped along  $\Gamma$ -M using TM-polarized light and showed two band-edge states at  $\Gamma_1$  and  $\Gamma_2$  points (Figure 4.8c).

Multiple lasing peaks were previously demonstrated from a NP superlattice composed of microscale arrays of finite-lattice patches.<sup>17</sup> In contrast, by controlling the sub-wavelength lattice



**Figure 4.9: Charge distributions at  $\Gamma_2$  resonance showing the charge accumulated at four corners of Al nanoparticles.**

structure *via* unit cell design, we can access two different SLR modes that can support lasing with a wavelength separation of  $\sim 300$  nm using different organic gain. With LDS 473-DMSO (20 mM) pumped by a 400-nm fs-pulsed laser, the PL centered at 475 nm overlapped with the  $\Gamma_2$  mode. A narrow lasing peak (FWHM  $\approx 0.3$  nm) at 505 nm was observed normal to the lattice plane (**Figure 4.8d**). The light-light curve showed a nonlinear increase in lasing intensity above the lasing threshold of  $0.65$  mJ/cm<sup>2</sup>, and angle-resolved emission spectra measurements confirmed the lasing

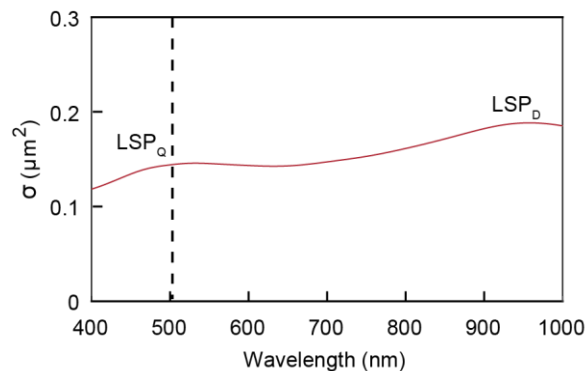


**Figure 4.10: The Bragg mode (denoted by the dash line) related to  $\Gamma_2$  resonance coupled with out-of-plane quadrupole localized surface plasmon.**

mode is from the  $\Gamma_2$  band-edge state at  $|\mathbf{k}_{\parallel}| = 0$  (**Figure 4.11**). To investigate the  $\Gamma_1$  mode, we used IR140-DMSO (0.5 mM) as gain medium and pumped with a 800-nm fs-pulsed laser. Lasing at 865 nm with a measured input power threshold value of  $0.45 \text{ mJ/cm}^2$  was achieved (**Figure 4.8e**).

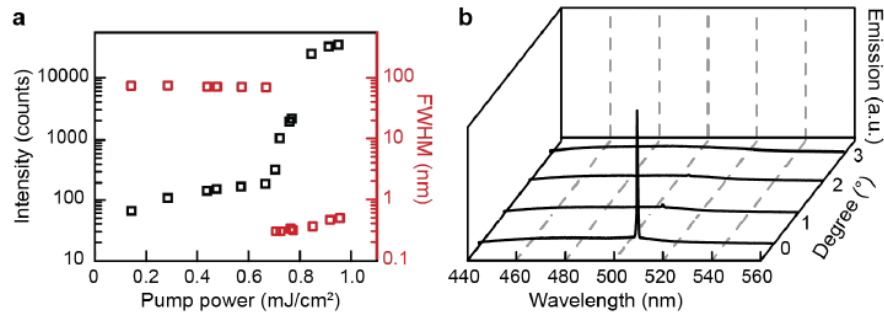


**Figure 4.11: Light-light curve and angle-resolved emission suggested that  $\Gamma_2$  lasing happened at zero wavevector. (a) Input-output curves of  $\Gamma_2$  lasing. (b) Angle-resolved emission spectra measured from  $0^\circ$  to  $3^\circ$ .**

Hence, multipolar LSPs can achieve two high quality SLRs separated by 100s of nm using a honeycomb lattice with identical NPs at each lattice site and is the first structure to realize lasing at the spectral ends of the visible regime.<sup>17</sup>

## 4.6 Summary and Outlook

We investigated the formation of hierarchically hybridized SLRs in plasmonic honeycomb NP lattices. Near the NP surface, the interplay between the non-Bravais lattice symmetry and the LSP wavefunction basis results in anisotropic electric near-field distributions that result in asymmetric spatial distributions of stimulated emission rates. By engineering NP shape, material, and spacing, we achieved two distinct band-edge states separated by more than 300 nm from a single-lattice array. This magnitude represents a key advantage of hierarchically hybridized SLRs: the lattice geometry and LSP wavefunctions can be separately tuned to create multi-polar plasmonic lattices. We anticipate our findings will be critical in tuning near-field interactions between plasmonic NP

lattices and emitters, for example in strong coupling and Bose-Einstein condensation.<sup>77, 96-99</sup> SLRs may also provide insight to photonic analogous of PT-symmetry and topological effects, especially since gain and loss in emitter-SLR systems can be exquisitely tailored.

## **4.7 Methods**

### **4.7.1 Fabrication of Al and Au NP arrays**

Arrays of Ag NPs on fused silica were fabricated with a soft nanofabrication process called PEEL.<sup>24</sup> Briefly, we generated periodic photoresist posts on Si wafers by solvent-assisted nanoscale embossing (SANE)<sup>34</sup> with controlled post size. The patterns were then transferred into free-standing Au nanohole films by depositing Cr film, removing PR posts, etching through Si nanoholes, depositing Au film, and lifting off Au film. Finally, we created NP arrays by thermal deposition through the hole-array mask on a transparent substrate and then used scotch tape to remove the Au hole mask. A 2-nm Cr layer was deposited in-between for better adhesion between Ag NPs and silica.

### **4.7.2 Lasing measurements**

A drop of a 0.5 mM IR140-DMSO solution was placed on Ag NP arrays and capped with a coverslip. The completed sample was pumped at an incident angle of  $45^\circ$  using a mode-locked Ti:sapphire laser with a regenerative amplifier (800-nm wavelength, 1 kHz operation rate and 90 fs pulse width), and the circular pump spot size was  $\sim 800 \mu\text{m}$  in diameter. Lasing signals were collected normal to the sample surface and analyzed by a charge-coupled device (CCD) spectrometer. For angle-resolved emission measurements, we fixed the sample vertically at the centre of a rotational stage and collected emission signals within detection angle from  $0^\circ$  to  $5^\circ$  in  $1^\circ$  increments manually (with respect to the sample surface normal).

### 4.7.3 FDTD simulations

FDTD calculations with commercial software (FDTD solution, Lumerical Inc., Vancouver, Canada) were used to simulate the linear optical properties and lasing emission from Ag NP arrays. The optical constants of Ag were taken from Palik measurements (400–1000 nm).<sup>36</sup> A uniform mesh size of 2 nm ( $x$ ,  $y$  and  $z$ ) was used to ensure the accuracy of electric and magnetic field calculations within the metal NPs.

Simulation of  $\Gamma_1$  lasing was performed by FDTD, where a four-level one-electron model was integrated for modeling dye molecules. In the semi-quantum systems, we set the Ag NP size  $d = 110$  nm and height  $h = 50$  nm, dye concentration  $C = 0.5$  mM, pump wavelength at  $\lambda_a = 800$  nm and dye emission at  $\lambda_e = 850$  nm with bandwidth  $\Delta\lambda_e = 120$  nm, close to experimental conditions. The spontaneous emission rate ( $N_2/\tau_{21}$ ) and stimulated emission rate ( $\frac{1}{\hbar\omega} \mathbf{E} \frac{d\mathbf{p}}{dt}$ ) were analyzed to show their spatial correlation with the plasmonic hot spots with the amplitude of pump power set to be  $8 \times 10^7$ .

## Chapter 5. M-point Lasing in Hexagonal and Honeycomb Plasmonic Lattices

### Abstract

This paper reports the observation of band-edge states at the M point in the first Brillouin zone of hexagonal and honeycomb plasmonic nanoparticle (NP) lattices. The surface lattice resonance at the M point ( $SLR_M$ ) of hexagonal arrays shows characteristics of asymmetric out-of-plane dipole coupling between silver NPs. Compared to the hexagonal lattice, two modes were observed at the M point of the honeycomb lattice. The non-Bravais nature of the honeycomb lattice and off-normal excitation result in the hybridization of the out-of-plane dipole resonance with the out-of-plane quadrupole resonance for the bluer  $SLR_M$ , and the in-plane dipole coupling at the redder  $SLR_M$  of the honeycomb lattice. By incorporating spectrally overlapped dye gain media, we achieved M-point lasing from both hexagonal and honeycomb lattices. These unexplored band-edge states are expected to contribute to the fields of nanophotonics and quantum optics

### Related reference

Manuscript in-preparation

## 5.1 Introduction

Two- and three-dimensional periodic dielectric structures known as photonic crystals can show photonic band gaps.<sup>100-101</sup> These stop bands at high-symmetry points in the Brillouin zone (BZ) of the reciprocal lattices can trap light<sup>102</sup> in the form of standing waves<sup>103</sup> and have facilitated single-molecule detection and fluorescence enhancement.<sup>104-106</sup> Two-dimensional lattices of metal nanoparticles (NPs) can support surface lattice resonances (SLRs), hybrid collective excitations that form between the localized surface plasmons of the NPs in an array with diffractive photonic modes of the lattice.<sup>53, 56, 107</sup> Because both the NP characteristics and the lattice modes can be independently tuned, the optical band structure of SLRs can be exquisitely engineered. For example, SLRs from square, hexagonal and rhombohedral lattices were realized.<sup>7, 54, 108</sup>

At the SLR wavelength, the NP lattice can strongly localize light in the subwavelength volumes around the NPs with a standing wave forming at the band-edge state.<sup>17, 56, 108</sup> Experimental studies have focused primarily on SLRs produced by dipolar plasmon excitations in cylindrical NPs coupled to high-symmetry lattices (square and hexagonal). Recently, studies have reported that engineering the NP unit cell can enable the excitation of out-of-plane quadrupole plasmons, producing hybrid quadrupole SLRs.<sup>7, 12, 108</sup> Moreover, lattices that share the same band structure (honeycomb and hexagonal) but have different unit cells can produce different SLRs due to the distinct coupling mechanisms of their unit cells.<sup>55, 82, 109</sup> The SLR at the  $\Gamma$  point ( $0^\circ$  excitation angle,  $\vec{k}_\parallel = 0$ ) in the honeycomb plasmonic lattice shows in-plane dipole coupling hybridized with in-plane quadrupole coupling while the SLR at the  $\Gamma$  point in the hexagonal lattice only shows in-plane dipole coupling.<sup>55</sup> Although studies about the K points in honeycomb lattices have been reported,<sup>109</sup> other high-symmetry points, especially those at large excitation angles, have not been

investigated because of challenges accessing these points in small patterned areas ( $\sim\mu\text{m}^2$ ).<sup>110-111</sup> Large-area patterns ( $\sim\text{cm}^2$ ) are necessary to measure large excitation angles experimentally.<sup>112-113</sup>

Topological effects in plasmonic systems are interesting because of the nanoscale-field amplification properties of localized surface plasmons and the robust transport properties of topological edge states.<sup>114-116</sup> Properties arising from system topology (topological invariants), including unidirectional chiral edge states are closely related to the interplay between lattice symmetry and the wavefunction response at each lattice site, especially at off-normal high-symmetry points.<sup>117-120</sup> We have reported the hierarchical hybridization coupling at the  $\Gamma$  point of SLRs in plasmonic honeycomb lattices.<sup>55</sup> However, the band-edge state and coupling mechanisms at off-normal high-symmetry points are unexplored. A full understanding of the band structure and coupling mechanism in plasmonic hexagonal and honeycomb lattices is necessary to investigate topology in plasmonic systems.

Here we show that six-fold rotational symmetry plasmonic lattices of silver NPs can support SLRs at the M point. In hexagonal plasmonic lattices, the single  $\text{SLR}_M$  is a result of asymmetric, out-of-plane dipole coupling between NPs. In honeycomb plasmonic lattices, two  $\text{SLR}_M$  modes were observed at the M point because of the non-Bravais nature of the honeycomb lattice (two-NP unit cells on a hexagonal lattice). We found that the two  $\text{SLR}_M$  modes in the honeycomb lattice were attributed to different hybridization couplings between NPs, where the shorter-wavelength M1 mode was from out-of-plane dipoles hybridized with out-of-plane quadrupoles while the longer-wavelength M2 mode showed only in-plane dipole coupling. M-point lasing was observed at ca.  $60^\circ$  relative to surface normal from honeycomb and hexagonal lattices of silver NP arrays.

## 5.2 Out-of-plane Dipole Coupling at M-point in Hexagonal Lattice

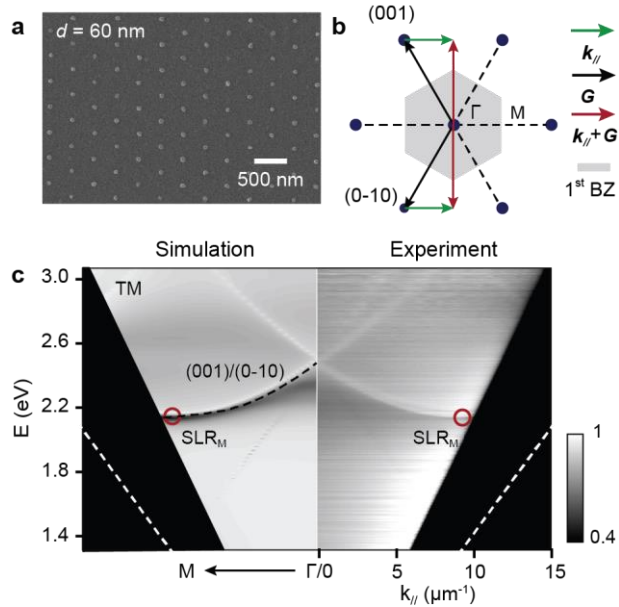


**Figure 1. M-point Band-edge State in Plasmonic Hexagonal Lattice.** (a) SEM image of fabricated hexagonal lattice ( $a_0 = 400$  nm) of Ag NPs with 80 nm diameter and 50 nm height. (b) Reciprocal space with Brillouin zone of hexagonal lattice. (c) Calculated (left) and measured (right) dispersion diagram (angle-dependent transmission of TM polarized plane wave) for the lattice in (a) along the  $\Gamma - M$  path through the Brillouin zone. The light cone in DMSO is denoted with the white dashed line.

Silver NPs arranged in a hexagonal lattice (spacing  $a_0 = 400$  nm, diameter  $d = 60$  nm, height  $h = 50$  nm) were patterned by solvent-assisted nanoscale embossing<sup>60</sup> and PEEL processes<sup>61-62</sup> on silica substrates (**Figure 1a**). **Figure 1b** depicts the hexagonal reciprocal lattice (blue dots) and the first-order Brillouin zone (BZ) (grey hexagon), with the  $\Gamma$  point in the center.  $\vec{G}_i$  is the reciprocal vector and  $\vec{k}_{\parallel}$  is the in-plane wavevector. When (001) and (0-10) modes are excited with a plane wave ( $\vec{k}_{\parallel}$ ) along x axis,  $|\vec{G}_{001} + \vec{k}_{\parallel}|$  and  $|\vec{G}_{0-10} + \vec{k}_{\parallel}|$  have the same value, suggesting the (001) and (0-10) modes are degenerated and share the same light energy.

**Figure 1c** shows excellent agreement between simulated and measured dispersion diagrams of Ag NPs in a hexagonal lattice (Methods). Under transverse magnetic (TM) polarized plane wave excitation, the dispersion properties of (001) and (0-10) are degenerate (black dashed line). At the M point ( $|\vec{k}_{\parallel}| = 9.2 \text{ } \mu\text{m}^{-1}$ ), where  $|\vec{k}_{\parallel}| = \frac{1}{2} |\vec{G}_{001}|$  (Figure 1b), the energy of photon in the lattice is at a local minimum and  $\frac{\partial E}{\partial k_{\parallel}} = 0$ , indicating the existence of a band-edge state with standing wave feature. Note we denote the plasmonic mode at the M-point band-edge state as  $\text{SLR}_M$ . The

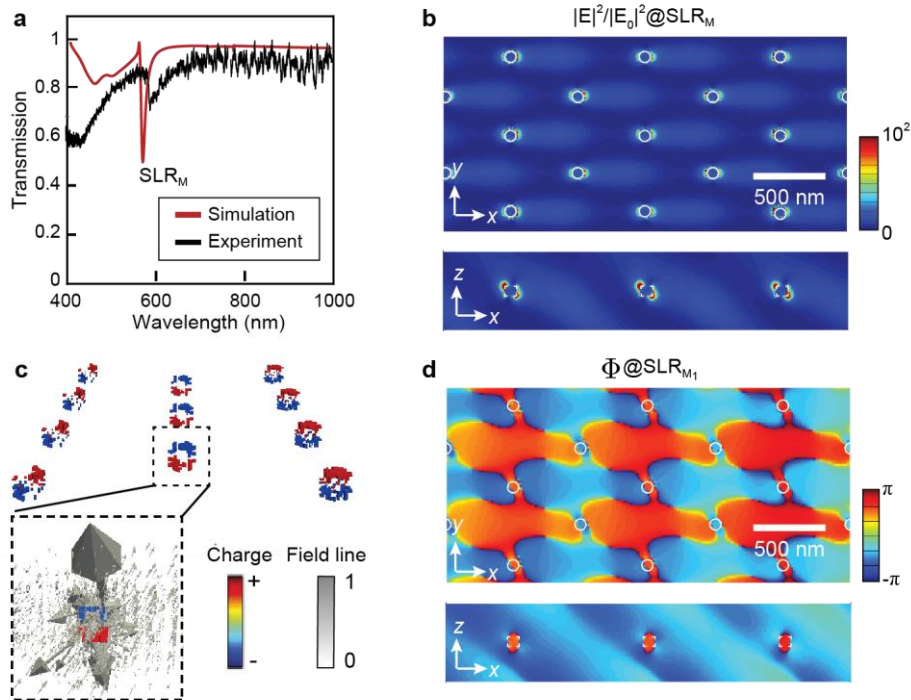


**Figure 5.2. Out-of-plane dipole coupling at  $\text{SLR}_M$ .** (a) Measured and calculated transmission spectra of lattice in Figure 1a for x-polarized plane waves at  $60^\circ$  excitation angle showing strong  $\text{SLR}_M$ . (b) Calculated electric field magnitude and (d) phase map within the XY and XZ plane of hexagonal Ag NP array showing out-of-plane dipole resonance (c) Calculated charge distribution of Ag NPs at  $\text{SLR}_M$  showing charge accumulates at the diagonal corners of NPs.

energy of  $SLR_M$  from experimental measurements is around 2.13 eV, corresponding to  $SLR_M$  at  $60^\circ$  with 582 nm wavelength in free space.

**Figure 5.2a** shows the measured and simulated transmission spectra of Ag NPs excited at  $60^\circ$ . A sharp and strong  $SLR_M$  was observed at 582 nm. We used finite-difference time-domain (FDTD) method<sup>17</sup> to investigate the near-field distributions at  $SLR_M$  (Methods). Compared with electric field intensities in XY plane, more than 400 times enhancement of electric fields was observed near the diagonal corners of Ag NPs in XZ plane (**Figure 5.2b**). The charge distributions of Ag NP array at  $SLR_M$  shows that the charges accumulated at the diagonal corners of NPs with electric vectors projected out of the plane of NP arrays, indicating an out-of-plane dipole resonance

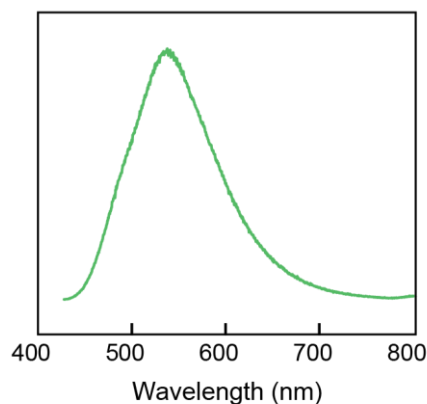


**Figure 5.3. Photoluminescence of C-540 dye dissolved into DMSO centers at 536 nm wavelength.**

(**Figure 5.2c**). Few charges on the other diagonal corners resulted from the anisotropic shape of NPs. The calculated phase mapping of NPs at  $SLR_M$  shows an alternative  $\pi$  phase change along the diagonal axis in XY plane and uniform phase in the XZ plane, suggesting the formation of a standing wave (**Figure 5.2d**). The phase fronts of the standing-wave patterns are along the

direction of (001) / (0-10) mode. Therefore, the  $SLR_M$  of hexagonal lattice comes from the out-of-plane dipole resonance coupled with the (001) / (0-10) diffraction mode.

### 5.3 M-point Lasing from Hexagonal Lattice

SLRs at  $\Gamma$  point have been used as optical feedbacks for plasmonic nanolaser emitted at  $0^\circ$ .<sup>54, 56, 108</sup> Whether the  $SLR_M$  can support plasmonic lasing remains a question. To identify the  $SLR_M$  as an optical feedback, we put a droplet of 20mM C540-DMSO dye solution on top of the NP array and encapsulated the dye solution with a cover glass slide. The C540-DMSO dye solution has a

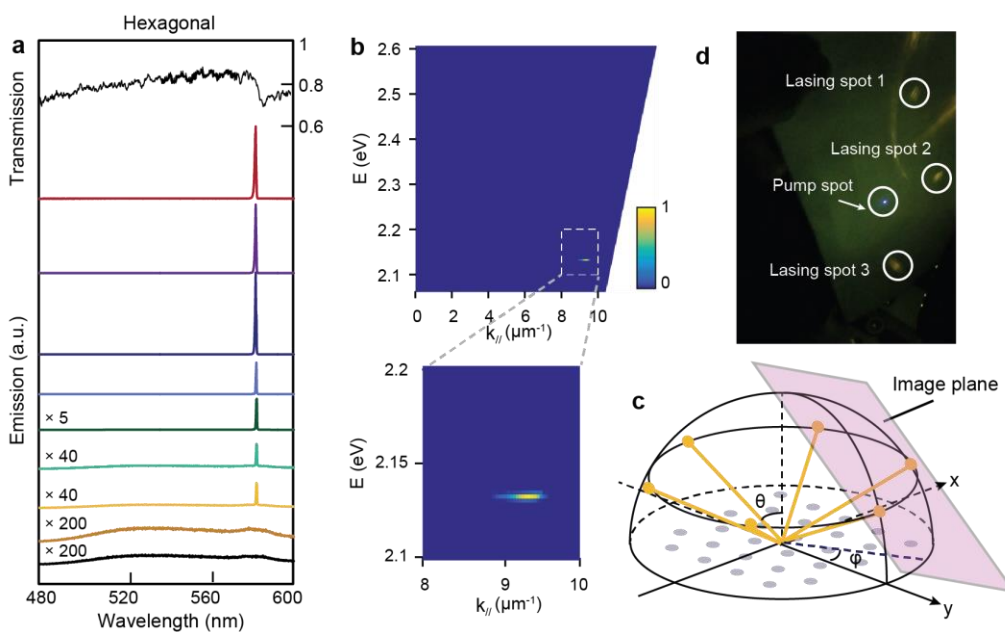


**Figure 5.4. Out-of-plane Dipole Coupling Supports Lasing at  $SLR_M$  Mode of Hexagonal Lattice.** (a)  $SLR_M$  lasing at 583 nm emission out-put of Ag NP array with PL of C540 dye solution. The lasing signal was detected at  $59^\circ$ . (b) Angle-resolved emission mapping shows that the  $SLR_M$  lasing from Ag NP array emitted at  $9.2 \mu\text{m}^{-1}$  ( $\sim 59^\circ$ ). (c) Scheme of  $SLR_M$  lasing emission from hexagonal array. (d) Imaged  $SLR_M$  laser spots indicating the six-fold symmetry of  $SLR_M$  lasing.

broad photoluminescence that can be spectrally overlapped with the  $SLR_M$  of hexagonal lattice (**Figure 5.3**). We pumped the whole device with 400nm wavelength femtosecond pulsed laser. Lasing at 583 nm with threshold value of  $0.21\text{mJ}/\text{cm}^2$  was observed at  $59^\circ$ , indicating it is supported by  $SLR_M$  (**Figure 5.4a and 5.5**). The angle-resolved emission map shows lasing at  $SLR_M$  resonance is directional at  $59^\circ$  ( $|\vec{k}_{\parallel}| = 9.2\ \mu\text{m}^{-1}, E = 2.13\ \text{eV}$ ) (**Figure 5.4b**). Furthermore, as indicated in Figure 1b, the high-symmetry M point has six-fold symmetry in hexagonal array. The  $SLR_M$  lasing should also have six-fold symmetry (**Figure 5.4c**). Considering

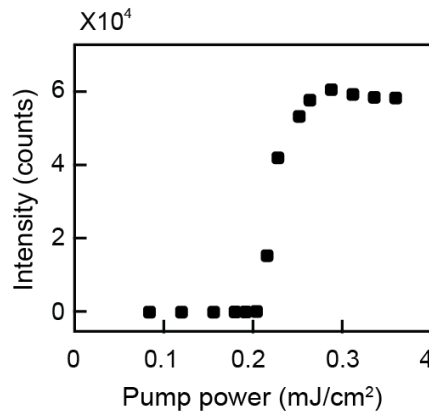


**Figure 5.5: Light-light curve of  $SLR_M$  lasing from hexagonal lattice.**

the mirror symmetry of hexagonal lattice along y axis, we put a piece of white paper in front of the device to image half of the plane of lasing emission (the other plane was not accessed to avoid blocking the pump source to the sample) (**Figure 5.4c**). Three laser beams were observed on the white paper, revealing the six-fold symmetry of  $SLR_M$  lasers (**Figure 5.4d**).

## 5.4 M-point Band-edge State from Honeycomb Lattice

Recent work reported the coupling difference between hexagonal and honeycomb lattice at  $\Gamma$  point.<sup>55</sup> Because honeycomb lattice shares the same reciprocal lattice with hexagonal lattice, a similar M-point band-edge state is expected in honeycomb lattice. To verify whether the  $SLR_M$  of

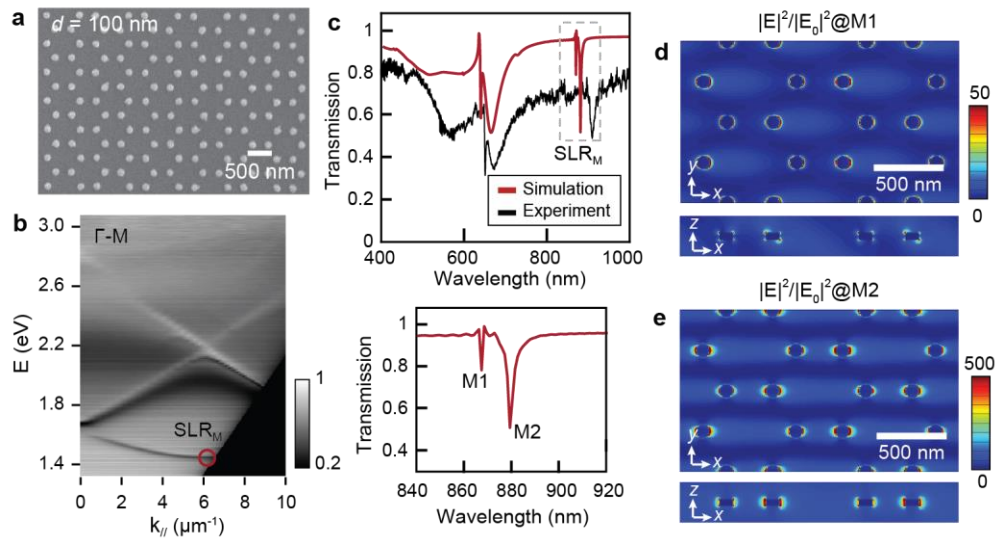


**Figure 5.6. Mode Splitting at the M-point of Plasmonic Honeycomb Lattice.** (a) SEM image of fabricated honeycomb lattice ( $a_0 = 346$  nm) of Ag NPs with 100 nm diameter and 50 nm height. (b) Measured dispersion diagram (angle-dependent transmission of TM polarized plane wave) for the lattice in (a) along the  $\Gamma - M$  path through the Brillouin zone. (c) Measured and calculated transmission spectra of lattice in (a) for x-polarized plane waves with  $60^\circ$  excitation angle showing two  $SLR_M$  resonances (shown in the zoomed-in image). (d) Near-field electric distributions indicates the hybridization between out-of-plane dipole and out-of-plane quadrupole resonance at M1. (e) Near-field electric distributions shows the in-plane dipole coupling at M2.

honeycomb lattice still exhibits out-of-plane dipole coupling, we fabricated Ag NP (diameter  $d = 100$  nm, height  $h = 50$  nm) array in honeycomb lattice in which the distance for nearest two NPs ( $a_0$ ) is 346 nm (**Figure 5.6a**). The measured dispersion diagram of the Ag NP array in honeycomb lattice shows the M-point band-edge state is located at  $|\vec{k}_{\parallel}| = 6.1 \text{ } \mu\text{m}^{-1}$  with 1.42eV energy, corresponding to  $\text{SLR}_M$  at  $60^\circ$  with 871 nm wavelength (**Figure 5.6b**). However, unlike hexagonal array, both the experimental and simulated transmission spectra at  $60^\circ$  present the splitting of  $\text{SLR}_M$  in honeycomb lattice (**Figure 5.6c**). Two SLRs (M1 at 869 nm and M2 at 880 nm) at M

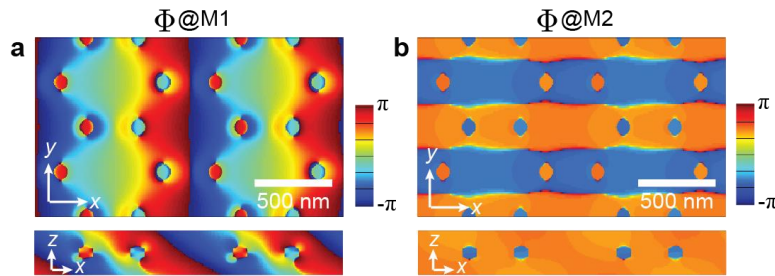


**Figure 5.7. Phase mapping of M1 and M2 modes.**

point were observed, which result from the interactions of two sub-hexagonal lattices. Furthermore, we used FDTD simulation to study the coupling mechanisms of the two SLRs. The near-field electric distributions at the M1 mode shows that in a single unit cell (two nearest NPs), one NP has out-of-plane quadrupole resonance and the other NP has out-of-plane dipole resonance (**Figure 5.6d**). The calculated phase mapping at M1 mode shows a phase change inside of NP at XZ plane also identified the existence of out-of-plane quadrupole coupling (**Figure 5.7a**). On the other hand, the near-field electric distributions at M2 mode shows that the electrons oscillate in the XY plane, and NPs have uniform phase distributions (**Figure 5.6e and 5.7b**), indicating an in-plane dipole coupling. The sweeping of the NP diameter and height further demonstrated our statements (**Figure 5.8**). The M1 mode becomes stronger with increasing the NP height at constant

NP diameter. Larger NP height contributes to stronger out-of-plane coupling (either dipole or quadrupole), which leads to the stronger M1 mode. Keeping the height of Ag NPs at 50 nm and

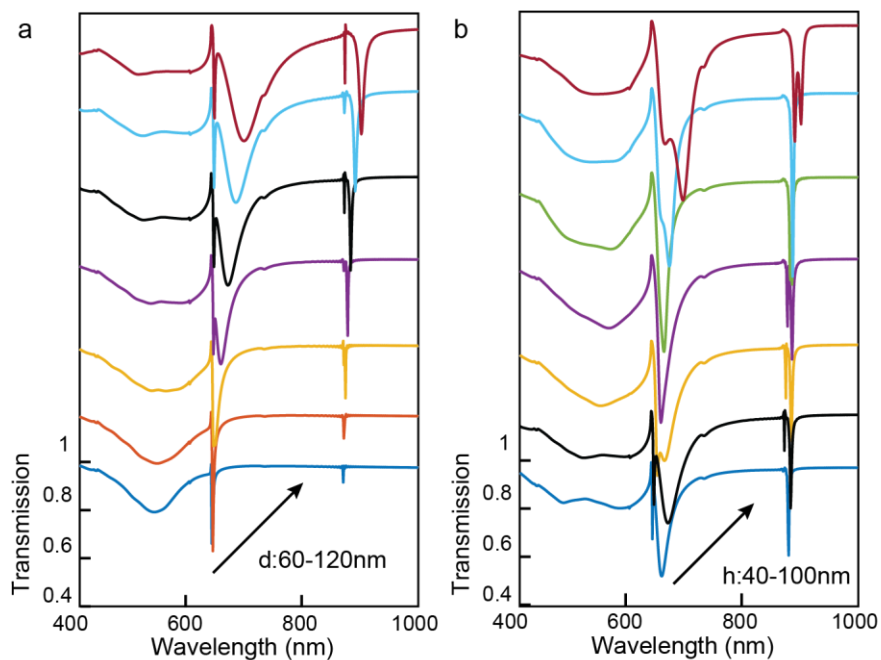


**Figure 5.8. Simulated transmission spectra at  $60^\circ$  from honeycomb lattice. (a)** Sweeping the NP diameter and fixing NP height to be 50 nm. **(b)** Sweeping the NP height and fixing diameter to be 100 nm.

increasing the NP diameter results in stronger in-plane dipole LSPs. The simulated transmission spectra show stronger M2 mode, suggesting the in-plane dipole coupling at M2 mode.

## 5.5 M-point Lasing from Honeycomb Lattice

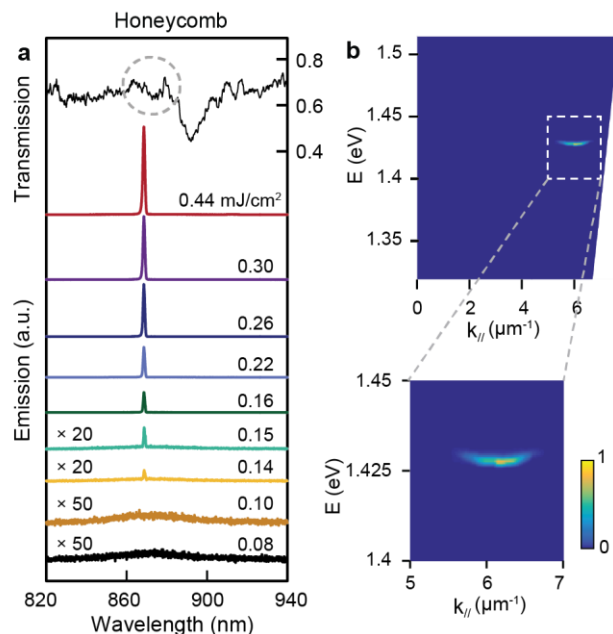


**Figure 5.9. M-point Lasing from Plasmonic Honeycomb Lattice.** (a) M1 lasing at 868 nm emission out-put of Ag NP array with PL of IR140 dye solution. The lasing signals were detected at  $58^\circ$ . (b) Angle-resolved emission mapping shows that the  $SLR_M$  lasing from Ag NP honeycomb lattice emitted at  $6.2 \mu\text{m}^{-1}$  ( $\sim 58^\circ$ ).

To investigate how M1 and M2 modes contribute to lasing emission process, we incorporated 1mM IR140-DMSO solution, which has spectrally overlap with M1 and M2 mode (SI). Under 800 nm wavelength femtosecond pulsed laser pump, we observed lasing emission at 868 nm wavelength from  $58^\circ$  detection angle with threshold value around  $0.15\text{mJ}/\text{cm}^2$  (**Figure 5.9a and 5.10**). The wavelength of  $SLR_M$  lasing matches with the wavelength of M1 mode, suggesting that the M1 mode supports  $SLR_M$  lasing in honeycomb lattice. Interestingly, we did not observe any lasing signal that is supported by M2 mode. The angle-resolved emission shows the lasing is directional at  $6.2 \mu\text{m}^{-1}$  with  $\sim 1.43 \text{ eV}$  energy ( $58^\circ$  degree with 868 nm wavelength), which is near

the M-point band-edge state in the bandstructure of honeycomb lattice (**Figure 5.9b and 5.6b**). This may suggest the importance of the near-field coupling, that the out-of-plane dipole coupling in this system can contribute to the M-point plasmonic lasing.

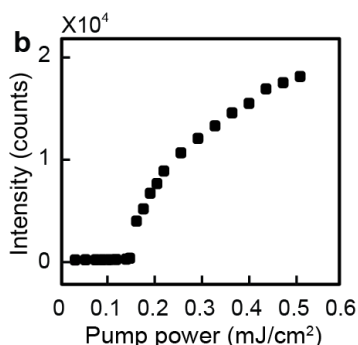


**Figure 5.10: Light-light curve of SLR<sub>M</sub> lasing from honeycomb lattice.**

## 5.6 Summary and Outlook

In summary, we investigated the coupling mechanisms of SLR<sub>M</sub> from Ag NP arrays in hexagonal and honeycomb lattices. Unlike the out-of-plane dipole coupling of SLR<sub>M</sub> in hexagonal lattice, the non-Bravais nature of honeycomb lattice introduces high-order coupling, resulting in mode splitting at the M point. We identified the out-of-plane dipole coupling related SLR<sub>M</sub> from hexagonal and honeycomb lattices can support plasmonic lasing emitted at M- point. Our results reveal the importance of lattice geometry in multipolar LSPR coupling and the formation of M-point band-edge states. We anticipate that our findings will be beneficial for nanophotonics, quantum optics, electrical engineering, and the greater nanotechnology communities.

## 5.7 Methods

### 5.7.1 Fabrication of Ag NP arrays

We fabricated Ag NP arrays on fused silica with a soft nanofabrication process. First, we fabricated periodic photoresist posts on Si wafers by solvent-assisted nanoscale embossing (SANE<sup>60</sup>). Following with Cr deposition, removal of photoresist posts, etching through the Si nanoholes, depositing Au film and wet etching the Cr layer, we can lift off a free-standing Au hole film on fused silica. The Ag NP array is generated by depositing Ag through the Au hole mask on fused silica and peel off the Au hole mask with scotch tape. A 2-nm Cr layer was deposited as an adhesive layer. A 5-nm Al<sub>2</sub>O<sub>3</sub> layer was deposited on the surface of Ag NPs to prevent oxidation of Ag.

### 5.7.2 Band structure measurements

We characterized the optical band structure of Ag NP lattices by compiling transmission spectra at different incident angles. In the experiment, the samples were placed at the center of a program-controlled rotational stage. The transmission spectra were collected by sweeping incident angles  $\theta$  from 0° to 70° in 1° increments using an automated, home-built National Instruments Lab-VIEW program. Band structures of the Ag NP lattices in wavelength ( $\lambda$ ) - incident angle ( $\theta$ ) units can be transferred to energy ( $E$ ) - wavevector ( $k_{//}$ ) format by  $E = hc/\lambda$  and  $k_{//} = (2\pi/\lambda) \sin\theta$ .

### 5.7.3 FDTD simulations

FDTD calculations with commercial software (FDTD solution, Lumerical Inc., Vancouver, Canada) were used to simulate the linear optical properties from Ag NP lattices. The optical constants of Ag were taken from Palik constant<sup>121</sup>. The bfast source and a uniform mesh size of 5

nm ( $x$ ,  $y$  and  $z$ ) was used for the near-field electric and phase mapping calculations within the metal NPs.

#### **5.7.4 Lasing measurements**

The plasmonic laser from hexagonal lattice was optically pumped using 35 fs, 400-nm laser pulses with a repetition rate of 100Hz, beam diameter of  $\sim 800 \mu\text{m}$ . The plasmonic laser from honeycomb lattice was optically pumped using 35fs, 800-nm pulsed laser with a repetition rate of 1kHz, beam diameter of  $\sim 800 \mu\text{m}$ . The incident excitation angle for both two pump conditions is around  $30^\circ$ . Lasing signals were collected normal to the sample surface and detected by a charge-coupled device (CCD) spectrometer.

## References

1. Henzie, J.; Lee, J.; Lee, M. H.; Hasan, W.; Odom, T. W., Nanofabrication of plasmonic structures. *Annual review of physical chemistry* **2009**, *60*, 147-165.
2. Kim, M.-G.; Shin, Y.-B.; Jung, J.-M.; Ro, H.-S.; Chung, B. H., Enhanced sensitivity of surface plasmon resonance (SPR) immunoassays using a peroxidase-catalyzed precipitation reaction and its application to a protein microarray. *Journal of immunological methods* **2005**, *297* (1), 125-132.
3. Bauch, M.; Toma, K.; Toma, M.; Zhang, Q.; Dostalek, J., Plasmon-enhanced fluorescence biosensors: a review. *Plasmonics* **2014**, *9* (4), 781-799.
4. Liu, Z.; Hou, W.; Pavaskar, P.; Aykol, M.; Cronin, S. B., Plasmon resonant enhancement of photocatalytic water splitting under visible illumination. *Nano letters* **2011**, *11* (3), 1111-1116.
5. Zhou, W.; Dridi, M.; Suh, J. Y.; Kim, C. H.; Co, D. T.; Wasielewski, M. R.; Schatz, G. C.; Odom, T. W., Lasing action in strongly coupled plasmonic nanocavity arrays. *Nature nanotechnology* **2013**, *8* (7), 506-511.
6. Wang, D.; Yang, A.; Hryn, A. J.; Schatz, G. C.; Odom, T. W., Superlattice plasmons in hierarchical Au nanoparticle arrays. *ACS Photonics* **2015**, *2* (12), 1789-1794.
7. Yang, A.; Hryn, A. J.; Bourgeois, M. R.; Lee, W.-K.; Hu, J.; Schatz, G. C.; Odom, T. W., Programmable and reversible plasmon mode engineering. *Proceedings of the National Academy of Sciences* **2016**, *113* (50), 14201-14206.
8. Henzie, J.; Lee, J.; Lee, M. H.; Hasan, W.; Odom, T. W., Nanofabrication of plasmonic structures. *Annual review of physical chemistry* **2009**, *60*.
9. Kelly, K. L.; Coronado, E.; Zhao, L. L.; Schatz, G. C., The optical properties of metal nanoparticles: the influence of size, shape, and dielectric environment. ACS Publications: 2003.
10. Humphrey, A. D.; Barnes, W. L., Plasmonic surface lattice resonances on arrays of different lattice symmetry. *Physical Review B* **2014**, *90* (7), 075404.
11. Vecchi, G.; Giannini, V.; Rivas, J. G., Surface modes in plasmonic crystals induced by diffractive coupling of nanoantennas. *Physical Review B* **2009**, *80* (20), 201401.
12. Wang, D.; Bourgeois, M. R.; Lee, W.-K.; Li, R.; Trivedi, D.; Knudson, M. P.; Wang, W.; Schatz, G. C.; Odom, T. W., Stretchable Nanolasing from Hybrid Quadrupole Plasmons. *Nano letters* **2018**.
13. Yang, A.; Hoang, T. B.; Dridi, M.; Deeb, C.; Mikkelsen, M. H.; Schatz, G. C.; Odom, T. W., Real-time tunable lasing from plasmonic nanocavity arrays. *Nature communications* **2015**, *6*, 6939.
14. Schokker, A. H.; Koenderink, A. F., Lasing at the band edges of plasmonic lattices. *Physical Review B* **2014**, *90* (15), 155452.
15. Shi, X.; Wang, Y.; Wang, Z.; Wei, S.; Sun, Y.; Liu, D.; Zhou, J.; Zhang, Y.; Shi, J., Random lasing with a high quality factor over the whole visible range based on cascade energy transfer. *Advanced Optical Materials* **2014**, *2* (1), 88-93.
16. Wang, W.; Ramezani, M.; Väkeväinen, A. I.; Törmä, P.; Rivas, J. G.; Odom, T. W., The rich photonic world of plasmonic nanoparticle arrays. *Materials Today* **2017**.
17. Wang, D.; Yang, A.; Wang, W.; Hua, Y.; Schaller, R. D.; Schatz, G. C.; Odom, T. W., Band-edge engineering for controlled multi-modal nanolasing in plasmonic superlattices. *Nature nanotechnology* **2017**, *12* (9), 889.

18. Ross, M. B.; Schatz, G. C., Radiative effects in plasmonic aluminum and silver nanospheres and nanorods. *Journal of Physics D: Applied Physics* **2014**, *48* (18), 184004.
19. West, P. R.; Ishii, S.; Naik, G. V.; Emani, N. K.; Shalaev, V. M.; Boltasseva, A., Searching for better plasmonic materials. *Laser & Photonics Reviews* **2010**, *4* (6), 795-808.
20. Knight, M. W.; King, N. S.; Liu, L.; Everitt, H. O.; Nordlander, P.; Halas, N. J., Aluminum for plasmonics. *ACS nano* **2013**, *8* (1), 834-840.
21. Castro-Lopez, M.; Brinks, D.; Sapienza, R.; van Hulst, N. F., Aluminum for nonlinear plasmonics: resonance-driven polarized luminescence of Al, Ag, and Au nanoantennas. *Nano letters* **2011**, *11* (11), 4674-4678.
22. Gérard, D.; Gray, S. K., Aluminium plasmonics. *Journal of Physics D: Applied Physics* **2014**, *48* (18), 184001.
23. Henzie, J.; Lee, M. H.; Odom, T. W., Multiscale patterning of plasmonic metamaterials. *Nature nanotechnology* **2007**, *2* (9), 549.
24. Henzie, J.; Barton, J. E.; Stender, C. L.; Odom, T. W., Large-area nanoscale patterning: chemistry meets fabrication. *Accounts of chemical research* **2006**, *39* (4), 249-257.
25. Oulton, R. F.; Sorger, V. J.; Zentgraf, T.; Ma, R.-M.; Gladden, C.; Dai, L.; Bartal, G.; Zhang, X., Plasmon lasers at deep subwavelength scale. *Nature* **2009**, *461* (7264), 629.
26. Brandi, F.; Velchev, I.; Neshev, D.; Hogervorst, W.; Ubachs, W., A narrow-band wavelength-tunable laser system delivering high-energy 300 ps pulses in the near-infrared. *Review of scientific instruments* **2003**, *74* (1), 32-37.
27. Sorger, V. J.; Zhang, X., Spotlight on plasmon lasers. *Science* **2011**, *333* (6043), 709-710.
28. Wang, D.; Wang, W.; Knudson, M. P.; Schatz, G. C.; Odom, T. W., Structural engineering in plasmon nanolasers. *Chemical reviews* **2017**, *118* (6), 2865-2881.
29. Wang, W.; Ramezani, M.; Väkeväinen, A. I.; Törmä, P.; Rivas, J. G.; Odom, T. W., The rich photonic world of plasmonic nanoparticle arrays. *Materials today* **2018**, *21* (3), 303-314.
30. Ordal, M. A.; Bell, R. J.; Alexander, R. W.; Long, L. L.; Querry, M. R., Optical properties of fourteen metals in the infrared and far infrared: Al, co, cu, au, fe, pb, mo, ni, pd, pt, ag, ti, v, and w. *Applied optics* **1985**, *24* (24), 4493-4499.
31. Babar, S.; Weaver, J., Optical constants of Cu, Ag, and Au revisited. *Applied Optics* **2015**, *54* (3), 477-481.
32. Willner, A. E.; Byer, R. L.; Chang-Hasnain, C. J.; Forrest, S. R.; Kressel, H.; Kogelnik, H.; Tearney, G. J.; Townes, C. H.; Zervas, M. N., Optics and photonics: Key enabling technologies. *Proceedings of the IEEE* **2012**, *100* (Special Centennial Issue), 1604-1643.
33. Dridi, M.; Schatz, G. C., Model for describing plasmon-enhanced lasers that combines rate equations with finite-difference time-domain. *JOSA B* **2013**, *30* (11), 2791-2797.
34. Lee, M. H.; Huntington, M. D.; Zhou, W.; Yang, J.-C.; Odom, T. W., Programmable soft lithography: solvent-assisted nanoscale embossing. *Nano letters* **2010**, *11* (2), 311-315.
35. Palik, E.; Ghosh, G., Handbook of Optical Constants of Solids (Orlando, FL: Academic). **1985**.
36. Johnson, P. B.; Christy, R.-W., Optical constants of the noble metals. *Physical review B* **1972**, *6* (12), 4370.
37. Sun, Y.; Giebink, N. C.; Kanno, H.; Ma, B.; Thompson, M. E.; Forrest, S. R., Management of singlet and triplet excitons for efficient white organic light-emitting devices. *Nature* **2006**, *440* (7086), 908-912.

38. Fukuda, Y.; Watanabe, T.; Wakimoto, T.; Miyaguchi, S.; Tsuchida, M., An organic LED display exhibiting pure RGB colors. *Synthetic Metals* **2000**, *111*, 1-6.
39. Blasse, G.; Brill, A., A new phosphor for flying - spot cathode - ray tubes for color television: yellow - emitting Y3Al5O12 - Ce<sup>3+</sup>. *Applied Physics Letters* **1967**, *11* (2), 53-55.
40. Hargis, D.; Earman, A., Lasers replace conventional technology in display designs. *Laser focus world* **1998**, *34* (7), 145-149.
41. Chow, W. W.; Koch, S. W.; Sargent, M. I., *Semiconductor-laser physics*. Springer Science & Business Media: 2012.
42. Jeong, Y. e.; Sahu, J.; Payne, D.; Nilsson, J., Ytterbium-doped large-core fiber laser with 1.36 kW continuous-wave output power. *Optics express* **2004**, *12* (25), 6088-6092.
43. Zhao, J.; Yan, Y.; Gao, Z.; Du, Y.; Dong, H.; Yao, J.; Zhao, Y. S., Full-color laser displays based on organic printed microlaser arrays. *Nature communications* **2019**, *10* (1), 870.
44. Chen, H.; Guo, K.; Yang, H.; Wu, D.; Yuan, F., Thoracic pedicle screw placement guide plate produced by three-dimensional (3-D) laser printing. *Medical science monitor: international medical journal of experimental and clinical research* **2016**, *22*, 1682.
45. Chen, S.; Liu, W.; Li, Z.; Cheng, H.; Tian, J., Metasurface - Empowered Optical Multiplexing and Multifunction. *Advanced Materials* **2020**, *32* (3), 1805912.
46. Liu, Z.; Yin, L.; Ning, H.; Yang, Z.; Tong, L.; Ning, C.-Z., Dynamical color-controllable lasing with extremely wide tuning range from red to green in a single alloy nanowire using nanoscale manipulation. *Nano letters* **2013**, *13* (10), 4945-4950.
47. Ding, Y.; Yang, Q.; Guo, X.; Wang, S.; Gu, F.; Fu, J.; Wan, Q.; Cheng, J.; Tong, L., Nanowires/microfiber hybrid structure multicolor laser. *Optics express* **2009**, *17* (24), 21813-21818.
48. Brunner, M.; Gulden, K.; Hovel, R.; Moser, M.; Carlin, J. F.; Stanley, R. P.; Ilegems, M., Continuous-wave dual-wavelength lasing in a two-section vertical-cavity laser. *IEEE Photonics Technology Letters* **2000**, *12* (10), 1316-1318.
49. Kou, Q.; Yesilyurt, I.; Chen, Y., Collinear dual-color laser emission from a microfluidic dye laser. *Applied physics letters* **2006**, *88* (9), 091101.
50. Fan, L.; Fallahi, M.; Hader, J.; Zakharian, A. R.; Moloney, J. V.; Stolz, W.; Koch, S. W.; Bedford, R.; Murray, J. T., Linearly polarized dual-wavelength vertical-external-cavity surface-emitting laser. *Applied physics letters* **2007**, *90* (18), 181124.
51. Naderi, N. A.; Grillot, F.; Yang, K.; Wright, J. B.; Gin, A.; Lester, L. F., Two-color multi-section quantum dot distributed feedback laser. *Optics express* **2010**, *18* (26), 27028-27035.
52. Zhang, C.; Yang, L.; Zhao, J.; Liu, B.; Han, M. Y.; Zhang, Z., White - light emission from an integrated upconversion nanostructure: toward multicolor displays modulated by laser power. *Angewandte Chemie International Edition* **2015**, *54* (39), 11531-11535.
53. Kelly, K. L.; Coronado, E.; Zhao, L. L.; Schatz, G. C., The optical properties of metal nanoparticles: The influence of size, shape, and dielectric environment. *J Phys Chem B* **2003**, *107* (3), 668-677.
54. Knudson, M. P.; Li, R.; Wang, D.; Wang, W.; Schaller, R. D.; Odom, T. W., Polarization-Dependent Lasing Behavior from Low-Symmetry Nanocavity Arrays. *ACS nano* **2019**.

55. Li, R.; Bourgeois, M. R.; Cherqui, C.; Guan, J.; Wang, D.; Hu, J.; Schaller, R. D.; Schatz, G. C.; Odom, T. W., Hierarchical Hybridization in Plasmonic Honeycomb Lattices. *Nano letters* **2019**, *19* (9), 6435-6441.
56. Zhou, W.; Dridi, M.; Suh, J. Y.; Kim, C. H.; Co, D. T.; Wasielewski, M. R.; Schatz, G. C.; Odom, T. W., Lasing action in strongly coupled plasmonic nanocavity arrays. *Nat Nano* **2013**, *8*, 506-511.
57. Yang, A.; Wang, D.; Wang, W.; Odom, T. W., Coherent Light Sources at the Nanoscale. *Annual Review of Physical Chemistry* **2017**, *68* (1), 83-99.
58. Dridi, M.; Schatz, G. C., Lasing action in periodic arrays of nanoparticles. *JOSA B* **2015**, *32* (5), 818-823.
59. Yang, A.; Li, Z.; Knudson, M. P.; Hryn, A. J.; Wang, W.; Aydin, K.; Odom, T. W., Unidirectional lasing from template-stripped two-dimensional plasmonic crystals. *ACS nano* **2015**, *9* (12), 11582-11588.
60. Lee, M. H.; Huntington, M. D.; Zhou, W.; Yang, J.-c.; Odom, T. W., Programmable Soft Lithography : Solvent-Assisted Nanoscale Embossing. *Nano Lett.* **2011**, *11*, 311-315.
61. Henzie, J.; Kwak, E. S.; Odom, T. W., Mesoscale metallic pyramids with nanoscale tips. *Nano letters* **2005**, *5* (7), 1199-202.
62. Gao, H.; Henzie, J.; Odom, T. W., Direct evidence for surface plasmon-mediated enhanced light transmission through metallic nanohole arrays. *Nano letters* **2006**, *6* (9), 2104-8.
63. Guan, J.; Sagar, L. K.; Li, R.; Wang, D.; Bappi, G.; Watkins, N. E.; Bourgeois, M. R.; Levina, L.; Fan, F.; Hoogland, S.; Voznyy, O.; Martins de Pina, J.; Schaller, R. D.; Schatz, G. C.; Sargent, E. H.; Odom, T. W., Engineering Directionality in Quantum Dot Shell Lasing Using Plasmonic Lattices. *Nano Letters* **2020**, *20* (2), 1468-1474.
64. Johnson, P. B.; Christy, R. W., Optical constants of the noble metals. *Phys. Rev. B* **1972**, *6*, 4370.
65. Aufray, B.; Kara, A.; Vizzini, S.; Oughaddou, H.; Leandri, C.; Ealet, B.; Le Lay, G., Graphene-like silicon nanoribbons on Ag (110): A possible formation of silicene. *Applied Physics Letters* **2010**, *96* (18), 183102.
66. Durgun, E.; Tongay, S.; Ciraci, S., Silicon and III-V compound nanotubes: structural and electronic properties. *Physical Review B* **2005**, *72* (7), 075420.
67. Ataca, C.; Sahin, H.; Ciraci, S., Stable, single-layer MX<sub>2</sub> transition-metal oxides and dichalcogenides in a honeycomb-like structure. *The Journal of Physical Chemistry C* **2012**, *116* (16), 8983-8999.
68. Kane, C. L.; Mele, E. J., Quantum spin Hall effect in graphene. *Phys Rev Lett* **2005**, *95* (22), 226801.
69. Haynes, C. L.; Mcfarland, A. D.; Zhao, L.; Duyne, R. P. V.; Schatz, G. C.; Gunnarsson, L.; Prikulis, J.; Kasemo, B.; Ka, M., Nanoparticle Optics : The Importance of Radiative Dipole Coupling in Two-Dimensional. **2003**, 7337-7342.
70. Cahangirov, S.; Topsakal, M.; Aktürk, E.; Şahin, H.; Ciraci, S., Two-and one-dimensional honeycomb structures of silicon and germanium. *Physical review letters* **2009**, *102* (23), 236804.
71. Li, T.; Galli, G., Electronic properties of MoS<sub>2</sub> nanoparticles. *The Journal of Physical Chemistry C* **2007**, *111* (44), 16192-16196.

72. Polini, M.; Guinea, F.; Lewenstein, M.; Manoharan, H. C.; Pellegrini, V., Artificial honeycomb lattices for electrons, atoms and photons. *Nature nanotechnology* **2013**, *8* (9), 625.
73. Weick, G.; Woollacott, C.; Barnes, W. L.; Hess, O.; Mariani, E., Dirac-like plasmons in honeycomb lattices of metallic nanoparticles. *Physical Review Letters* **2013**, *110*, 1-6.
74. Odom, T. W.; Gao, H.; McMahon, J. M.; Henzie, J.; Schatz, G. C., Plasmonic superlattices: Hierarchical subwavelength hole arrays. *Chem. Phys. Lett.* **2009**, *483* (4-6), 187-192.
75. Ramezani, M.; Halpin, A.; Feist, J.; Van Hoof, N.; Fernández-Domínguez, A. I.; Garcia-Vidal, F. J.; Gómez Rivas, J., Dispersion Anisotropy of Plasmon–Exciton–Polaritons in Lattices of Metallic Nanoparticles. *ACS Photonics* **2017**, *5* (1), 233-239.
76. Murai, S.; Fujita, K.; Daido, Y.; Yasuhara, R.; Kamakura, R.; Tanaka, K., Plasmonic arrays of titanium nitride nanoparticles fabricated from epitaxial thin films. *Optics express* **2016**, *24* (2), 1143-1153.
77. Guo, R.; Hakala, T. K.; Törmä, P., Geometry dependence of surface lattice resonances in plasmonic nanoparticle arrays. *Physical Review B* **2017**, *95* (15), 155423.
78. Lin, C.-H.; Chen, H.-L.; Chao, W.-C.; Hsieh, C.-I.; Chang, W.-H., Optical characterization of two-dimensional photonic crystals based on spectroscopic ellipsometry with rigorous coupled-wave analysis. *Microelectronic engineering* **2006**, *83* (4-9), 1798-1804.
79. Wagner, R.; Cichos, F., Fast measurement of photonic stop bands by back focal plane imaging. *Physical Review B* **2013**, *87* (16), 165438.
80. Robertson, W.; Arjavalingam, G.; Meade, R.; Brommer, K.; Rappe, A. M.; Joannopoulos, J., Measurement of photonic band structure in a two-dimensional periodic dielectric array. *Physical review letters* **1992**, *68* (13), 2023.
81. Labilloy, D.; Benisty, H.; Weisbuch, C.; Krauss, T.; De La Rue, R.; Bardinal, V.; Houdré, R.; Oesterle, U.; Cassagne, D.; Jouanin, C., Quantitative measurement of transmission, reflection, and diffraction of two-dimensional photonic band gap structures at near-infrared wavelengths. *Physical review letters* **1997**, *79* (21), 4147.
82. Humphrey, A. D.; Barnes, W. L., Plasmonic surface lattice resonances on arrays of different lattice symmetry. *Physical Review B - Condensed Matter and Materials Physics* **2014**, *90*.
83. Evlyukhin, A. B.; Reinhardt, C.; Zywietz, U.; Chichkov, B. N., Collective resonances in metal nanoparticle arrays with dipole-quadrupole interactions. *Physical Review B - Condensed Matter and Materials Physics* **2012**, *85*.
84. Wang, L.; Zhang, R. Y.; Xiao, M.; Han, D.; Chan, C. T.; Wen, W., The existence of topological edge states in honeycomb plasmonic lattices. *New Journal of Physics* **2016**, *18*.
85. Hakala, T. K.; Rekola, H. T.; Väkeväinen, A. I.; Martikainen, J. P.; Nečada, M.; Moilanen, A. J.; Törmä, P., Lasing in dark and bright modes of a finite-sized plasmonic lattice. *Nature Communications* **2017**, *8*, 1-7.
86. Lu, L.; Joannopoulos, J. D.; Soljačić, M., Topological photonics. *Nature Publishing Group* **2014**, *8*, 821-829.
87. Noh, J.; Benalcazar, W. A.; Huang, S.; Collins, M. J.; Chen, K. P.; Hughes, T. L.; Rechtsman, M. C., Topological protection of photonic mid-gap defect modes. *Nature Photonics* **2018**, *1*.

88. Downing, C. A.; Weick, G., Topological collective plasmons in bipartite chains of metallic nanoparticles. *Physical Review B* **2017**, *95*.
89. Pocock, S.; Xiao, X.; Huidobro, P. A.; Giannini, V., The topological plasmonic chain with retardation and radiative effects. *ACS Photonics* **2018**, *5*, 2271-2279.
90. Zou, S.; Janel, N.; Schatz, G. C., Silver nanoparticle array structures that produce remarkably narrow plasmon lineshapes. *Journal of Chemical Physics* **2004**, *120*, 10871-10875.
91. Wu, L.-H.; Hu, X., Scheme for achieving a topological photonic crystal by using dielectric material. *Physical review letters* **2015**, *114* (22), 223901.
92. Hohenester, U.; Trugler, A., MNPBEM - A Matlab toolbox for the simulation of plasmonic nanoparticles. *Comput Phys Commun* **2012**, *183* (2), 370-381.
93. Sherry, L. J.; Chang, S. H.; Schatz, G. C.; Van Duyne, R. P.; Wiley, B. J.; Xia, Y. N., Localized surface plasmon resonance spectroscopy of single silver nanocubes. *Nano Letters* **2005**, *5* (10), 2034-2038.
94. Cherqui, C.; Li, G. L.; Busche, J. A.; Quillin, S. C.; Camden, J. P.; Masiello, D. J., Multipolar Nanocube Plasmon Mode-Mixing in Finite Substrates. *J Phys Chem Lett* **2018**, *9* (3), 504-512.
95. Wang, W.; Watkins, N.; Yang, A.; Schaller, R. D.; Schatz, G. C.; Odom, T. W., Ultrafast Dynamics of Lattice Plasmon Lasers. *The Journal of Physical Chemistry Letters* **2019**, 3301-3306.
96. Vasa, P.; Wang, W.; Pomraenke, R.; Lammers, M.; Maiuri, M.; Manzoni, C.; Cerullo, G.; Lienau, C., Real-time observation of ultrafast Rabi oscillations between excitons and plasmons in metal nanostructures with J-aggregates. *Nature Photonics* **2013**, *7* (2), 128-132.
97. Shi, L.; Hakala, T. K.; Rekola, H. T.; Martikainen, J. P.; Moerland, R. J.; Torma, P., Spatial Coherence Properties of Organic Molecules Coupled to Plasmonic Surface Lattice Resonances in the Weak and Strong Coupling Regimes. *Physical Review Letters* **2014**, *112* (15).
98. Liu, W. J.; Lee, B.; Naylor, C. H.; Ee, H. S.; Park, J.; Johnson, A. T. C.; Agarwal, R., Strong Exciton-Plasmon Coupling in MoS<sub>2</sub> Coupled with Plasmonic Lattice. *Nano Letters* **2016**, *16* (2), 1262-1269.
99. Hakala, T. K.; Moilanen, A. J.; Vakevainen, A. I.; Guo, R.; Martikainen, J. P.; Daskalakis, K. S.; Rekola, H. T.; Julku, A.; Torma, P., Bose-Einstein condensation in a plasmonic lattice. *Nat Phys* **2018**, *14* (7), 739-+.
100. Yablonovitch, E., Photonic band-gap structures. *J. Opt. Soc. Am. B* **1993**, *10* (2), 283-295.
101. Busch, K.; John, S., Photonic band gap formation in certain self-organizing systems. *Physical Review E* **1998**, *58* (3), 3896-3908.
102. Mao, Q.; Xie, K.; Hu, L.; Li, Q.; Zhang, W.; Jiang, H.; Hu, Z.; Wang, E., Light trapping at Dirac point in 2D triangular Archimedean-like lattice photonic crystal. *Applied optics* **2016**, *55* (12), B139-B143.
103. Notomi, M.; Suzuki, H.; Tamamura, T.; Edagawa, K., Lasing action due to the two-dimensional quasiperiodicity of photonic quasicrystals with a Penrose lattice. *Physical review letters* **2004**, *92* (12), 123906.
104. Zhou, D.; Biswas, R., Photonic crystal enhanced light-trapping in thin film solar cells. *Journal of Applied Physics* **2008**, *103* (9), 093102.

105. Lang, M. J.; Fordyce, P. M.; Engh, A. M.; Neuman, K. C.; Block, S. M., Simultaneous, coincident optical trapping and single-molecule fluorescence. *Nature methods* **2004**, *1* (2), 133.
106. John, S., Why trap light? *Nature materials* **2012**, *11* (12), 997.
107. Maier, S. A., *Plasmonics: Fundamentals and Applications*. 2007.
108. Li, R.; Wang, D.; Guan, J.; Wang, W.; Ao, X.; Schatz, G. C.; Schaller, R.; Odom, T. W., Plasmon nanolasing with aluminum nanoparticle arrays. *JOSA B* **2019**, *36* (7), E104-E111.
109. Guo, R.; Nečada, M.; Hakala, T. K.; Väkeväinen, A. I.; Törmä, P., Lasing at K Points of a Honeycomb Plasmonic Lattice. *Physical review letters* **2019**, *122* (1), 013901.
110. Xiong, W.; Jiang, L. J.; Baldacchini, T.; Lu, Y. F., 9 - Laser additive manufacturing using nanofabrication by integrated two-photon polymerization and multiphoton ablation. In *Laser Additive Manufacturing*, Brandt, M., Ed. Woodhead Publishing: 2017; pp 237-256.
111. Balamurugan, R.; Liu, J.-H., A review of the fabrication of photonic band gap materials based on cholesteric liquid crystals. *Reactive and Functional Polymers* **2016**, *105*, 9-34.
112. Langguth, L.; Punj, D.; Wenger, J.; Koenderink, A. F., Plasmonic band structure controls single-molecule fluorescence. *ACS nano* **2013**, *7* (10), 8840-8848.
113. Bleckmann, F.; Cherpakova, Z.; Linden, S.; Alberti, A., Spectral imaging of topological edge states in plasmonic waveguide arrays. *Physical Review B* **2017**, *96* (4), 045417.
114. Cheng, Q.; Pan, Y.; Wang, Q.; Li, T.; Zhu, S., Topologically protected interface mode in plasmonic waveguide arrays. *Laser & Photonics Reviews* **2015**, *9* (4), 392-398.
115. Dubrovkin, A. M.; Adamo, G.; Yin, J.; Wang, L.; Soci, C.; Wang, Q. J.; Zheludev, N. I., Visible range plasmonic modes on topological insulator nanostructures. *Advanced Optical Materials* **2017**, *5* (3), 1600768.
116. Autore, M.; D'Apuzzo, F.; Di Gaspare, A.; Giliberti, V.; Limaj, O.; Roy, P.; Brahlek, M.; Koirala, N.; Oh, S.; Garcia de Abajo, F. J., Plasmon–phonon interactions in topological insulator microrings. *Advanced Optical Materials* **2015**, *3* (9), 1257-1263.
117. Wang, L.; Zhang, R.-Y.; Xiao, M.; Han, D.; Chan, C. T.; Wen, W., The existence of topological edge states in honeycomb plasmonic lattices. *New Journal of Physics* **2016**, *18* (10), 103029.
118. Zhang, Y.-L.; Wu, R. P.; Kumar, A.; Si, T.; Fung, K. H., Nonsymmorphic symmetry-protected topological modes in plasmonic nanoribbon lattices. *Physical Review B* **2018**, *97* (14), 144203.
119. Liu, W.; Hwang, M.; Ji, Z.; Wang, Y.; Modi, G.; Agarwal, R., Z2 Photonic Topological Insulators in the Visible Wavelength Range for Robust Nanoscale Photonics. *Nano Letters* **2020**.
120. Poddubny, A.; Miroshnichenko, A.; Slobozhanyuk, A.; Kivshar, Y., Topological Majorana States in Zigzag Chains of Plasmonic Nanoparticles. *ACS Photonics* **2014**, *1* (2), 101-105.
121. Weast, R. C.; Astle, M. J.; Beyer, W. H., *CRC handbook of chemistry and physics*. CRC press Boca Raton, FL: 1988; Vol. 69.

## Ran Li

• RanLi2014@u.northwestern.edu • +1 (224) 307-3533

### EDUCATION

<b>Northwestern University</b> , Evanston, IL Ph.D. candidate in Material Science and Engineering	2014 – 2020
<b>University of Science and Technology of China</b> , Hefei, China B.S. in Material Science and Engineering	2010 – 2014

### RESEARCH EXPERIENCE

**Northwestern University**, Evanston, IL

- Graduate research advised by Prof. Teri W. Odom
  - Designed and optimized the nano fabrication process (photolithography, reactive ion etching and wet etching, metal deposition processes) to engineer the diameter of metallic nanoparticles arranged in an array
  - Worked as an independent project leader collaborating with a theoretical chemistry group to investigate the optical properties of new plasmonic materials (aluminum) with strong hands-on experimental skills
  - Initiated and designed new optical setup with femtosecond laser pump using lasing emission signals as a tool to discover newly plasmonic modes in Bravais and non-Bravais lattices of plasmonic nanoparticle arrays
  - Achieved multi-color (from visible to near-infrared wavelength range) laser by engineering the shape of metal nanoparticles on a single honeycomb lattice
  - Designed time-resolved photoluminescence setup and optimized the experimental procedure of incorporating quantum dots onto plasmonic nanoparticle arrays to control the lasing emission process
  - Collaborated in an interdisciplinary center spanning 5 groups across 4 disciplines to publish advances in transparent electronic semiconductors with expertise in *in-situ* heating TEM and SEM
  - Served as an expert for designing optical simulation models with FDTD solutions and wrote Lumerical and Matlab scripts for data processing and analyses
  - Coordinated 4 grant reviews and 4 proposal writings of which three successful and one on-going

### AWARDS

Graduate Student Conference Travel Grant Award	2018
ASU Winter School on High Resolution Electron Microscopy Scholarship	2016
Guo Moruo Presidential Scholarship	2014
National Scholarship	2018

## PUBLICATIONS

1. **Li, R.**; Bourgeois, M.; Cherqui, C.; Guan, J.; Wang, W.; Hu, J.; Schatz, G. C.; Schaller, R.; Odom, T. W., Hierarchical Hybridization in Plasmonic Honeycomb Lattices. *Nano Letters* **2019**, 19, 9, 6345 - 6441.
2. **Li, R.**; Wang, D.; Guan, J.; Wang, W.; Ao, X.; Schatz, G. C.; Schaller, R.; Odom, T. W., Plasmon Nanolasing with Aluminum Nanoparticle Arrays. *JOSA B* **2019**, 36, E104-E111.
3. **Li, R.**; Moghadam, M. M.; Buchholz, D. B.; Li, Q.; Voorhees, P. W.; Dravid, V. P., In situ Crystallization and Morphological Evolution in Multicomponent Indium Oxide Thin Films. *Crystal Growth & Design* **2017**, 17, 1396-1403.
4. Knudson, M. P.; **Li, R.**; Wang, D.; Wang, W.; Schaller, R. D.; Odom, T. W., Polarization-Dependent Lasing Behavior from Low-Symmetry Nanocavity Arrays. *ACS nano* **2019**, 13, 7435-7441.
5. Guan, J.; Sagar, L. K.; **Li, R.**; Wang, D.; Bappi, G.; Watkins, N. E.; Bourgeois, M. R.; Levina, L.; Fan, F.; Hoogland, S.; Voznyy, O.; Martins de Pina, J.; Schaller, R. D.; Schatz, G. C.; Sargent, E. H.; Odom, T. W., Engineering Directionality in Quantum Dot Shell Lasing Using Plasmonic Lattices. *Nano Letters* **2020**, 20 (2), 1468-1474.
6. Guan, J.; Sagar, L. K.; **Li, R.**; Wang, D.; Bappi, G.; Wang, W.; Watkins, N.; Bourgeois, M. R.; Levina, L.; Fan, F.; Hoogland, S.; Voznyy, O.; de Pina, J. M.; Schaller, R. D.; Schatz, G. C.; Sargent, E. H.; Odom, T. W., Quantum Dot-Plasmon Lasing with Controlled Polarization Patterns. *ACS Nano* **2020**.
7. Wang, G.; Huang, W.; Eastham, N. D.; Fabiano, S.; Manley, E. F.; Zeng, L.; Wang, B.; Zhang, X.; Chen, Z.; **Li, R.**, Aggregation Control in Natural Brush-printed Conjugated Polymer Films and Implications for Enhancing Charge Transport. *Proceedings of the National Academy of Sciences* **2017**, 114, E10066-E10073.
8. Huang, W.; Guo, P.; Zeng, L.; **Li, R.**; Wang, B.; Wang, G.; Zhang, X.; Chang, R. P.; Yu, J.; Bedzyk, M. J., Metal Composition and Polyethylenimine Doping Capacity Effects on Semiconducting Metal Oxide–Polymer Blend Charge Transport. *Journal of the American Chemical Society* **2018**, 140, 5457-5473.
9. Zeng, L.; Moghadam, M. M.; Buchholz, D. B.; **Li, R.**; Keane, D. T.; Dravid, V. P.; Chang, R. P.; Voorhees, P. W.; Marks, T. J.; Bedzyk, M. J., Processing-dependent Thermal Stability of a Prototypical Amorphous Metal Oxide. *Physical Review Materials* **2018**, 2, 053401.

10. Islam, S. M.; Peng, L.; Zeng, L.; Malliakas, C. D.; Chung, D. Y.; Buchholz, D. B.; Chasapis, T.; **Li, R.**; Chrissafis, K.; Medvedeva, J. E., Multistates and Polyamorphism in Phase-Change K<sub>2</sub>Sb<sub>8</sub>Se<sub>13</sub>. *Journal of the American Chemical Society* **2018**, *140*, 9261-9268.
11. Wang, D.; Bourgeois, M. R.; Lee, W.-K.; **Li, R.**; Trivedi, D.; Knudson, M. P.; Wang, W.; Schatz, G. C.; Odom, T. W., Stretchable Nanolasing from Hybrid Quadrupole Plasmons. *Nano letters* **2018**, *18*, 4549-4555.

## CONFERENCES AND PRESENTATIONS

- MRS Fall Meeting** Boston, MA 2019  
Talk: "Dipole-quadrupole Coupling from Plasmonic Honeycomb Lattices"
- Gordon Conference** Waterville Valley, NH 2018  
Poster: "Polarization-Dependent Lasing Behavior from Low-Symmetry Nanocavity Arrays"

## PROFICIENCIES AND SKILLS

### Nanofabrication

Phase-shift photolithography, Reactive ion etching, Deep reactive ion etching, E-beam Evaporation, Thermal Evaporation, *In-situ* TEM, SEM, XRD, ALD, PECVD, AFM

### Optical characterization

Optical Set-up, Lasing Detection, Time-resolved Photoluminescence, Angle-resolved Spectroscopy, UV-VIS Spectrophotometry

### Modeling and Computation

Finite-Difference Time-Domain (FDTD) Modeling, MATLAB, Adobe Illustrator, Blender 3D Software

## LEADERSHIP POSITIONS

- 2017-19 Laser Instrument Manager, the Odom Group
- 2017-20 Rotational-stage Spectrometer Manager, the Odom Group
- 2017-20 Clean Room Manager, the Odom Group

## REFERENCE CONTACTS

### Prof. Teri W. Odom

Department of Chemistry, Department of Materials Science and Engineering, Northwestern University

Email: [todom@northwestern.edu](mailto:todom@northwestern.edu)

Phone: 01-847-491-7674